Tuning energy dissipation/damping by topography of poro-viscoelastic interfaces

By

Lejie Liu

A dissertation submitted in partial fulfillment of

the requirements for the degree of

Doctor of Philosophy

(Mechanical Engineering)

at the

UNIVERSITY OF WISCONSIN - MADISON

2022

Date of final oral examination: September 30, 2021

The dissertation will be approved by the following members of the Final Oral Committee:

Melih Eriten, Associate Professor, Mechanical Engineering
Corinne R. Henak, Assistant Professor, Mechanical Engineering
Dan Negrut, Professor, Mechanical Engineering
Matt Allen, Professor, Engineering Physics
Michael R. Zinn, Associate Professor, Mechanical Engineering

ACKNOWLEDGEMENTS

I express my deep sense of gratitude to my advisor, Professor Melih Eriten. I appreciate your help and guidance on my research works. Thanks to your intelligent supervision, I learnt how to write professional reports and deal with complicated experiments. Thanks for all the great opportunities you offered to attend seminars, conferences, and summer school. I learnt a lot and really enjoyed these experiences.

Thanks to Professor Corinne Henak for all the intelligent feedbacks and suggestions you gave me. It is a great opportunity to work with you.

Thanks to my committee members Professor Matt Allen, Professor Dan Negrut, and Professor Mike Zinn. I appreciate your advice and support throughout my dissertation process. I am also grateful to the Departments of Mechanical Engineering for offering me research and teaching assistantships. Most of my doctoral work was supported by the National Science Foundation under Grants CMMI 1662456 and CAREER 1554146.

My gratitude to all the members in our lab, Ahmet Usta, Shixuan Chen, Guebum Han, Uraching Chowdhury, Utku Boz, Karthik Yerrapragada, Ilke Ozsut, Cole Hess, and Haocheng Yang. The discussions we had made me a better researcher.

Finally, I wish to express my sincere gratitude to my parents for their unconditional support throughout my life. A special thanks to my girlfriend, Quan for all her love and support.

ABSTRACT

Absorbing and trapping energy as achieved often by dampers in a prescribed frequency range is essential for vibration suppression in engineered systems. Dampers with various damping mechanisms are the most common devices to dissipate undesired vibratory energy. This dissertation provides a novel indenter-foam passive damper idea with poro-viscoelastic (PVE) damping mechanism. The first objective was to introduce a passive damper design inspired by the PVE material damping mechanisms. In particular, a passive PVE damper, where a PVE layer is sandwiched between two hard materials with multiple interfacial length scales, was simulated using multiple fractional Zener models in parallel. Simulation results showed that one can ideally design such a passive damper that dissipate maximum energy at a desired bandwidth of loading frequencies, either for broadband or for narrowband. The second objective was to validate and realize the passive damper idea developed in objective one. Multiple single-indenter–foam dampers were designed by combining foam sheets with different pore diameters and indenters with different radii. Their damping capacity was investigated by dynamic mechanical analysis in a frequency range of 0.5–100 Hz. Single-indenter–foam dampers delivered peak damping frequencies that depended on the foam's pore diameter and characteristic diffusion length (contact radii). Those dampers maximized the damping capacity at the desired frequency (narrowband performance). Afterwards, combinations of single-indenter–foam dampers were optimized to obtain a two-indenter–foam damper that delivered nearly rate-independent damping capacity within 0.5–100 Hz (broadband performance). These findings suggested that such indenter-foam damper can be an effective mean of passive damping for both narrowband and broadband applications. The third objective was to extend the behavior of the indenter-foam damper to a higher excitation level, for both strain and stain rate. The nonlinearity maps that described the

degree of nonlinear behavior of the indenter-foam dampers were generated as a function of strains and strain rates. The major reasons caused such nonlinearity were found to be the reduction in contact stiffness, and the decrease in contact lengths. Nonlinear dynamic response could complicate the design and limit usability of indenter-foam dampers. Those findings suggested increasing adhesion at the indenter-foam interface would suppress those nonlinearities trivially. In summary, all the outcomes and findings of three objectives together provided a thorough understanding on PVE damping mechanism and a mature guideline on PVE indenter-foam dampers.

TABLE OF CONTENTS

Page

LIST OF FIGURES

Page

Chapter 1 Introduction

1.1. Damping Mechanisms

Absorption and dissipation of vibratory energy in a prescribed frequency range is essential for most man-made structures. Unlike other system parameters like mass or stiffness, damping cannot be simply derived as a function of the system geometry and material properties. There could be multiple physical mechanisms that together result in the observed damping, but one major factor can be considered as the dominant damping mechanism [1]. There are as many damping mechanisms as there are different ways of converting mechanical energy into thermal energy. The most important mechanisms are interface friction, fluid viscosity, and mechanical hysteresis (material damping) [2]. Interface topography plays a significant role in the interfacial frictional and material damping, and it includes surface roughness, curvature, lay, waviness and slopes. For example, in order to properly predict the frictional behavior of jointed contact and get a realistic value of joint damping, the mathematical description of its surface roughness must be accounted for [3].

Lazan describes frictional damping as the structural damping caused mainly by slip and micro-impacts occurring at the contact interfaces [4]. For metallic assemblies, frictional damping is orders of magnitude higher than the material damping, and hence, controls the amplitude of dynamic response of structures to a great extent. Hartog [5], Cattaneo [6], and Mindlin [7] provided the classical solutions to the frictional interactions under sliding and partial-slip (micro-slip) contacts loaded by a constant normal and monotonically increasing tangential forces. Those solutions listed the static friction and applied tangential forces as the parameters tuning the frictional slip and thus dissipation. In addition, frictional slip and force were found to depend on

slip rates and system states [8–10]. In the last four decades, additional parameters such as normal load fluctuations and phase difference between dynamic loads imposed on contact were shown to affect frictional dissipation significantly. High normal pressures lead to suppression of sliding, whereas low pressures promote frictional slip while decreasing the shear tractions over the interface. Therefore, tuning frictional dissipation is possible by continuous preload-control [11–14]. Imposing a dynamic preload and adjusting the phase difference between the preload and tangential vibrations provides an alternative approach to tuning frictional dissipation [15–18]. The effect of surface geometry on frictional dissipation was first embedded in the response of spherical contacts to cyclic loading by Mindlin et al. [19]. The dissipation was found to scale inversely with a contact radius under constant normal load and tangential fluctuation amplitude. More recently, frictional dissipation was investigated extensively in arbitrary 2D contacts [20,21], and rough surfaces [18,22,23]. In those works, surface geometry and compliance were found as major factors affecting dissipation. Our group studied the influence of both surface roughness [24] and curvature [25,26] on frictional damping. The surface roughness plays a significant role on the wear evolution of frictional cyclic contacts. It was highly plastic contact at the initial cycles and transformed to elastic dominant contact afterwards. Therefore, the natural frequency and damping of the contact interface changed due to the change in surface roughness [24]. We studied the influence of patterned geometry on frictional damping as well: the tension-induced wrinkling phenomenon of a composite surface was utilized to generate the sinusoidal patterned surface [27]. A large mismatch in stiffness of constituents was also a key factor in creating wrinkles on composite surface layers such as soft biological tissues and soft-hard materials interfaces [28–30]. We investigated a similar configuration as in [31], and tuned frictional dissipation on wrinkled (patterned) surfaces.

Viscous damping is mainly due to the viscous force that prevents the opposite shear motion against the fluid. The most famous example of the viscous damping is the dashpot element that is widely used as a mathematical tool in vibration studies. Viscous damping was first applied in the military and aerospace industries and then was adapted for structural applications in civil engineering [32]. Constantinou and Symans introduced a viscous fluid device that consists of a piston within a housing space filled with silicone oils [33]. Such a device could dissipate energy and be used to prevent structures from earthquake-induced vibrations by taking advantage of the viscous damping. Many studies by different researchers optimize the viscous damping devices by sophisticated techniques [34–36] or design optimization of active and passive structural controller [37]. Viscous damping is heavily applied to reduce vibrations of bridge [38]. Fluid viscous dampers were built to reduce both the first few modes [39] and higher modes [40] of the bridge vibrations depending on the purpose of usage. Viscous damping can also play a significant role to dissipate undesired vibratory energy at many length scales, from Micro-electromechanical Systems (MEMS) [41] to aerospace structures [42].

Material damping is known as the most complex damping mechanism not only because of various micro-scale behaviors such as grain defects, local thermal effects, and dislocations in the grain lamina, but also due to the diversity of materials, i.e., frequency dependent damping mechanism for biological tissues and frequency independent damping mechanism for most metals [1]. Therefore, most researchers modeled material damping not distinguished by different materials, but based on rate dependence [43]. Rate-independent damping is also known as the ideal hysteretic damping [44], which is widely used in structural vibration analysis [45] and soil behavior studies [46]. Rate-dependent damping is dominantly observed in soft materials with time-dependent mechanical properties; i.e., viscoelastic and poro-viscoelastic (PVE) relaxations [47].

Viscoelastic materials have been employed in sandwiched [48] and other composite structures [49] to enhance viscoelastic damping. Viscoelastic damping has been widely used in aerospace, automotive [50], turbines [51], and MEMS [52]. Viscoelastic damping is length scale independent, while PVE damping is dependent on diffusion length scale [53,54]. Poroelastic materials are well-known for their time-dependent behaviors [55]. Poroelastic damping has already been utilized for synthetic noise absorption, but damping efficacy in those cases is limited to high frequency excitations. Recent efforts attempt at expanding the bandwidth, especially to lower frequencies by active and passive composite systems [56,57]. Deshmukh and McKinley provided PVE composites (open-cell polyurethane foam with magnetorheological fluid) as an adaptive energy absorbing material [58]. They concluded that such fluid-based composites can be used for wide-ranging energy absorbing applications from ballistic armor to automotive components.

1.2. Categories of Damper

In recent years, many innovative dampers that absorbs vibratory energy have been studied in various research groups. They can be divided into three major categories: passive energy dissipation, active energy dissipation, and semiactive energy dissipation [32,59]. These categories of dampers usually utilize one or more damping mechanisms to absorb vibratory energy.

A passive damper, as implied by its name, does not require an external power supply [60]. A passive damper usually uses a single damping mechanism to reduce vibratory energy, and it is widely used in all man-made structures from macro-scale (spacecraft and buildings) to micro-scale (MEMS) systems. Metallic yield damper, as a common passive energy dissipation method for earthquake-resistance, takes advantage of the inelastic deformation of metals. X-shape and honeycomb structures with steel, lead, or shape-memory alloys are used as the metallic yield

devices [61,62]. Those dampers possess stable hysteretic behavior, long term reliability, and relative insensitivity to environmental temperature [32]. Friction dampers are widely used to avoid high cycle fatigue failures of gas-turbine blades [63]. There are two basic types of friction dampers: blade to ground damper links a vibrating point on the blade to a relatively rigid structure such as a cover plate; blade to blade damper links two points on the blade. Both type of dampers dissipate energy when frictional slip occurs on the linked contact points [14,64]. For MEMS devices with a fluid film squeezed between two plates, the so-called squeeze film damping becomes an important mechanism that need to be investigated thoroughly. Squeeze film effect changes the desired dynamic behavior of MEMS devices, such as accelerometers, optical switches, micro-torsion mirrors, and resonators significantly [65]. Nevertheless, additional damping is shown to provide stability to some MEMS devices such as micro accelerometers [66]. Thus, squeeze film damping needs to be evaluated whether to be reduced or enhanced depending on the design criteria and operating conditions of the MEMS [67].

Active dampers are usually force delivery devices integrated with real-time processing controllers. Active dampers are used when high performance is needed or the system behavior is varied due to surrounding environment. Hence, active dampers consist of a set of sensors (strain, acceleration, velocity, force), a set of actuators (force, inertial, strain), and a control algorithm (feedback or feedforward) [68]. One of the earliest active dampers was made in 1989 with active damping of truss structures for a high accuracy structures requirement. Each strut consisted of a piezoelectric linear actuator colinear with a force transducer. The desired damping profile was obtained due to velocity feedback and the application of collocated force [69]. It was improved with embedding viscous damping actuator to gain higher damping performance within an optional frequency range [70]. The first full-scale application of active damper system, Active Mass Driver

(AMD) system, to a building was accomplished by the Kajima Corporation in 1989. It consists of an auxiliary mass installed in a building and an actuator that operates the mass and produces a control force which reduces building vibrations under strong wind or earthquake [71]. Active dampers are widely used in the suspension system of automobiles. Bose Corporation provided an active suspension system that consists of an electromagnetic motor and a power amplifier [72]. The major characteristics of such active dampers are high controllability and energy regeneration [73]. Kawamoto et al. presented a similar electromagnetic damper for automobile suspension, and did both shaker tests and simulations to validate the energy dissipation capacity of the dampers [74].

Recently, semi-active dampers became popular in various vibration control applications: they consist of passive energy dissipation component with controllable properties. Semi-active dampers usually require less power than active dampers, and the energy can be stored locally in a portable battery without external power supply [68]. The magneto-rheological (MR) fluid damper is a famous example of semi-active dampers. MR fluid was first discovered by Jacob Rabinow in 1951 [75]. The magnetizable particles inside MR fluid form a chain-like structure to restrict the flow of the fluid when magnetic field is applied. When no field is applied, the rheological fluids exhibit a Newtonian behavior. MR fluid dampers are commonly used to reduce vibration in automotive industry. Lam and Liao proposed a semi-active MR fluid damper for vehicle suspension system, and the damper controller was designed to adjust the appropriate input voltage to the MR damper [76]. They tested the damper under sinusoidal excitations and the results showed the damper can improve the ride comfort quite effectively. MR fluid dampers were also built for seismic protection of buildings. Johnson et al. compared two possible types of dampers: ideal fully active damper and semi-active MR damper [77]. They did earthquake excitation tests and the MR

damper showed significant vibratory reduction while much less power was required. Piezoelectric transducer with switched electrical networks is another example for semi-active dampers. The vibratory energy is collected in the capacitor of a piezoelectric transducer and transformed into electric charge. Onoda et al. provided numerical simulation and experiments of a truss structure embedded with such piezoelectric transducers under vibrations, and the results showed an effective vibration reduction [78]. Alternatively, some researchers proposed a hybrid damper as a combination of passive and active devices. It can be treated as the same as semi-active dampers, but sometimes hybrid damper can have both passive and active energy dissipation components [32].

Each type of dampers has advantages and disadvantages. For example, passive dampers are cheaper and easier to design and manufacture, but they are less efficient under unknown operating conditions when real-time control of damping profile is necessary. Active dampers are desired when high damping performance is needed or the system vibratory behavior is varied due to surrounding environment. However, active vibration control is not always better than passtive and has several limitations such as complex design requirements, need for power and sophisticated auxiliary components such as electronics and software, and costs associated with those. Semi-active dampers require less power than active vibration control systems and are more portable without external power supply. The limitation of semi-active dampers includes but not limited to, inappropriate for vibrations of small amplitude and relatively higher costs than passive dampers [79]. In most engineering applications, an active solution should normally be considered only after all other passive means have been exhausted [68].

1.3. The Major Contribution of the Dissertation

The traditional vibration dissipation methods discussed above required costly and heavy sets of auxiliary materials and components, yet still lack effectiveness on a broadband frequency range. For instance, Wang and Inman presented an active damper design combining piezo-ceramics, oxides, polymers and elastomers in a functionally graded multilayer composite, which provided effective damping within structural vibration regime (10-200 Hz) [80]. Numerous research groups have demonstrated broad frequency band gaps by using fractal, granular, particle and beam-based composite metamaterials [81,82]. However, those frequency band gaps reside at higher frequency ranges than structural vibrations (>200 Hz). Harne et al. introduced so-called hyperdamping metamaterials achieving broadband energy dissipation (up to 1600 Hz), but it lacked any discussion on rate-dependence [83]. Therefore, this dissertation introduces a PVE damper design that fills the gaps in the current literature: it yields rate-independent relaxation damping within a wide range of frequencies.

The major topic of this dissertation is to examine the influence of interface topography on PVE material damping, and to design and fabricate a prototype of a passive damper that uses PVE material damping. In this work, both narrowband [84] and broadband [85] passive dampers were simulated, fabricated, and validated through dynamic mechanical analysis (DMA). The broadband damper consists of a PVE layer, which is sandwiched between two hard materials with multiple length scales, and the damper can obtain a relatively constant loss factor for an unprecedented frequency range (3-3000 Hz). We designed and validated a practical composite PVE damper [86]. Rigid cylindrical indenters and open-cell polyethylene foam with Newtonian liquid was used as the PVE dampers. We conducted DMA to obtain rate-independent damping capacity over a frequency range of 0.5-100 Hz. These findings demonstrated the potential of attenuating vibrations

at a specific modal frequency by tuning the peak damping frequency of an indenter-foam PVE damper. Although many systems, such as automobile, aerospace, and measurement devices, require broadband damping, narrow-band dampers are also widely used in sensitive detection [87], sensing [88], acoustic fields [89] and machining applications [90,91]. The damping profile of our PVE damper can be tuned for optimal narrow-banded or broad-banded damping performance. Small vibration assumption assisted us in modeling the indenter-foam system with linearized PVE models in those damper designs. In the last part of my study, I studied nonlinearities observed in dynamic response of indenter-foam dampers. I found that adhesion and peeling process at the indenter-foam interfaces were the major source of nonlinear dynamic response.

To summarize, this dissertation discusses how the interface topography and length scales affect PVE material damping. In Chapter 2, I introduce a broadband damper design inspired by the cartilage-like relaxation mechanisms. Chapter 2 was published in Journal of Sound and Vibration [85]. I contributed writing, modeling, and optimizing of design in this work. In Chapter 3, I introduce the designing, fabricating, and validating of an indenter-foam PVE damper. Chapter 3 was published in Journal of Vibration and Acoustics [86]. I contributed part of the writing, fabricating the damper, and conducting DMA tests. In Chapter 4, I introduce a DMA characterization of the indenter-foam damper under higher excitation levels and discuss the nonlinear behavior of the damper. Chapter 4 is prepared to be submitted to a Journal. I contributed the writing, fabricating the damper, and conducting DMA and adhesion tests. Finally, Chapter 5 presents conclusions and future work.

1.4. References

[1] A. Puthanpurayil, R. Dhakal, A. Carr, Modelling of In-Structure Damping: A Review of the State-of-the-art, In Proc. Ninth Pacific Conf. Earthquake Engineering, (2011) No. 091

[2] E.E. Ungar, The status of engineering knowledge concerning the damping of built-up structures, J. Sound Vib. 26 (1973) 141–154.

[3] A.S.R. Murty, K.K. Padmanabhan, Effect of surface topography on damping in machine joints, Precis. Eng. 4 (1982) 185–190.

[4] B.J. Lazan, Damping of materials and members in structural mechanics, Pergamon press Oxford, 1968.

[5] J.P.D. Hartog, LXXIII. Forced vibrations with combined viscous and coulomb damping, Lond. Edinb. Dublin Philos. Mag. J. Sci. 9 (1930) 801–817.

[6] C. Cattaneo, Sul contatto di due corpi elastici: distribuzione locale degli sforzi, Rend Accad Naz Lincei. 27 (1938) 342–348.

[7] R.D. Mindlin, Compliance of elastic bodies in contact, J Appl Mech. 16 (1949) 259–268.

[8] J.H. Dieterich, Time-dependent friction and the mechanics of stick-slip, in: Rock Frict. Earthq. Predict., Springer, 1978: pp. 790–806.

[9] J.H. Dieterich, Modeling of rock friction: 1. Experimental results and constitutive equations, J. Geophys. Res. Solid Earth. 84 (1979) 2161–2168.

[10] A. Ruina, Slip instability and state variable friction laws, J. Geophys. Res. Solid Earth. 88 (1983) 10359–10370.

[11] E.J. Williams, S.W.E. Earles, Optimization of the response of frictionally damped beam type structures with reference to gas turbine compressor blading, J. Eng. Ind. 96 (1974) 471–476.

[12] C.F. Beards, A. Woowat, The control of frame vibration by friction damping in joints, J. Vib. Acoust. Stress Reliab. Des. 107 (1985) 26–32.

[13] L. Gaul, R. Nitsche, Friction control for vibration suppression, Mech. Syst. Signal Process. 14 (2000) 139–150.

[14] C.F. Beards, The damping of structural vibration by controlled interfacial slip in joints, J. Vib. Acoust. Stress Reliab. Des. 105 (1983) 369–373.

[15] J.H. Griffin, C.-H. Menq, Friction damping of circular motion and its implications to vibration control, J. Vib. Acoust. 113 (1991) 225–229.

[16] C.-H. Menq, P. Chidamparam, J.H. Griffin, Friction damping of two-dimensional motion and its application in vibration control, J. Sound Vib. 144 (1991) 427–447.

[17] Y.H. Jang, J.R. Barber, Effect of phase on the frictional dissipation in systems subjected to harmonically varying loads, Eur. J. Mech.-ASolids. 30 (2011) 269–274.

[18] C. Putignano, M. Ciavarella, J.R. Barber, Frictional energy dissipation in contact of nominally flat rough surfaces under harmonically varying loads, J. Mech. Phys. Solids. 59 (2011) 2442–2454.

[19] R.D. Mindlin, W.P. Mason, T.F. Osmer, H. Deresiewicz, Effects of an oscillating tangential force on the contact surfaces of elastic spheres, in: J. Appl. Mech.-Trans. ASME, ASME-AMER Soc Mechanical Eng 345 E 47TH ST, NEW YORK, NY 10017, 1951: pp. 331–331.

[20] M. Davies, J.R. Barber, D.A. Hills, Energy dissipation in a frictional incomplete contact with varying normal load, Int. J. Mech. Sci. 55 (2012) 13–21.

[21] J.R. Barber, M. Davies, D.A. Hills, Frictional elastic contact with periodic loading, Int. J. Solids Struct. 48 (2011) 2041–2047.

[22] D.B. Patil, M. Eriten, Effect of Roughness on Frictional Energy Dissipation in Presliding Contacts, J. Tribol. 138 (2016) 011401.

[23] D. Dini, D.A. Hills, Frictional Energy Dissipation in a Rough Hertzian Contact, J. Tribol. 131 (2009) 021401-021401–8.

[24] Fantetti, A., L. R. Tamatam, Martin Volvert, I. Lawal, L. Liu, L. Salles, M. R. W. Brake, C. W. Schwingshackl, and D. Nowell, The impact of fretting wear on structural dynamics: Experiment and Simulation, Tribology International 138 (2019): 111-124

[25] L. Liu, M. Eriten, Frictional Energy Dissipation in Wavy Surfaces, J. Appl. Mech. 83 (2016).

[26] Eriten, Melih, Ahmet D. Usta, and Lejie Liu. Tuning the Dissipation in Friction Dampers Excited by Depolarized Waves Across Patterned Surfaces, J. Vibration and Acoustics. 138, no. 5 (2016).

[27] E. Cerda, L. Mahadevan, Geometry and physics of wrinkling, Phys. Rev. Lett. 90 (2003) 074302.

[28] P.S. Stewart, S.L. Waters, T. El Sayed, D. Vella, A. Goriely, Wrinkling, creasing, and folding in fiber-reinforced soft tissues, Extreme Mech. Lett. 8 (2016) 22–29.

[29] Q. Li, T.J. Healey, Stability boundaries for wrinkling in highly stretched elastic sheets, J. Mech. Phys. Solids. 97 (2016) 260–274.

[30] G. Geng, L.A. Johnston, E. Yan, J.M. Britto, D.W. Smith, D.W. Walker, G.F. Egan, Biomechanisms for modelling cerebral cortical folding, Med. Image Anal. 13 (2009) 920–930.

[31] Q. Chen, A. Elbanna, Tension-induced tunable corrugation in two-phase soft composites: Mechanisms and implications, Extreme Mech. Lett. 4 (2015) 26–37.

[32] T.T. Soong, B.F. Spencer, Supplemental energy dissipation: state-of-the-art and state-of-the-practice, Eng. Struct. 24 (2002) 243–259.

[33] M.C. Constantinou, M.D. Symans, Experimental study of seismic response of buildings with supplemental fluid dampers, Struct. Des. Tall Build. 2 (1993) 93–132.

[34] T. TROMBETTI, S. SILVESTRI, Added Viscous Dampers in Shear-Type Structures: The Effectiveness of Mass Proportional Damping, J. Earthq. Eng. 8 (2004) 275–313.

[35] N. Wongprasert, M.D. Symans, Application of a genetic algorithm for optimal damper distribution within the nonlinear seismic benchmark building, J. Eng. Mech. 130 (2004) 401–406.

[36] W. Liu, M. Tong, G.C. Lee, Optimization methodology for damper configuration based on building performance indices, J. Struct. Eng. 131 (2005) 1746–1756.

[37] L. D Nikos, Design Optimization of Active and Passive Structural Control Systems, IGI Global, 2012.

[38] J.A. Main, N.P. Jones, Free Vibrations of Taut Cable with Attached Damper. I: Linear Viscous Damper, J. Eng. Mech. 128 (2002) 1062–1071.

[39] B.M. Pacheco, Y. Fujino, A. Sulekh, Estimation Curve for Modal Damping in Stay Cables with Viscous Damper, J. Struct. Eng. 119 (1993) 1961–1979.

[40] J.A. Main, N.P. Jones, A Comparison of Full-Scale Measurements of Stay Cable Vibration, Advanced Technology in Structural Engineering (2000) 1–8.

[41] T.B. Gabrielson, Mechanical-thermal noise in micromachined acoustic and vibration sensors, IEEE Trans. Electron Devices. 40 (1993) 903–909.

[42] D.H. Hibner, Dynamic response of viscous-damped multi-shaft jet engines, J. Aircr. (2012).

[43] A. Reggio, M. De Angelis, Modelling and identification of structures with rate-independent linear damping, Meccanica. 50 (2015) 617–632.

[44] S.H. Crandall, The Hysteretic Damping Model in Vibration Theory, Proc. Inst. Mech. Eng. Part C Mech. Eng. Sci. 205 (1991) 23–28.

[45] J.A. Inaudi, J.M. Kelly, Linear Hysteretic Damping and the Hilbert Transform, J. Eng. Mech. 121 (1995) 626–632.

[46] N. Makris, J. Zhang, Time-domain viscoelastic analysis of earth structures, Earthq. Eng. Struct. Dyn. 29 (2000) 745–768.

[47] R. Lakes, R.S. Lakes, Viscoelastic materials, Cambridge university press, 2009.

[48] Z. Li, M.J. Crocker, A review on vibration damping in sandwich composite structures, Int. J. Acoust. Vib. 10 (2005) 159–169.

[49] X.Q. Zhou, D.Y. Yu, X.Y. Shao, S.Q. Zhang, S. Wang, Research and applications of viscoelastic vibration damping materials: a review, Compos. Struct. 136 (2016) 460–480.

[50] M.D. Rao, Recent applications of viscoelastic damping for noise control in automobiles and commercial airplanes, J. Sound Vib. 262 (2003) 457–474.

[51] B.C. Nakra, Vibration control in machine and structures using viscoelastic damping, J. Sound Vib. 211 (1998) 449–466.

[52] B.M. Schöberle, Evaluation of viscoelastic materials for MEMS by creep compliance analysis, ETH Zurich, 2008.

[53] Unified solution for poroelastic oscillation indentation on gels for spherical, conical and cylindrical indenters, Soft matter 13.4 (2017): 852-861.

[54] G. Han, C. Hess, M. Eriten, C.R. Henak, Uncoupled poroelastic and intrinsic viscoelastic dissipation in cartilage, J. Mech. Behav. Biomed. Mater. 84 (2018) 28–34.

[55] M.A. Biot, General theory of three-dimensional consolidation, J. Appl. Phys. 12 (1941) 155–164.

[56] A.C. Slagle, C.R. Fuller, Low frequency noise reduction using poro-elastic acoustic metamaterials, in: 21st AIAACEAS Aeroacoustics Conf., 2015: p. 3113.

[57] J.P. Carneal, M. Giovanardi, C.R. Fuller, D. Palumbo, Re-Active Passive devices for control of noise transmission through a panel, J. Sound Vib. 309 (2008) 495–506.

[58] S.S. Deshmukh, G.H. McKinley, Adaptive energy-absorbing materials using field-responsive fluid-impregnated cellular solids, Smart Mater. Struct. 16 (2006) 106.

[59] B.F. Spencer, S. Nagarajaiah, State of the Art of Structural Control, J. Struct. Eng. 129 (2003) 845–856.

[60] Y.M. Parulekar, G.R. Reddy, Passive response control systems for seismic response reduction: A state-of-the-art review, Int. J. Struct. Stab. Dyn. 09 (2009).

[61] I.D. Aiken, D.K. Nims, J.M. Kelly, Comparative study of four passive energy dissipation systems, Bull. N. Z. Soc. Earthq. Eng. 25 (1992) 175–192.

[62] R.I. Skinner, R.G. Tyler, A.J. Heine, W.H. Robinson, Hysteretic dampers for the protection of structures from earthquakes, Bull. N. Z. Soc. Earthq. Eng. 13 (1980) 22–36.

[63] Jerry H. Griffin, A Review of Friction Damping of Turbine Blade Vibration, Int. J. Turbo Jet Engines. 7 (1990) 297–308.

[64] N.F. Rieger, Damping properties of turbine blades, SVIC Shock Vib. Dig. 11 (1979).

[65] M. Bao, H. Yang, Squeeze film air damping in MEMS, Sens. Actuators Phys. 136 (2007) 3–27.

[66] R. Houlihan, M. Kraft, Modelling squeeze film effects in a MEMS accelerometer with a levitated proof mass, J. Micromechanics Microengineering. 15 (2005) 893–902.

[67] S. Huang, D.-A. Borca-Tasciuc, J. Tichy, Limits of linearity in squeeze film behavior of a single degree of freedom microsystem, Microfluid. Nanofluidics. 16 (2014) 1155–1163.

[68] A. Preumont, Vibration Control of Active Structures: An Introduction, Springer, 2018.

[69] Experimental studies of adaptive structures for precision performance | 30th Structures, Structural Dynamics and Materials Conference, p. 1327.

[70] T.T. Hyde, E.H. Anderson, Actuator with Built-In Viscous Damping for Isolation and Structural Control, AIAA J. 34 (1996) 129–135.

[71] T. Kobori, N. Koshika, K. Yamada, Y. Ikeda, Seismic-response-controlled structure with active mass driver system. Part 1: Design, Earthq. Eng. Struct. Dyn. 20 (1991) 133–149.

[72] Rakshith, M., Yathin Kumar, and S. G. Vikas. Bose Automotive Suspension, International Journal of Recent Technology and Engineering (IJRTE) 3, no. 4 (2014)

[73] K. Nakano, Y. Suda, S. Nakadai, Self-powered active vibration control using a single electric actuator, J. Sound Vib. 260 (2003) 213–235.

[74] Y. Kawamoto, Y. Suda, H. Inoue, T. Kondo, Modeling of Electromagnetic Damper for Automobile Suspension, J. Syst. Des. Dyn. 1 (2007) 524–535.

[75] R. Jacob, Magnetic fluid torque and force transmitting device, U.S. Patent 2,575,360, issued November 20, 1951.

[76] H.F. Lam, W.-H. Liao, Semi-active control of automotive suspension systems with magnetorheological dampers, in: Smart Struct. Mater. 2001 Smart Struct. Integr. Syst., SPIE, 2001: pp. 125–136.

[77] E.A. Johnson, J.C. Ramallo, B.F. Spencer, M.K. Sain, Intelligent Base Isolation Systems, Proc. Second World Conference on Structural Control, vol. 1, no. June, pp. 367-76. 1998..

[78] J. Onoda, K. Makihara, K. Minesugi, Energy-Recycling Semi-Active Method for Vibration Suppression with Piezoelectric Transducers, AIAA journal 41, no. 4 (2003): 711-719

[79] A. Preumont, Semi-active Control, in: A. Preumont (Ed.), Vib. Control Act. Struct. Introd., Springer International Publishing, Cham, 2018: pp. 487–501.

[80] Y. Wang, D.J. Inman, Electronic Damping in Multifunctional Systems, Smart Materials, Adaptive Structures and Intelligent Systems, vol. 56031, p. V001T01A018. American Society of Mechanical Engineers, 2013.

[81] P. Wang, F. Casadei, S.H. Kang, K. Bertoldi, Locally resonant band gaps in periodic beam lattices by tuning connectivity, Phys. Rev. B. 91 (2015) 020103.

[82] N. Boechler, J. Yang, G. Theocharis, P.G. Kevrekidis, C. Daraio, Tunable vibrational band gaps in one-dimensional diatomic granular crystals with three-particle unit cells, J. Appl. Phys. 109 (2011) 074906.

[83] R.L. Harne, Y. Song, Q. Dai, Trapping and attenuating broadband vibroacoustic energy with hyperdamping metamaterials, Extreme Mech. Lett. 12 (2017) 41–47.

[84] U. Boz, M. Eriten, A numerical investigation of damping in fuzzy oscillators with poroelastic coating attached to a host structure, J. Sound Vib. 417 (2018) 277–293.

[85] L. Liu, A.D. Usta, M. Eriten, A broadband damper design inspired by cartilage-like relaxation mechanisms, J. Sound Vib. 406 (2017) 1–14.

[86] G. Han, U. Boz, L. Liu, C.R. Henak, M. Eriten, Indenter–Foam Dampers Inspired by Cartilage: Dynamic Mechanical Analyses and Design, J. Vib. Acoust. 142 (2020) 051113.

[87] N. Liu, M. Mesch, T. Weiss, M. Hentschel, H. Giessen, Infrared perfect absorber and its application as plasmonic sensor, Nano Lett. 10 (2010) 2342–2348.

[88] S. Ogawa, K. Okada, N. Fukushima, M. Kimata, Wavelength selective uncooled infrared sensor by plasmonics, Appl. Phys. Lett. 100 (2012) 21111.

[89] M.B. Zahui, K. Naghshineh, J.W. Kamman, Narrow band active control of sound radiated from a baffled beam using local volume displacement minimization, Appl. Acoust. 62 (2001) 47–64.

[90] Y. Yang, D. Xu, Q. Liu, Milling vibration attenuation by eddy current damping, Int. J. Adv. Manuf. Technol. 81 (2015) 445–454.

[91] G.J. Stein, P. Tobolka, R. Chmúrny, Ferromagnetic eddy current damper of beam transversal vibrations, J. Vib. Control. 24 (2018) 892–903.

Chapter 2 A Broadband Damper Design Inspired by Cartilage-like Relaxation Mechanisms*

Lejie Liu, Ahmet D. Usta, and Melih Eriten

*(*Reprinted from Journal of the Sound and Vibration with permission from Elsevier)*

2.1. Introduction

Absorption and trapping vibratory energy within a broadband frequency is indispensable for most man-made systems. Traditional vibration attenuation methods include isolation from the loading source, and use of active or passive vibration absorbers, impedance mismatch (reflection and redirection of vibration energy), magnetorheological fluids and viscoelastic materials for damping [1]. Those techniques require costly and heavy sets of auxiliary materials and components, yet still lack broadband effectiveness. Cellular materials such as elastomeric or polyurethane foams provide excellent shock absorption at the expense of mostly irrecoverable buckling, crushing and collapse, and hence are not suitable for mitigating sustained vibrations [2]. More contemporary damper designs achieve broadband performance by incorporating two or more of the traditional methods in semi or fully active configurations. For instance, the “e-damping” idea by Wang and Inman presents an active broadband damper design combining piezo-ceramics, oxides, polymers and elastomers in a functionally graded multilayer composite [3]. Piezo-ceramics serve as sensors and actuators in this composite, and a closed loop controller compensates for dissipation in the polymer and elastomer layers dependent on the rate and temperature. Although this active damper design increases power consumption and overall weight, it promises effective damping across wide frequency bands relevant to structural vibrations (10-200 Hz).

Frequency band gaps obtained in metamaterials and structures offer an alternative vibration suppression mechanism by stopping wave transmission at certain frequency ranges. In properly designed metamaterials, periodic arrangement of resonators (lattices) add inertia to a host system, trap vibrations locally, and thus prevent wave transmission at certain frequency bands [4–8]. Numerous research groups have demonstrated broad frequency band gaps by using fractal, granular, particle and beam-based composite metamaterials [5,9–15]. Those frequency band gaps, however, reside at higher frequency ranges than structural vibrations (>200 Hz). Several groups proposed composite metastructures with chiral and zigzag lattice geometries to localize the vibration energy and obtain effective band gaps relevant to structural vibrations [16,17]. Similar energy localization was shown to occur in dynamic systems consisting of fuzzy internal components with distributed natural frequencies [18–23]. Recent work optimizing the frequency distribution of fuzzy internal components provides experimental validation of enhanced suppression and damping performance for structural vibrations [24,25]. As in the metamaterials, these approaches require some form of dissipative interactions and/or viscoelastic materials to quickly and effectively dampen localized energy. Otherwise, reliability issues arise in the form of either structural failure at the lattice-scale or transfer of localized energy to the host structure after a short duration [20,26].

Recently, several research groups introduced a novel mechanism to enhance wave and vibration damping by adding negative stiffness to a dynamic system [27–29]. Chronopoulos et al. designed and applied negative stiffness inclusions into the composite metamaterials, and found several orders of magnitude increase in damping ratio in the low frequency range (100Hz) [30]. Harne et al. introduced so-called hyperdamping metamaterials achieving broadband energy dissipation (up to 1600 Hz) [31,32]. Furthermore, Antoniadis et al. provide theoretical framework

for the contribution of negative stiffness to broadband damping [33]. Those studies offer significant enhancement in damping magnitude, yet dismiss any discussion on rate-dependence.

In this work, we illustrate a composite damper design that yields rate-independent relaxation damping within a wide range of frequencies. This damper design is inspired by the broadband poroelastic relaxation in human and animal articular cartilage [34–38]. Poroelastic relaxations are already utilized in synthetic noise-absorbing materials, but damping efficacy in those materials is limited to high frequency excitations. Recent efforts attempt at expanding the bandwidth, especially to lower frequencies by active and passive composite systems [39–41]. One approach to ensure effective damping at both low and high frequencies is to embed mass inclusions with low resonance frequencies into the poroelastic matrix [40]. Embedded inclusions tend to move significantly under resonance conditions, and damping increases due to inclusion-matrix interactions at low frequencies. Combined with the high-frequency poroelastic relaxations, those composite dampers achieve effective damping at both ends of the frequency spectrum. Our composite damper design can be seen as an extension of this idea to continuous patch of materials rather than discrete masses. In particular, our study will demonstrate that energy dissipation in cartilage-like coatings and interfaces with hard materials spans wide frequency bands, and sandwiched damper designs with multiple contact interfaces can be optimized for rate-independent damping. Rate-independent broadband damping enables both energy absorption and mathematical tractability, and therefore offers the most ideal characteristics for structural dynamics and acoustics applications [42,43]. In the rest of the paper, we will first revisit simple mechanical models and discuss their relevance to the interfacial mechanics of poroelastic half space-hard indenter contact. Then, we will obtain rate-independent broadband damping system by optimizing the contact

patches and material properties. The assumptions and expansion of the model will be discussed at the end of the paper.

2.2. Problem Description

2.2.1. Damping in Poroelastic Interfaces

In this work, we mimic the broadband dynamic response of cartilage by a composite damper consisting of a swollen poroelastic (PE) layer sandwiched between hard plates as shown in Figure 2-1. The lower plate acts as a substrate upon which the PE layer reside, and the upper plate includes spherical protrusions with different radii contacting the PE layer. A dynamic stress (strain) is applied to the PE layer and the strain (stress) is monitored. The phase difference between the stress and strain is employed in quantification of damping. Our first claim is that one can model the dissipative properties of such a multiple contact interface system with multiple fractional Zener models shown in Figure 2-1. We will validate this claim by studying the single interface consisting of a hard spherical probe pressed on to PE layer. After the validation, we will use the multiple fractional Zener model representation to obtain optimal damping.

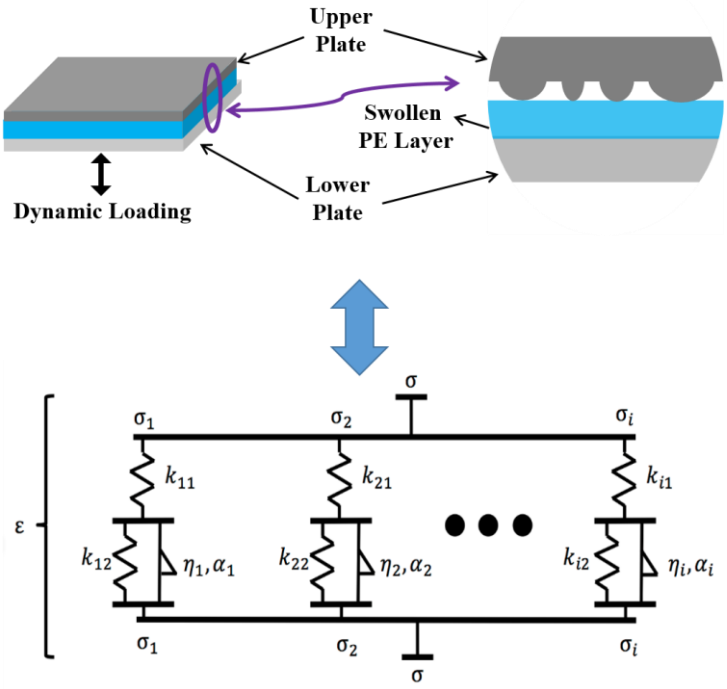

Figure 2-1: Diagram of multiple spherical protrusions in contact with the poroelastic (PE) layer (top), and its representation a multiple Fractional Zener Model (bottom).

2.2.2. Modeling of Single Interface

Relaxation of Single Fractional Zener Model

We will use a fractional Zener material (FZM) model in Figure 2-2b to simulate the single contact interface between a hard (rigid) spherical probe and a poroelastic half space shown in Figure 2-2a, and analyze the poroelastic relaxation and broadband dissipation properties of this interface.

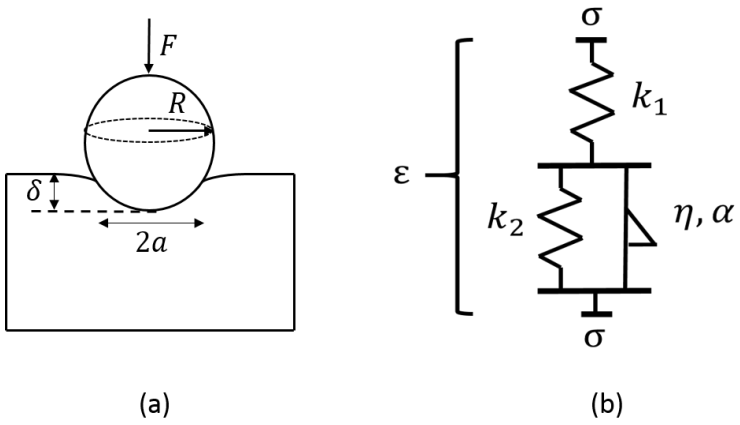

Figure 2-2: (a) A hard spherical probe in contact with a poroelastic half space, and (b) the representative single fractional Zener Model.

Stress-strain relations of a FZM can be derived as

$$\sigma + \tau_\sigma \frac{\mathrm{d}^\alpha \sigma}{\mathrm{d}t^\alpha} = M_R \left(\varepsilon + \tau_\varepsilon \frac{\mathrm{d}^\alpha \varepsilon}{\mathrm{d}t^\alpha} \right) \tag{2-1}$$

where $M_R = \frac{k_1 k_2}{k_1 + k_2}, \tau_\sigma = \frac{\eta}{k_1 + k_2}$ and $\tau_\varepsilon = \frac{\eta}{k_2}$ are relaxed modulus, and stress and strain relaxation time constants, respectively, and the fractional derivative of an arbitrary function $f(t)$ can be expressed as

$$\frac{\mathrm{d}^\alpha f(t)}{\mathrm{d}t^\alpha} = \frac{1}{\Gamma(1-\alpha)} \int_0^t \frac{f(\tau)}{(t-\tau)^\alpha} \mathrm{d}\tau \tag{2-2}$$

where Γ and α are the gamma function and order of the derivative, respectively. Note that for $\alpha = 1$, Eq. (2-1 retrieves the stress-strain relations of a standard Zener element. Stress relaxation function ψ (i.e., the stress response to a rapidly-applied constant strain) of a FZM can be found by Laplace transform pair of Eq. (2-1 as done in elsewhere [44]

$$\psi^{\alpha}(t) = M_R\left(1 - \left(1 - \frac{\tau_\varepsilon}{\tau_\sigma}\right) E_\alpha\left[-\frac{t^\alpha}{\tau_\sigma}\right]\right) H[t] \tag{2-3}$$

where E_α and H are the Mittag-Leffler and Heaviside step functions, respectively. Unrelaxed modulus can be found as

$$M_U = \lim_{t\to 0} \psi^{\alpha}(t) = M_R\left(\frac{\tau_\varepsilon}{\tau_\sigma}\right). \tag{2-4}$$

Assuming no loading or residual history before $t = 0$, we obtain the normalized relaxation function as

$$\psi_N^{\alpha}(t) = \frac{\psi^{\alpha}(t) - M_R}{M_U - M_R} = E_\alpha\left[-\frac{t^\alpha}{\tau_\sigma}\right] \tag{2-5}$$

Single FZM in Frequency Domain

To model the response of poroelastic media under broadband dynamic loading, we transform the stress-strain relation given in Eq. (2-1 to frequency-domain, and obtain the complex modulus as the ratio of stress and strain in frequency domain; i.e.,

$$M(\omega) = \frac{\sigma(\omega)}{\varepsilon(\omega)} = M_R\left(\frac{1 + (\mathrm{i}\omega)^\alpha \tau_\varepsilon}{1 + (\mathrm{i}\omega)^\alpha \tau_\sigma}\right) \tag{2-6}$$

and the loss factor (tangent) follows as

$$\zeta = \frac{\mathrm{Im}[M(\omega)]}{\mathrm{Re}[M(\omega)]} = \frac{\omega^\alpha(\tau_\varepsilon - \tau_\sigma)\sin\left(\frac{\alpha\pi}{2}\right)}{1 + \omega^{2\alpha}\tau_\varepsilon\tau_\sigma + \omega^\alpha(\tau_\varepsilon + \tau_\sigma)\cos\left(\frac{\alpha\pi}{2}\right)}. \tag{2-7}$$

The loss factor reaches maximum value of

$$\zeta_0 = \frac{\omega_0^{\alpha}(\tau_\varepsilon - \tau_\sigma)\sin\left(\frac{\alpha\pi}{2}\right)}{2 + \omega_0^{\alpha}(\tau_\varepsilon + \tau_\sigma)\cos\left(\frac{\alpha\pi}{2}\right)} \tag{2-8}$$

at

$$\omega_0 = (\tau_\varepsilon \tau_\sigma)^{-\frac{1}{2\alpha}} \tag{2-9}$$

where ω_0 is the relaxation peak frequency.

2.2.3. Validation of Single FZM Response

Relaxation Response: Simulations and Experiments

Hu et al. recently proposed normalized relaxation functions for poroelastic materials loaded by various shapes of indenters [45]. They discussed the theoretical force relaxation curves for spherical and conical indenters contacting on a gel with a fixed penetration, and solved the poroelastic contact problems in ABAQUS. In particular, the relaxation function for the spherical indenter is given as

$$g(\tau) = \frac{F(t) - F(\infty)}{F(0) - F(\infty)} = 0.491\mathrm{e}^{-0.908\sqrt{\tau}} + 0.509\mathrm{e}^{-1.679\tau} \tag{2-10}$$

where $\tau = \frac{Dt}{a^2}$, D is the diffusivity, $a = \sqrt{\delta R}$ is the contact radius at a constant indentation depth of δ as shown in Figure 2-3a, R is the radius of the spherical indenter, and $F(t)$ is the force measured. They found that the contact radius, a, mainly depends on the depth of the indentation, δ, and the relaxation function, g, only depends on the normalized time, τ. In other words, the relaxation function is a master curve based on three parameters: D, δ, and R. This master curve given in Eq. (2-10 will be compared to the normalized relaxation function $\psi_N^{\alpha}(t)$ of single FZM given in Eq. (2-5. This comparison will validate the FZM in simulating the poroelastic relaxations under spherical indentation.

We also conduct stress relaxation experiments on cartilage by performing microindentation on porcine femur cartilage, and provide further validation of the single FZM simulating PE interface response. Figure 2-3a shows a schematic of the microindentation experiments. Femur head samples are collected at the Swine Research & Teaching Center (SRTC) of the Department of Animal Sciences at the University of Wisconsin-Madison. Samples are preserved in a freezer and thawed two hours before the microindentation experiments. Prior to conducting experiments, the samples are cut into 5 mm thick slices by an EXAKT 300 precision diamond bandsaw. These slices are then glued in a Petri dish, and covered with 5% saline solution for hydration. The thickness of articular cartilage of our samples is measured as 1.1 mm. Microindentation tests are conducted on the cross-section of the cartilage approximately 550 μm below the articular surface. Circumferentially, tested locations are separated by at least 1 mm to prevent interactions between consecutive testing locations. A sphero-conical probe with 50 μm tip radius and 45^o half angle was used in the microindentation tests. Standard 2D transducer of the Triboindenter (TI-950 by Hysitron, Inc.) is employed in the tests. This transducer has high force (<1 nN) and displacement (0.02 nm) resolutions necessary for testing soft materials, and hence is well suited for testing the cartilage. In all experiments, probe displacement is imposed as a trapezoidal function with a loading segment followed by hold and unloading segments. Two maximum probe displacements, δ are used: 1 and 5 μm as shown in Figure 2-3b. Those displacements are small enough to warrant spherical indentation conditions. Loading rates and holding time for both cases were set to 5 μm/s and 360 s, respectively. Four trials were completed for each tip displacement. Indentation force and penetration time histories were recorded with a data acquisition rate of 200 Hz in all of the experiments. The tests were completed within 3 hours of sample preparation.

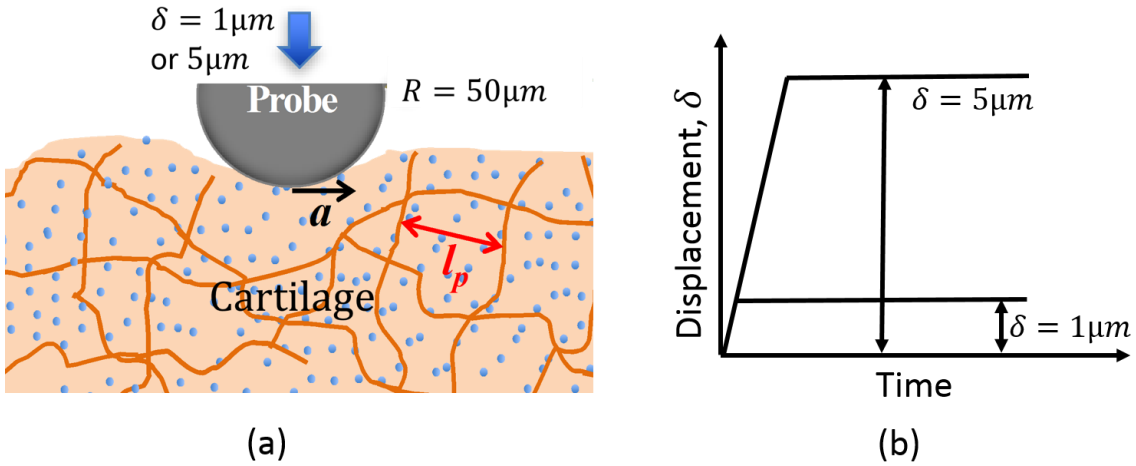

Figure 2-3: (a) Schematic of the microindentation tests conducted; (b) imposed probe displacement profile.

Dynamic Response

Nia et al. recently conducted an AFM-based nanoindentation to study the broadband dynamic response of normal and glycosaminoglycan (GAG)-depleted cartilage [36,37]. The GAG-depleted cartilage is considered as an abnormal cartilage with considerable extracellular matrix degradation that occurs at the earliest stages of osteoarthritis. The nanoindentation configuration is similar to Figure 2-3a, albeit with a probe radius of 12.5 µm. The displacement imposed on the AFM probe is a dynamic chirp signal with amplitude of about 4 nm over frequency range of 1-10000 Hz, superposed on to a mean displacement around 2-4 µm (Figure 2-4). Nia et al. reported the phase, ϕ, between the measured force and imposed displacement within the frequency range as a measure of dissipation. We will compare the empirical phase with the frequency-dependent phase of a single FZM (Eq. (2-7) to provide further validation of FZM to simulate cartilage damping across wide loading frequencies.

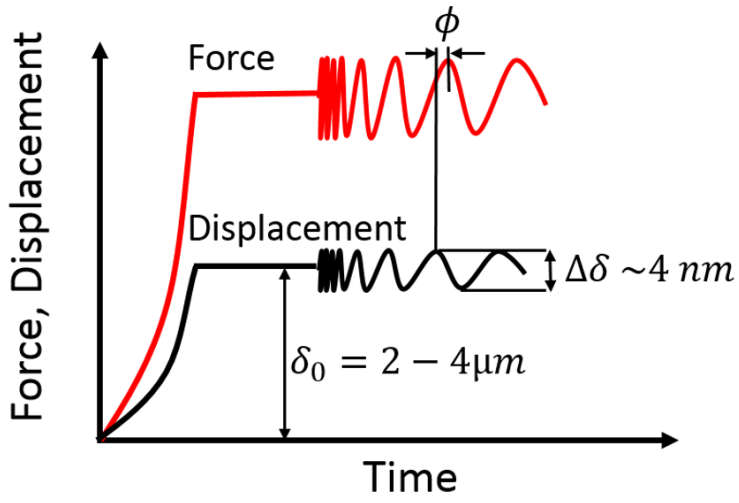

Figure 2-4: Displacement and force profiles of the dynamic nanoindentation tests conducted by Nia et al. [36,37].

2.2.4. Modeling of Multiple Interfaces and Optimization for Rate-independent Damping

Next, we will model the multiple interfaces shown in Figure 2-1 as *N*-element generalized fractional Zener model, and formulate the optimization problem for rate-independent broadband damping. The generalized Zener model in parallel configuration results in the following constitutive relation in the frequency domain

$$\sigma = M_C(\omega)\varepsilon = \sum_{l=1}^{N} M_l(\omega)\,\varepsilon = \sum_{l=1}^{N} M_{Rl}\left(\frac{1+(\mathrm{i}\omega)^{\alpha_l}\tau_{\varepsilon l}}{1+(\mathrm{i}\omega)^{\alpha_l}\tau_{\sigma l}}\right)\varepsilon \qquad (2\text{-}11)$$

where α_l, $M_{Rl} = \frac{k_{l1}k_{l2}}{k_{l1}+k_{l2}}$, $\tau_{\sigma l} = \frac{\eta_l}{k_{l1}+k_{l2}}$ and $\tau_{\varepsilon l} = \frac{\eta_l}{k_{l2}}$ are respectively the fractional derivative order, relaxed modulus, and creep and stress relaxation time constants for the l-th element, and $M_C(\omega)$ is the composite modulus of the multiple interfaces. Assuming the composite relaxed modulus M_{RC} is evenly distributed to each element, $M_{Rl} = M_{RC}/L$, so that the composite modulus

only has one coefficient M_{RC}, and this coefficient can be canceled when deal with the composite loss factor. The complex loss factor for the composite follows as

$$\zeta_C = \frac{\mathrm{Im}[\sum_{l=1}^{N} M_l(\omega)]}{\mathrm{Re}[\sum_{l=1}^{N} M_l(\omega)]} = \frac{\sum_{l=1}^{N} \mathrm{Im}[M_l(\omega)]}{\sum_{l=1}^{N} \mathrm{Re}[M_l(\omega)]}. \quad (2\text{-}12)$$

Our objective is to obtain a constant loss factor and thus damping across frequencies ranging from 3 Hz to 3 kHz. Mechanical vibrations of many aerospace, automotive and industrial structures reside within this range. The approach we present here is not limited to this particular range, yet should be repeated for a given frequency range of interest. Note that dynamic modulus of each element, $M_l(\omega)$ includes three material constants, namely α_l, $\tau_{\varepsilon l}$ and $\tau_{\sigma l}$ to be optimized to fulfill this objective. For further reduction in the number of material constants, we introduce a constant, λ to describe the ratio of $\tau_{\varepsilon l}$ to $\tau_{\sigma l}$ as $\lambda_l = \frac{\tau_{\varepsilon l}}{\tau_{\sigma l}}$, and substitute Eq. (2-9 in to Eq. (2-6 to establish a relationship between the dynamic modulus and the peak relaxation frequency, ω_{0l}, as

$$M_l(\omega) = M_{Rl}\left(1 + \frac{(\lambda_l - 1)(\mathrm{i}\omega)^{\alpha_l}}{(\mathrm{i}\omega)^{\alpha_l} + {\omega_{0l}}^{\alpha_l}\sqrt{\lambda_l}}\right). \quad (2\text{-}13)$$

If we assume α_l and λ_l are known (can be determined experimentally for a given material interface), we can simply choose numerous fractional Zener elements with different peak relaxation frequencies to develop a broadband damper. The loss factor of such damping system can be calculated by Eq. (2-12, and then the phase lag can be obtained by converting the loss factor into degrees. Next, instead of randomly picking discrete peak relaxation frequencies, we introduce a general way using the continuous distribution of the peak frequency in order to find a constant loss factor (or phase lag) from 3-3000 Hz as [46]:

$$M_c(\omega) = M_{RC}\int_0^{\infty} \Omega(\omega_0)\left[1 + \frac{(\lambda - 1)(\mathrm{i}\omega)^{\alpha}}{(\mathrm{i}\omega)^{\alpha} + {\omega_0}^{\alpha}\sqrt{\lambda}}\right] d\omega_0 \quad (2\text{-}14)$$

where $\Omega(\omega_0)$ is the probability density function (PDF) of the peak frequencies, ω_0.

Next, we use MATLAB Optimization Toolbox function "*fmincon*" to find the optimal PDF of peak frequencies yielding rate-independence and/or maximum damping over the frequency range of interest. The optimization variable is the discretized version of the PDF of peak frequencies, i.e., Ω_i. We impose two constraints on the optimization variable to satisfy PDF properties; i) all components of the PDF vector are nonzero, and ii) numerical integral of the PDF over peak frequencies yields unity. We formulate two objective functions: one for rate-independence and the other for damping magnitude. The rate of change in phase in the composite damper is chose as $f(\mathbf{\Omega}) = \sum_i^n |\phi_{i+1} - \phi_i|$ to address the former optimization. Numerical integration of Eq. (2-14, and then Eq. (2-12 is used to obtain the phase vector, $\boldsymbol{\phi}$, and compute the objective function, $f(\mathbf{\Omega})$. To maximize the damping amplitude, we utilize the summation of the reciprocal of the phase: $f(\mathbf{\Omega}) = \sum_i^n(\frac{1}{\phi_i})$. Note that other objective functions could yield similar or better results than ours. We pick those two functions to illustrate the concept. The discretization resolution, n, influences both the accuracy of the results, and computational time. To compromise both considerations, we choose n as 120 for this study. The tolerances on optimization variables and objective functions are set to 1×10^{-10}.

2.3. Results

2.3.1. Validation of Single Interface Models

Validation of Relaxation Response: Simulations and Experiments

The normalized relaxation functions for 1D loading of a single FZM (Eq. (2-5) and spherical indentation of poroelastic materials (Eq. (2-10) are compared in Figure 2-5.

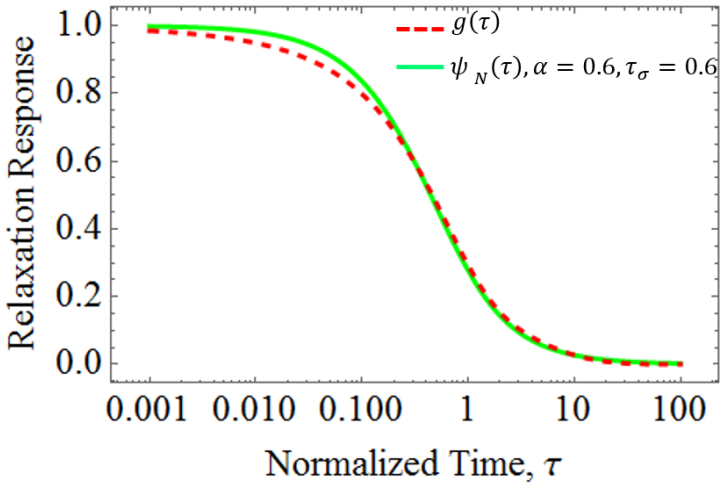

Figure 2-5: Normalized relaxation obtained from the finite element simulations ($g(\tau)$ in Eq. (2-10) and single FZM ($\psi_N(\tau)$).

By setting the derivative order α as 0.6, and stress relaxation time constant τ_σ as 0.6, we found these two curves fitted well in the entire time range. Recall that $\tau_\sigma = \frac{\eta}{k_1+k_2}$, it means by simply adjusting the parameters of a single FZM, we can simulate the relaxation response of an interface between a spherical indenter and poroelastic materials.

We further validate the relaxation response of the FZM against our microindentation tests. Figure 2-6 shows the relaxation response of porcine cartilage under microindentation of 1 and 5 μm depth. The indentation forces measured exhibit relaxation dynamics ending within the first 50 seconds of holding time. The relaxation rates change significantly at around 4 and 20 s for 1 and 5 μm depths, respectively. This suggests that multiple time scales might play a significant role in the long-term relaxation dynamics. In addition, poroviscoelastic effects commonly observed in loading of biological materials and tissues might compete with each other resulting in different mechanisms being dominant at different periods of the relaxation [47]. The fact that the change in the relaxation rate for 5 μm indentation occurs nearly 5 times later than the one for 1 μm

indentation suggests that the poroelastic relaxation dominates in those periods. Constant relaxation rates observed over 10-100 s periods are recognized as viscoelastic time constants of the cells and biological tissues [48]. Note that the poroelastic time constants, $\tau_\sigma = \frac{\delta R}{D}$. Since the same indenter tip is used for both depths, R is constant. The diffusivity, however, can be different since each indentation is conducted at a different location at the mid-section of the cartilage. Here we are assuming small variations of diffusivity at the mid-section of the cartilage, and Eq. (2-10) with a best fit $\tau_\sigma/\delta = \frac{R}{D} = 1.953$ s/μm since the indenter tip radius is 50 μm, the diffusivity estimated from the best fit is 25.6 μm^2/s (This value falls within the range of values: 19-33 μm^2/s) previously reported for porcine cartilage [49–51]. Therefore, the poroelastic time constants estimated from 1 and 5 μm indentations are 2 and 10 seconds, respectively. To illustrate the good-fit to experiments, we present the normalized relaxation force and time histories for the experimental data in Figure 2-6b. Force normalization follows Eq. (2-10), and time is normalized to indentation depths (t/δ). Therefore, the normalized time deviates from $\tau = \frac{Dt}{a^2} = \frac{Dt}{R\delta}$ in Eq. (2-10) by a factor of D/R, which can be treated as a constant in our experiments. From Figure 2-6b, we find that the experimental data for both 1 μm and 5 μm penetrations collapse in to one master curve with minor deviations between normalized time of 0.02 to 2. Then, we adjust the parameters of single Zener model response to fit the experimental master curve. Choosing the derivative order α as 0.7, and stress relaxation time constant τ_σ as 1, yields the best fit to all of the experimental data.

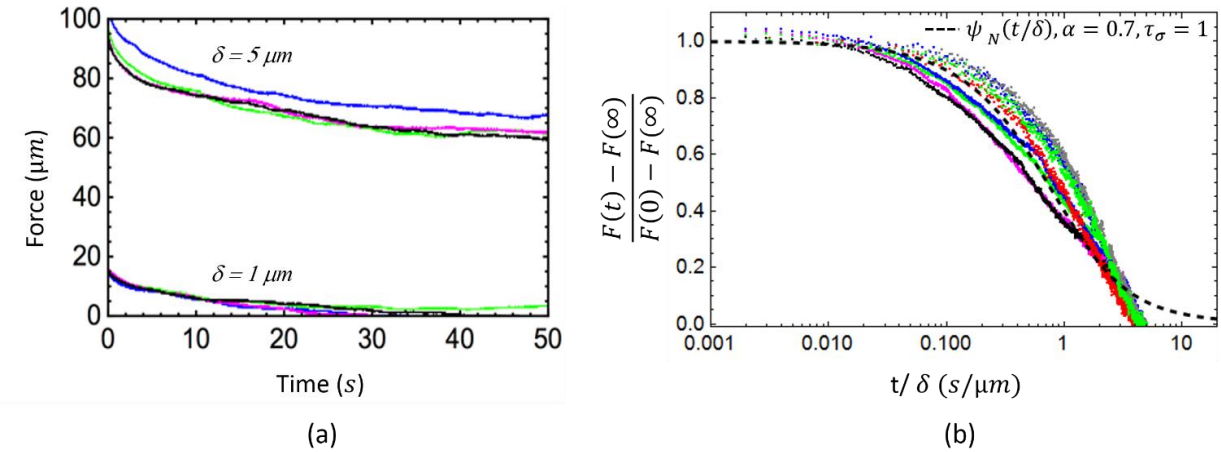

Figure 2-6: (a) Relaxation response for 1 μm and 5 μm penetration experiments; (b) normalized response of the experimental data and the single FZM results.

Validation of Dynamic Response

The broadband phase of the healthy and GAG-depleted cartilage from [37] and the FZM response fit to those data are shown in Figure 2-7. The best-fit parameters of the single FZM are given in Table 2-1. It is noteworthy that the peak relaxation frequency shifts nearly an order of magnitude to the higher frequencies upon GAG-depletion. This is mainly because the GAGs in the extracellular matrix of the cartilage attract water, and thus, depletion of them results in less water in the tissue, which then increases the diffusivity [37]. Since the relaxation time constant is $\tau_\sigma = \frac{\delta R}{D}$, increased diffusivity means higher peak relaxation frequencies. Albeit the shift in the peak relaxation frequencies, the phase magnitudes observed in healthy and GAG-depleted cartilage are similar suggesting that the damping capacity is not influenced by GAG-depletion. Noting that everyday loading of cartilage feature frequencies lower than 100 Hz, GAG-depleted cartilage does not offer ideal damping bandwidth to human musculoskeletal system. However, modification in

tissue structure and resulting changes in the peak relaxation response enables engineering a broadband damper, as we will discuss in the coming sections.

In summary, the FZM accurately reproduces both the finite element simulations on poroelastic half space, and static and dynamic indentation tests on cartilage samples. Therefore, we conclude that the single FZM is a suitable reduced-order model for the broadband dynamic responses of interfaces between hard spherical probes and poroelastic materials. Next, we utilize those reduced-order models in optimization studies to obtain rate-independent damping.

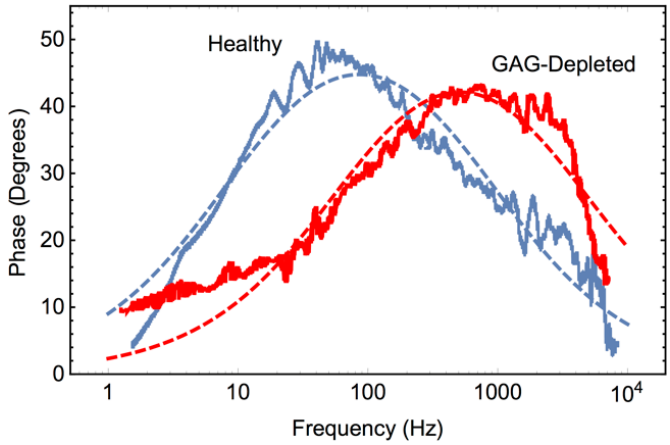

Figure 2-7: Broadband phase measurements from healthy and GAG-Depleted cartilage [37] (solid), and single FZM fitted to those measurements (dashed).

Table 2-1. Parameters of single FZM for healthy and GAG-Depleted cartilage using in Figure 2-7

Case\Parameters	τ_ε (ms)	τ_σ (ms)	α	R^2	a (μm)	f_0 (Hz)
Healthy	**54.61**	**2.33**	**0.71**	**0.99**	**5**	**86**
GAG-Depleted	**13.26**	**0.75**	**0.71**	**0.98**	**5**	**513**

2.3.2. Rate-independent Damping with Discrete Frequencies

The first exploration towards a rate-independent damping is through multiple FZM with different discrete peak frequencies (see Eq. (2-9). Equal spacing of peak frequencies in logarithmic values is previously shown to yield constant broadband damping in various other material systems [52]. Therefore, we fixed the peak frequencies equally spaced within the bandwidth of interest at 1, 10, 100, and 1000 Hz. This set of frequencies is arbitrarily chosen to provide a proof-of-concept. In other words, the chosen peak frequency set is not unique, and so another set of peak frequencies can deliver equally good or even better results in terms of rate-independency. For the value adopted in Eq. (2-13, the derivative order $\alpha_l = 0.71$ is a good approximation for the healthy cartilage. In addition, for all the cases studied in [38], creep time constant ranged between 13 and 23 times the stress relaxation time constant; i.e., $\tau_{\varepsilon l} \sim 13 - 23\tau_{\sigma l}$, andhence we assume an average value for $\lambda_l = \frac{\tau_{\varepsilon l}}{\tau_{\sigma l}} \sim 18$. Next, we set the number of fractional Zener element for 1 Hz peak frequency as 10,

10 Hz peak frequency as 10, 100 Hz peak frequency as 25, and 1000 Hz peak frequency as 75 (Figure 2-8a). Then we obtain the composite phase by using Eqs. (13) and (12), and find that it varies not more than 10% for the frequency range of interest (3-3000 Hz) as shown in Figure 2-8b. Albeit being away from optimal solution, even a simple hand picking of peak frequencies equally spaced logarithmically yields nearly rate-independent damping over 3-3000 Hz.

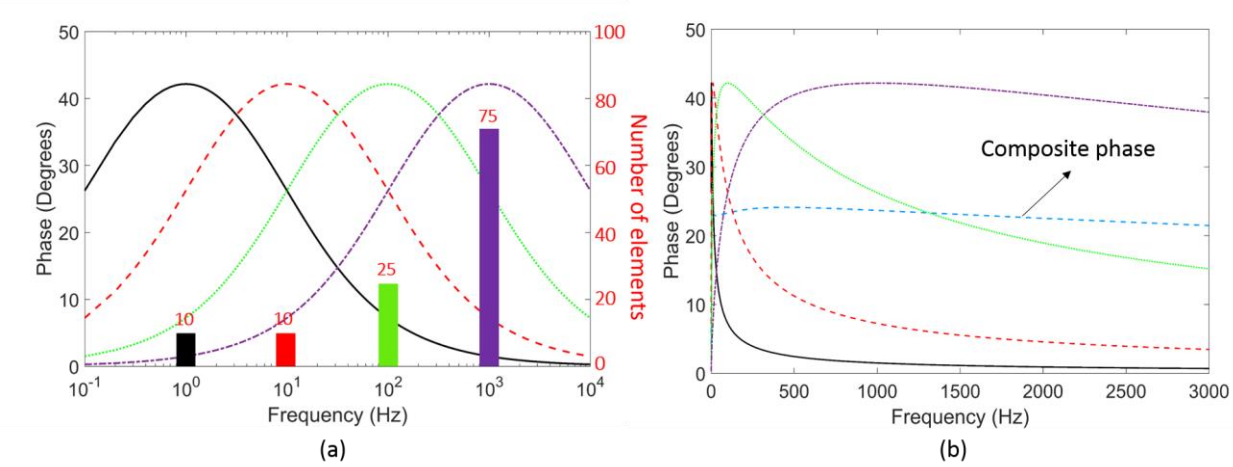

Figure 2-8: (a) Phase responses of fractional Zener elements with peak frequencies at 1, 10, 100, and 1000 Hz and the number of such elements; (b) phase responses in linear frequency scale of individual elements and the composite multiple interfaces

2.3.3. Rate-independent Damping with Continuous Frequency Distribution

Next, we will utilize the continuous formulation given in Eq. (2-14 to obtain optimum solution through an optimization routine. We choose a normal distribution function as the initial guess for the PDF of peak frequencies, and the optimal PDF we obtain is shown in Figure 2-9a. The optimal PDF has two large peak value around 3 Hz and 53 Hz, and a small peak around 3000 Hz. For all other frequencies, the optimal PDF attains very small values. In other words, in order to have the rate-independent damping system, we should have larger number of fractional Zener elements,

which have the peak frequencies near 3 Hz, 53 Hz and 3000 Hz, and small number of fractional Zener elements in all other frequencies. Figure 2-9b shows the optimal phase responses from the discrete and continuous formulations. Continuous formulation after a proper optimization routine delivers a nearly perfect rate-independence across 3-3000 Hz.

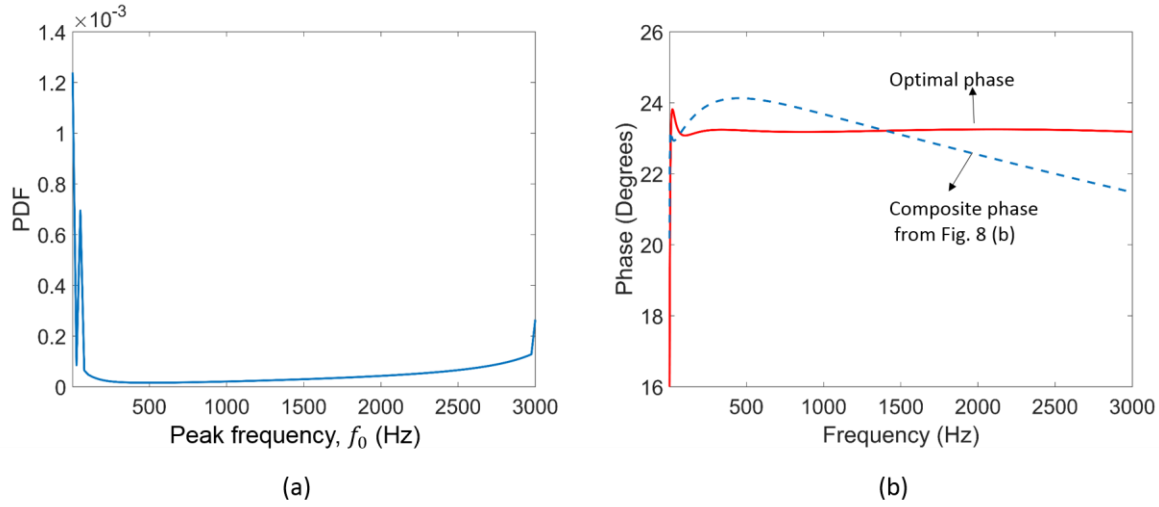

Figure 2-9: (a) Optimized PDF of peak frequencies for rate-independent damping; (b) phase responses of optimal continuous PDF and composite discrete Zener elements from Figure 2-8b.

2.3.4. Optimization of Damping Amplitude

We are also interested in maximizing the value of the phase and thus damping. We employ a different objective function to obtain the corresponding PDF of the fractional Zener elements yielding maximum damping. As shown in Figure 2-10a, the optimal PDF resembles a delta function, which indicates that we should have large number of fractional Zener elements at peak frequencies around 1000-1500 Hz. However, Figure 2-10b tells that even when we obtain larger amplitude of phase with that optimal PDF, the phase is rate-dependent especially within 3 to 500 Hz range. When we compare the optimal PDFs shown in Figure 2-9a and Figure 2-10a, the optimal

solutions yielding rate-independence and maximum amplitude in damping seem in competition. The optimal distribution for the rate-independent damping has two peaks around 3 Hz and 3000 Hz, and the distribution for the maximum damping amplitude has peaks around 1000-1500 Hz; nearly fully incompatible trends. This observation seemingly leads to the conclusion that maximizing damping while maintaining rate-independence is impossible. To verify this conclusion fully, a global optimization routine could be run where multiple objective functions are optimized simultaneously. We leave this to future work.

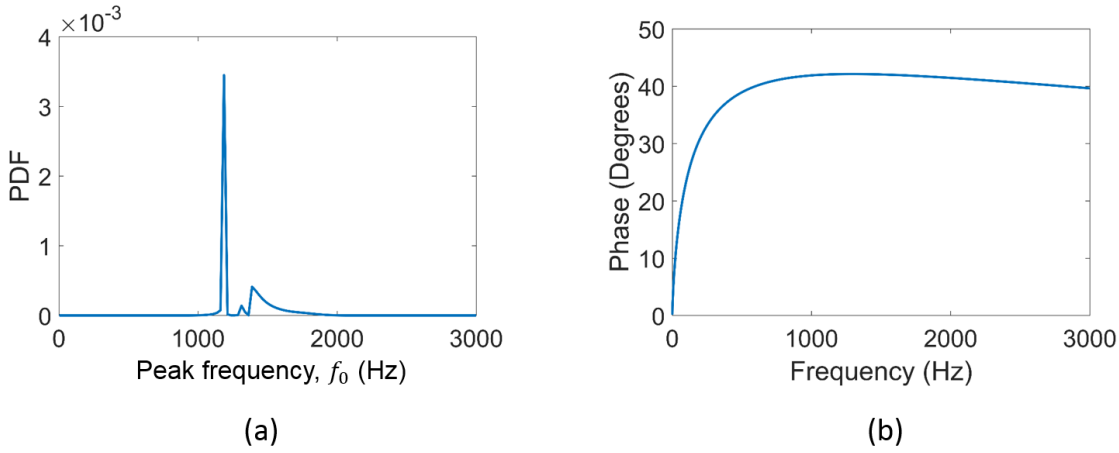

Figure 2-10: (a) Optimized PDF of peak frequencies for maximum damping amplitude; (b) phase responses of optimal continuous PDF.

2.4. Discussions

2.4.1. Selection of FZM for Simulating Broadband Relaxations

In Figure 2-5, 2-6 and 2-7, we obtain excellent correlation between the numerical/experimental data and fractional Zener models. Those curve-fit models, however, possess different fractional derivative orders, α, and stress relaxation time constants, τ_σ. This could be attributed to the differences in the materials tested. In Hu et al.'s finite element simulations [45], generic poroelastic

half spaces with a wide range of diffusivities are modeled, whereas porcine cartilage is tested in our relaxation experiments. Nia et al.'s dynamic indentation tests [37] are conducted on healthy and enzymatically GAG-depleted articular cartilage of young bovine. Several research groups also adopted FZM to model biological materials. Some groups claimed that fractional calculus can provide a concise model for the description of multiphysics and scale events that occur in biological tissues such as electrical properties of cardiac muscle [53] and anomalous diffusion in the human brain [54]. Magin et al. proposed a fractional-order model by using a parallel combination of a number of Coulomb sliding friction elements and fractional order springpots to mimic cartilage behavior in different loading conditions [55]. Davis et al. utilized similar fractional Zener models to study both the stress relaxation and creep behavior of human brain tissue observed experimentally [56]. Besides showing good correlation to experimental data from biological materials, FZM is also shown to possess an equivalent form that could be derived from molecular theory, and that could predict the macroscopic behavior of biological tissues [57]. This rich literature guided us to select FZM over other available viscoelastic models. Next, we revisit the assumptions made in curve-fitting the data to FZM.

In Figure 2-11, we present the phase angle predictions of FZM versus excitation frequency with different derivative orders and stress relaxation time constants (Eq. (2-7). We simplify the parameters as $\tau_\varepsilon \sim 18\tau_\sigma$, then use $\tau_\sigma = 2.33$ ms from Table 2-1 to obtain the responses shown in Figure 2-11a. As described in the result section, the creep time constant τ_ε always has a larger value compared to the stress relaxation time constant, τ_σ, and the range for the dynamic indentation tests on cartilage is $\tau_\varepsilon \sim 13 - 23\tau_\sigma$. This is a result of the different boundary condition of the creep and stress relaxation test, i.e., constant-displacement boundary condition for the stress relaxation experiment versus the constant-stress condition for creep test [58]. As the derivative

order increases, the phase distribution and thus the bandwidth for optimal damping become narrower. When the derivative order is 1; FZM becomes a general Zener model (standard linear solid), which yields the smallest bandwidth. Note that all of the indentation tests presented in this work (Figure 2-5, 2-6 and 2-7) exhibit broadband relaxations. Therefore, it is not surprising to see that derivative orders we obtain for the curve-fit FZM are fractional. Then, we fixed the derivative order as $\alpha = 0.71$, and varied stress relaxation time constants to obtain Figure 2-11b. As evident from the figure, increasing stress relaxation time constants have no influence on the magnitudes of phase angle, but shift the phase curves to the left. This is in line with the experimental findings presented here and elsewhere; i.e. the damping magnitude does not change but bandwidth shifts significantly. In summary, using FZM enabled us to model both broadband nature and peak relaxation bandwidths in the damping patterns of different poroelastic media.

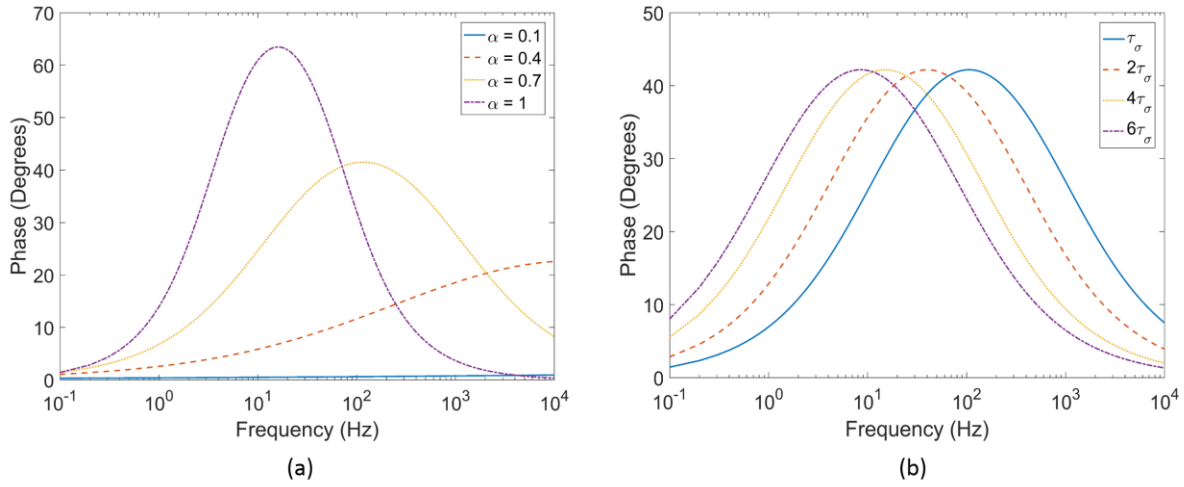

Figure 2-11: Phase angle of a given fractional Zener elements based on (a) different derivative, α, and (b) different stress relaxation time constants.

2.4.2. Assumptions Made in FZM Modeling the Spherical Indentation Responses

In this study, we employed simple FZM to model the spherical indentation response of poroelastic materials. Note that FZM is a constitutive model, and thus features stress-strain response. In other words, the change in stress under constant strain is what is referred as the relaxation response of FZM (Eq. (2-1). For the finite element simulations and experimental data we employed for validation, however, force and displacements are reported. Hence, geometry of the interfaces specific to those studies might be influential in measured response, and this could seemingly limit the applicability of our analyses. When we investigate the relaxation and broadband dynamic indentation experiments closely, one sees that the indentation depth; i.e., the distance of mutual approach of distant points in the indenter and specimen, δ, is set as a constant, thus the equivalent strain, $\varepsilon \sim \frac{a}{R} = \sqrt{\frac{\delta}{R}}$ is expected to be constant according to the indentation theory [59]. For spherical indentation, $\delta = a^2/R$. Since the radius of indenter, R, is not changed in the tests we discussed here, the contact radius, a, and area can be considered constant as well. Therefore, an equivalent stress measure of $\sigma \sim \frac{F}{a^2}$ can be considered as proportional to the force. Therefore, modeling force-displacement responses after a constitutive law such as FZM is a valid approach for the numerical simulations and tests discussed in this paper. Similar conclusions hold for the broadband dynamic indentation tests discussed. Specifically, for the experiments reported in Nia et al. [37], a mean indentation depth of around 2-4 μm is first imposed on bovine cartilage. After equilibration under that mean depth, small perturbations on the order of 4 nm is superimposed on the indentation depth. Those perturbations correspond to 0.1% of the mean depth, and using the relation $\delta \sim a^2$, lead to very small changes in both strain and contact areas (<<1%). Therefore, we can safely use a

constitutive model independent of geometry to represent the dynamic response of the interfaces between spherical probes and poroelastic materials discussed in this paper.

In the damper design process of our study, we use collection of FZMs in modeling the interface between multiple spherical protrusions and poroelastic layer as shown in Figure 2-1. This approach inherently assumes that the response of neighboring interfaces does not interfere with each other and thus can be treated independently. This, however, can only be warranted for sufficiently large spherical protrusion spacing. For linear elastic interface response under indentation, the stress field diffuses quickly away from the contact patches, and drops to negligible magnitudes at points $5a$ away from the contact patch (a is contact radius) [60]. For poroelastic interfaces, however, a similar analysis won't hold mainly due to fluid diffusion even under quasistatic loading. That diffusion process can extend up to larger areas underneath each interface and start interacting with stress-field and diffusion patterns of the neighboring interfaces. Therefore, diffusivity and corresponding peak relaxation dynamics can be altered significantly. The authors are currently addressing this problem with finite element analyses of two neighboring protrusions contacting a poroelastic half space. In the meantime, the presented results associated with the multiple interface response should be taken with precaution thanks to the independent interface response inferred in the analyses.

2.4.3. Design Considerations for a Rate-independent Damping System

In Figure 2-8b, we demonstrate rate-independent damping response obtained by combining multiple fractional Zener elements with different peak frequencies. However, the amplitude of the phase for the multiple FZM (about 25°) decreases when compared to the single element equivalent; e.g., the element that has peak frequency at 1000 Hz has maximum phase of around 40°. As evident from Eq. (2-12, the phase lag depends on the ratio of the imaginary part to the real part of the

dynamic modulus, $M(\omega)$. Typically, for a given Zener element, the ratio of Im$[M(\omega)]$ to Re$[M(\omega)]$, or the loss factor, will have the maximum value when the loading frequency, ω corresponds to the peak relaxation frequency, $\omega \sim \omega_0$. At loading rates away from the peak frequency, the loss factor will decrease significantly. Under very large loading rates; i.e., $\omega \gg \omega_0$, the fluid swelling the poroelastic media does not have sufficient time for diffusion and thus the tissue responds as an undrained elastic material, and damping is minimal. This is modeled as the dashpot in Figure 2-2b having no time to move, and hence the imaginary part of the dynamic modulus representing the dissipative component attains negligibly small values. When the loading frequency is small, $\omega \ll \omega_0$, fluid diffusion occurs but relatively low shear rates result in negligibly small dissipative forces. Therefore, the tissue responds as a fully-drain elastic material with limited energy dissipation. Figure 2-12 summarizes this physics by showing the real and imaginary parts of the dynamic modulus for Zener elements with three different peak relaxation frequencies at 10 Hz, 100 Hz, and 1000 Hz, and the composite damper the response of which is shown in Figure 2-8b. From Figure 2-9 and 2-10, we know that to build a rate-independent damper, many fractional Zener elements with peak frequencies around 3 and 3000 Hz are needed. On the other hand, the maximum damping amplitude is attained by FZMs with about 1000 Hz peak relaxation frequency. In other words, rate-independence and maximal amplitude seem mutually exclusive. This is evident from the responses shown in Figure 2-12. The imaginary part of 1000 Hz element is very close to its real curve for a wide range of frequencies within 3-3000 Hz, and thus the damping amplitude is large. However, for other elements, the ratio of imaginary to real parts is relative small, and thus the damping is small across the same frequency range. In contrast, the ratio of the imaginary and real parts of the composite response is constant but small within the same bandwidth. Therefore, rate-independence compromises damping amplitude

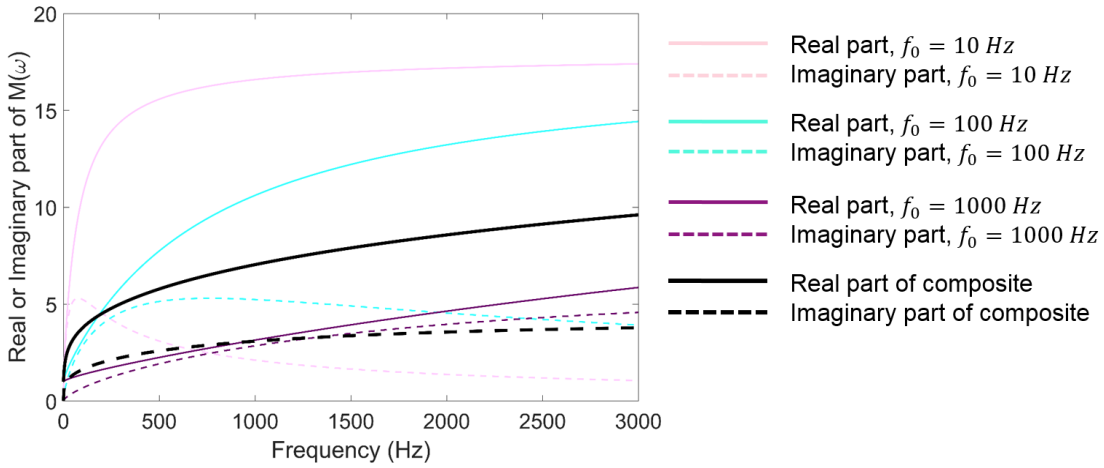

Figure 2-12: Real and imaginary part of the dynamic modulus, $M(\omega)$, for Zener elements of three different peak frequencies at 10 Hz, 100 Hz, and 1000 Hz, and along with the real and imaginary part of the composite dynamic modulus which we used to obtain phase lag in Figure 2-8b.

In the last part of the results section, we present an optimal distribution of fractional Zener elements with different peak relaxation frequencies to obtain rate-independent damping. Practical design of such an interface with multiple protrusions as in Fig.1 satisfying that optimal distribution is at minimum a challenging task. As discussed thoroughly in [36], the peak relaxation frequency, f_0, is the inverse of the poroelastic time constant, $t_s \sim \frac{a^2}{D} = \frac{R\delta}{D}$. This enables designers to relate the peak frequencies to geometry and materials properties as $f_0 \sim \frac{D}{R\delta} = \frac{D}{a^2}$. That means, by adjusting the diffusivity of the poroelastic coating, radii of the spherical indenters and indentation depths, one can obtain the desired peak frequency for a single protrusion. For instance, we can fix the diffusivity and indentation depths, and vary the radii of indenters as in Figure 2-1. Alternatively, one can tune the diffusivity to a desired peak frequency. In the result section, we used the value $D = 25.6\ \mu m^2/s$ for cartilage. As shown in Figure 2-13, the design of interfaces with multiple protrusions can be projected on to 2D maps of peak relaxation frequency and contact lengths for a given poroelastic coating; i.e., when the diffusivity is fixed. Say we are interested in rate-

independent damping over a bandwidth of lower and upper frequencies: f_{0l} to f_{0u}=$10^4 f_{0l}$, the contact lengths fall within two orders of magnitude. Note that contact lengths can be controlled by protrusion geometry albeit the difficulties in finding a common manufacturing process for creating surfaces with multiple length scales. In summary, maps as in Figure 2-13 provides design guidelines for the design of optimal sandwiched dampers proposed in this work. Note that besides changing the contact geometry or the diffusivity of the coating, temporal hierarchy in poroviscoleastic materials can be tuned with the relative concentration of the cross-links [46]. This tuning property might facilitate new damper designs especially since it is detached from the spatial hierarchy, and thus temporal response such as peak relaxation frequencies can be selected independent of fiber matrix geometry in those materials.

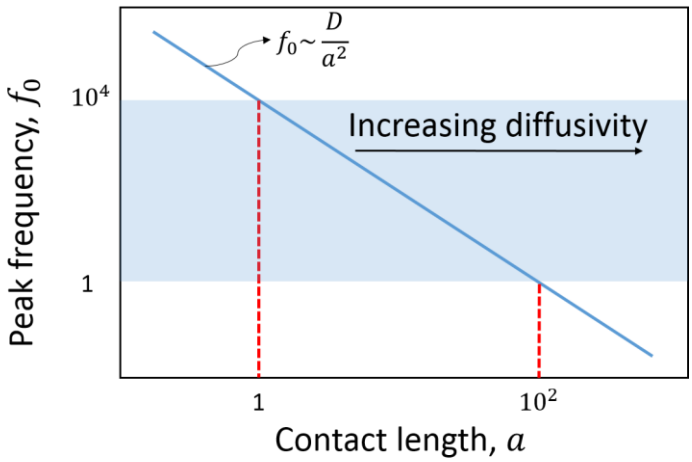

Figure 2-13: Diagram of peak frequency spectrum based on the contact length and diffusivity of the poroelastic material.

2.5. Conclusions

Inspired by cartilage, we study the dissipative properties of poroelastic materials sandwiched by hard materials. We model the hard and poroelastic materials interfaces by fractional Zener

elements; validate this approach by our experiments and published numerical and experimental data, and demonstrate that optimal damping (high amplitude or rate-independent) can be harvested from such interfaces. Key findings of the paper can be listed as follows:

- The fractional Zener models can accurately simulate the broadband dynamic response of the interfaces between hard spherical indenters and poroelastic materials.
- When designed properly, sandwiched poroelastic materials making multiple interfaces with the hard casings can exhibit rate-independent or high amplitude damping over a frequency range of interest.
- High-amplitude and rate-independent damping seems unattainable simultaneously due to compromise made by utilization of multiple dissipative interfaces.
- By relating the fractional Zener element parameters to the contact interface parameters, one can ideally design sandwiched dampers that dissipate maximum energy at a desired bandwidth of loading frequencies.
- Poroelastic materials with high diffusivities or interfaces with controlled protrusion geometries provide more flexibility in the design of sandwiched dampers.

2.6. Acknowledgment

This work is supported by the US National Science Foundation (NSF) under Grant No. NSF-CMMI-1554146. The authors also would like to acknowledge NSF for the Major Research Instrumentation enabling the acquisition and utilization of the Triboindenter in this work (grant No. NSF-MRI-DMR-1428080).

2.7. References

[1] G. Agnes, Absorbers, Active, in: S. Braun (Ed.), Encyclopedia of Vibration, Elsevier, Oxford, 2001, pp. 1–9.

[2] L.J. Gibson, M.F. Ashby, Cellular Solids: Structure and Properties, Cambridge University Press, 1999.

[3] Y. Wang, D.J. Inman, Electronic Damping in Multifunctional Systems, In ASME 2013 Conference on Smart Materials, 2013, pp. V001T01A018-V001T01A018.

[4] P. Wang, J. Shim, and K. Bertoldi, Effects of Geometric and Material Nonlinearities on Tunable Band Gaps and Low-frequency Directionality of Phononic Crystals, Phys. Rev. B, vol. 88, no. 1, p. 14304, Jul. 2013.

[5] N. Boechler, J. Yang, G. Theocharis, P. G. Kevrekidis, and C. Daraio, Tunable Vibrational Band Gaps in One-dimensional Diatomic Granular Crystals with Three-particle Unit Cells, J. Appl. Phys., vol. 109, no. 7, p. 74906, Apr. 2011.

[6] N. Boechler, J.K. Eliason, A. Kumar, A.A. Maznev, K.A. Nelson, N. Fang, Interaction of a Contact Resonance of Microspheres with Surface Acoustic Waves, Phys. Rev. Lett. 111 (2013) 036103.

[7] N. S. Boechler, Granular Crystals: Controlling Mechanical Energy with Nonlinearity and Discreteness, OhD diss., California Institute of Technology, 2011.

[8] Z. Liu, X. Zhang, Y. Mao, Y.Y. Zhu, Z. Yang, C.T. Chan, P. Sheng, Locally Resonant Sonic Materials, Science. 289 (2000) 1734–1736.

[9] V. Kunin, S. Yang, Y. Cho, P. Deymier, and D. J. Srolovitz, Static and Dynamic Elastic Properties of Fractal-cut Materials, Extreme Mech. Lett., vol. 6, pp. 103–114, Mar. 2016.

[10] E. Kim, Y. H. N. Kim, and J. Yang, Nonlinear Stress Wave Propagation in 3D Woodpile Elastic Metamaterials, Int. J. Solids Struct., vol. 58, pp. 128–135, Apr. 2015.

[11] L. Bonanomi, G. Theocharis, and C. Daraio, Wave Propagation in Granular Chains with Local Resonances, Phys. Rev. E, vol. 91, no. 3, p. 33208, Mar. 2015.

[12] G. Gantzounis, M. Serra-Garcia, K. Homma, J. M. Mendoza, and C. Daraio, Granular Metamaterials for Vibration Mitigation, J. Appl. Phys., vol. 114, no. 9, p. 93514, Sep. 2013.

[13] E. B. Herbold, J. Kim, V. F. Nesterenko, S. Y. Wang, and C. Daraio, Pulse Propagation in a Linear and Nonlinear Diatomic Periodic Chain: Effects of Acoustic Frequency Band-gap, Acta Mech., vol. 205, no. 1–4, pp. 85–103, Jun. 2009.

[14] P. Wang, F. Casadei, S. H. Kang, and K. Bertoldi, Locally Resonant Band Gaps in Periodic Beam Lattices by Tuning Connectivity, Phys. Rev. B, vol. 91, no. 2, p. 20103, Jan. 2015.

[15] A. Khanolkar, S. Wallen, M. Abi Ghanem, J. Jenks, N. Vogel, and N. Boechler, A Self-assembled Metamaterial for Lamb Waves, Appl. Phys. Lett., vol. 107, no. 7, p. 71903, Aug. 2015.

[16] E. Baravelli and M. Ruzzene, Internally Resonating Lattices for Bandgap Generation and Low-frequency Vibration Control, J. Sound Vib., vol. 332, no. 25, pp. 6562–6579, Dec. 2013.

[17] J. D. Hobeck and D. J. Inman, Magnetoelastic Metastructures for Passive Broadband Vibration Suppression, In SPIE Smart Structures and Materials+ Nondestructive Evaluation and Health Monitoring, pp. 943119-943119, International Society for Optics and Photonics, 2015.

[18] A.D. Pierce, V.W. Sparrow, D.A. Russell, Fundamental Structural-Acoustic Idealizations for Structures with Fuzzy Internals, J. Vib. Acoust. 117 (1995) 339–348.

[19] C. Soize, Vibration Damping in Low-frequency Range Due to Structural Complexity. A Model Based on the Theory of Fuzzy Structures and Model Parameters Estimation, Comput. Struct., vol. 58, no. 5, pp. 901–915, Mar. 1996.

[20] R. L. Weaver, The Effect of an Undamped Finite Degree of Freedom "Fuzzy" Substructure: Numerical Solutions and Theoretical Discussion, J. Acoust. Soc. Am., vol. 100, no. 5, pp. 3159–3164, Nov. 1996.

[21] R. L. Weaver, Mean and Mean-square Responses of a Prototypical Master/fuzzy Structure, J. Acoust. Soc. Am., vol. 101, no. 3, pp. 1441–1449, Mar. 1997.

[22] R. L. Weaver, Multiple-scattering Theory for Mean Responses in a Plate with Sprung Masses, J. Acoust. Soc. Am., vol. 101, no. 6, pp. 3466–3474, Jun. 1997.

[23] A.D. Pierce, Resonant-Frequency-Distribution of Internal Mass Inferred From Mechanical Impedance Matrices, With Application to Fuzzy Structure Theory, J. Vib. Acoust. 119 (1997) 324–333.

[24] N. Roveri, A. Carcaterra, and A. Akay, Energy Equipartition and Frequency Distribution in Complex Attachments, J. Acoust. Soc. Am., vol. 126, no. 1, pp. 122–128, Jul. 2009.

[25] A. Carcaterra, A. Akay, and C. Bernardini, Trapping of Vibration Energy into a Set of Resonators: Theory and Application to Aerospace Structures, Mech. Syst. Signal Process., vol. 26, pp. 1–14, Jan. 2012.

[26] F. Dell'Isola, D. Steigmann, A. Della Corte, Synthesis of Fibrous Complex Structures: Designing Microstructure to Deliver Targeted Macroscale Response, Appl. Mech. Rev. 67 (2016) 060804-060804.

[27] K. Idrisi, M.E. Johnson, D. Theurich, J.P. Carneal, A study on the characteristic behavior of mass inclusions added to a poro-elastic layer, J. Sound Vib. 329 (2010) 4136–4148.

[28] K. Idrisi, M.E. Johnson, A. Toso, J.P. Carneal, Increase in transmission loss of a double panel system by addition of mass inclusions to a poro-elastic layer: A comparison between theory and experiment, J. Sound Vib. 323 (2009) 51–66.

[29] D. Krattiger, R. Khajehtourian, C. L. Bacquet, and M. I., Hussein Anisotropic dissipation in lattice metamaterials, AIP Adv. 6 (2016) 121802.

[30] D. Chronopoulos, I. Antoniadis, T. Ampatzidis, Enhanced acoustic insulation properties of composite metamaterials having embedded negative stiffness inclusions, Extreme Mech. Lett. 12 (2017) 48–54.

[31] R.L. Harne, Y. Song, Q. Dai, Trapping and attenuating broadband vibroacoustic energy with hyperdamping metamaterials, Extreme Mech. Lett. 12 (2017) 41–47.

[32] J. Bishop, Q. Dai, Y. Song, R.L. Harne, Resilience to Impact by Extreme Energy Absorption in Lightweight Material Inclusions Constrained Near a Critical Point, Adv. Eng. Mater. 18 (2016) 1871–1876.

[33] I. Antoniadis, D. Chronopoulos, V. Spitas, D. Koulocheris, Hyper-damping properties of a stiff and stable linear oscillator with a negative stiffness element, J. Sound Vib. 346 (2015) 37–52.

[34] L. Han, E.H. Frank, J.J. Greene, H.-Y. Lee, H.-H.K. Hung, A.J. Grodzinsky, C. Ortiz, Time-Dependent Nanomechanics of Cartilage, Biophys. J. 100 (2011) 1846–1854.

[35] L. Han, A.J. Grodzinsky, C. Ortiz, Nanomechanics of the Cartilage Extracellular Matrix, Annu. Rev. Mater. Res. 41 (2011) 133–168.

[36] H.T. Nia, L. Han, Y. Li, C. Ortiz, A. Grodzinsky, Poroelasticity of Cartilage at the Nanoscale, Biophys. J. 101 (2011) 2304–2313.

[37] H.T. Nia, I.S. Bozchalooi, Y. Li, L. Han, H.-H. Hung, E. Frank, K. Youcef-Toumi, C. Ortiz, A. Grodzinsky, High-Bandwidth AFM-Based Rheology Reveals that Cartilage is Most Sensitive to High Loading Rates at Early Stages of Impairment, Biophys. J. 104 (2013) 1529–1537.

[38] H. Tavakoli Nia, L. Han, I. Soltani Bozchalooi, P. Roughley, K. Youcef-Toumi, A.J. Grodzinsky, C. Ortiz, Aggrecan Nanoscale Solid–Fluid Interactions Are a Primary Determinant of Cartilage Dynamic Mechanical Properties, ACS Nano. 9 (2015) 2614–2625.

[39] A.C. Slagle, C.R. Fuller, Low Frequency Noise Reduction Using Poro-Elastic Acoustic Metamaterials, in: 21st AIAACEAS Aeroacoustics Conf., American Institute of Aeronautics and Astronautics, n.d.

[40] M. R. F. Kidner, C. R. Fuller, and B. Gardner, Increase in Transmission Loss of Single Panels by Addition of Mass Inclusions to a Poro-elastic Layer: Experimental Investigation, J. Sound Vib., vol. 294, no. 3, pp. 466–472, Jun. 2006.

[41] J. P. Carneal, M. Giovanardi, C. R. Fuller, and D. Palumbo, Re-Active Passive Devices for Control of Noise Transmission through a Panel, J. Sound Vib., vol. 309, no. 3–5, pp. 495–506, Jan. 2008.

[42] A. Reggio and M. D. Angelis, Modelling and Identification of Structures with Rate-independent Linear Damping, Meccanica, vol. 50, no. 3, pp. 617–632, Mar. 2015.

[43] J.A. Inaudi, J.M. Kelly, Linear Hysteretic Damping and the Hilbert Transform, J. Eng. Mech. 121 (1995) 626–632.

[44] X. Guo, G. Yan, L. Benyahia, and S. Sahraoui, Fitting Stress Relaxation Experiments with Fractional Zener Model to Predict High Frequency Moduli of Polymeric Acoustic Foams, Mech. Time-Depend. Mater., vol. 20, no. 4, pp. 523–533, Nov. 2016.

[45] Y. Hu, X. Zhao, J. J. Vlassak, and Z. Suo, Using Indentation to Characterize the Poroelasticity of Gels, Appl. Phys. Lett., vol. 96, no. 12, p. 121904, Mar. 2010.

[46] S. C. Grindy et al., Control of Hierarchical polymer Mechanics with Bioinspired Metal-coordination Dynamics, Nat. Mater., vol. 14, no. 12, pp. 1210–1216, Dec. 2015.

[47] Z. Ilke Kalcioglu, R. Mahmoodian, Y. Hu, Z. Suo, and K. J. V. Vliet, From Macro- to Microscale Poroelastic Characterization of Polymeric Hydrogels Via Indentation, Soft Matter, vol. 8, no. 12, pp. 3393–3398, 2012.

[48] Y. Hu and Z. Suo, Viscoelasticity and Poroelasticity in Elastomeric Gels, Acta Mech. Solida Sin., vol. 25, no. 5, pp. 441–458, Oct. 2012.

[49] H. A. Leddy, S. E. Christensen, and F. Guilak, Microscale Diffusion Properties of the Cartilage Pericellular Matrix Measured Using 3D Scanning Microphotolysis, J. Biomech. Eng., vol. 130, no. 6, p. 61002, 2008.

[50] H.A. Leddy, F. Guilak, Site-Specific Effects of Compression on Macromolecular Diffusion in Articular Cartilage, Biophys. J. 95 (2008) 4890–4895.

[51] J. I. Lee, M. Sato, K. Ushida, and J. Mochida, Measurement of Diffusion in Articular Cartilage Using Fluorescence Correlation Spectroscopy, BMC Biotechnol., vol. 11, p. 19, 2011.

[52] J.M. Carcione, Wave Fields in Real Media: Wave Propagation in Anisotropic, Anelastic, Porous and Electromagnetic Media, vol. 38, Elsevier, Jan. 2007.

[53] R. L. Magin, Fractional Calculus Models of Complex Dynamics in Biological Tissues, Comput. Math. Appl., vol. 59, no. 5, pp. 1586–1593, Mar. 2010.

[54] X. J. Zhou, Q. Gao, O. Abdullah, and R. L. Magin, Studies of Anomalous Dffusion in the Human Brain Using Fractional Order Calculus, Magn. Reson. Med., vol. 63, no. 3, pp. 562–569, Mar. 2010.

[55] R. L. Magin and T. J. Royston, Fractional-order Elastic Models of Cartilage: A Multi-scale Approach, Commun. Nonlinear Sci. Numer. Simul., vol. 15, no. 3, pp. 657–664, Mar. 2010.

[56] G. B. Davis, M. Kohandel, S. Sivaloganathan, and G. Tenti, The Constitutive Properties of the Brain Paraenchyma: Part 2. Fractional Derivative Approach, Med. Eng. Phys., vol. 28, no. 5, pp. 455–459, Jun. 2006.

[57] R.L. Bagley, P.J. Torvik, A Theoretical Basis for the Application of Fractional Calculus to Viscoelasticity, J. Rheol. 27 (1983) 201–210.

[58] A. Grodzinsky, Field, Forces and Flows in Biological Systems, First ed., Garland Science, London and New York, 2011.

[59] A. C. Fischer-Cripps, Nanoindentation, Springer-Verlag, New York, 2004.

[60] K.L. Johnson, K.L. Johnson, Contact Mechanics, Cambridge University Press, Cambridge, 1987.

Chapter 3 Indenter-foam Dampers Inspired by Cartilage: Dynamic Mechanical Analyses and Design*

Guebum Han, Utku Boz, Lejie Liu, Corinne R. Henak, and Melih Eriten

*(*Reprinted from Journal of Vibration and Acoustics with permission from ASME)*

3.1. Introduction

Structures in aerospace, marine, automotive, and manufacturing industries undergo broadband vibrations and noise, which can cause material and component failure and occupational health hazards. Various techniques are available in the literature to suppress undesired vibrations and noise [1–4]. Passive methods offer robust, effective, and stable performance at relatively high frequencies, but their suppression capacity generally drops at relatively low frequencies (< 100 Hz) [5,6]. Several remedies to this reduction were proposed in the literature. For instance, Xue et al. simulated a thick layer of poroelastic materials on thin aluminum plates and demonstrated uncompromised damping capacity for low-frequencies (<100 Hz) [7]. However, this treatment utilized a passive layer with thickness 30 times that of the plate. Noting the practical challenges of such treatments, previous works had proposed adding auxiliary passive absorbers to poroelastic layers [6,8]. In general, embedding such auxiliary energy storing and dissipating systems to a host structure enhances low-frequency performance (e.g., distributed vibration absorbers). Novel materials and optimization techniques are currently available for the optimal design of these absorbers. For instance, Zuo and Nayfeh proposed a robust single degree-of-freedom (DOF) absorber by treating stiffness and damping values as control variables [9]. They also showed that a 2-DOF tuned mass-spring-damper system performed better than the single DOF system in vibration suppression [10]. In addition, previous studies showed that optimizing the frequency distribution of oscillators provided satisfactory vibration suppression [11] and nearly irreversible

energy transfer [12]. Carcaterra et al. [13] demonstrated the efficacy of oscillators on a satellite (UNISAT). However, typical limitations of undamped oscillators are a possible reversal of vibration energy to the host, leading to their early failure [14].

Interfacial and material damping mechanisms can overcome the limitations of undamped oscillators [15]. Interfacial damping involves mechanical losses due to frictional slip, microscale impacts, and relaxations localized to contact interfaces [16]. A typical example of interfacial damping is the underplatform dampers used to reduce resonances in blades of a gas turbine [17]. Rate-independent frictional interactions constitute the major mechanism of energy losses in these dampers. Material damping is dominantly observed in viscoelastic materials [18]. In particular, viscoelastic materials have been employed in sandwiched [19] and composite structures [20] to enhance damping. Bitumen-based viscoelastic damping is heavily used in automotive frames, aircraft fuselages [21], and ship decks [22]. Granular viscoelastic materials can provide the maximum damping at a targeted frequency range by using different properties of particles [23]. Although viscoelastic materials help overcome the challenges of undamped oscillators, they exhibit narrow bandwidth [18] and place maximum damping at relatively high frequencies. Therefore, they might not be useful for low structural modes (< 100 Hz) [24].

Effective damping efficacy of synthetic noise-absorbing materials is primarily limited to relatively high frequencies (> 100 Hz), and therefore recent efforts to expand the bandwidth in low frequencies were made by adding active and passive systems [5]. For example, Harne et al. attached a thin plate to a poroelastic foam layer to attenuate low-frequency vibrations [25]. Embedding mass inclusions with low resonance frequencies into a poroelastic matrix was another solution to the bandwidth problem [8]. These inclusions were designed to move significantly and thus increased damping due to inclusion-matrix interactions at low-frequency resonances.

Composite dampers combined with poroelastic damping could achieve effective damping at both ends of the frequency spectrum. Deshmukh and McKinley proposed poroviscoelastic (PVE) composites (open-cell polyurethane foam with magnetorheological fluid) as an adaptive energy-absorbing material [26].

Articular cartilage, composed of a dense solid matrix swollen by fluid, exhibits effective damping in a low-frequency range of less than 100 Hz. Effective cartilage damping in the low-frequency range stems from the combination of poroelastic and viscoelastic damping mechanisms [27]. Poroelastic damping stems from solid-fluid friction interactions in cartilage, and viscoelastic damping originates from the rearrangements of the solid fibrillary [28–30]. Therefore, poroelastic damping is dependent on the diffusivity and characteristic diffusion length in loading [27,31,32], but viscoelastic damping is length-independent. Our previous study about cartilage damping mechanisms (5 - 100 Hz) [27] showed that viscoelastic damping in cartilage provided base damping independent of characteristic diffusion lengths in loading, and poroelastic damping provided additional damping at a relatively small characteristic diffusion length in loading. Besides, our other past studies about cartilage-like dampers numerically showed that characteristic diffusion lengths in loading could be optimized to achieve rate-independent damping and maximum damping at desired frequencies (3-3000 Hz) [33,34]. These experimental [27,32,35] and simulation studies [33,34] inspired the development of cartilage-like dampers combined with multiple diffusion lengths in loading to provide effective and sustained damping in a low-frequency range (< 100 Hz). These potential benefits are a driving force behind this study. This damping method can be categorized as a hybrid of interfacial and material damping and fills in the deficiency of damping methods for a low-frequency range.

This study aims to demonstrate a practical realization of cartilage-inspired PVE dampers that provide maximum damping at desired frequencies and rate-independent broadband damping in a relatively low-frequency range (< 100 Hz). Cartilage-inspired PVE dampers are designed with indenter-foam configurations for a low-frequency range of 0.5 - 100 Hz. The PVE dampers in a single-indenter-foam configuration (singe diffusion length in loading) are investigated through dynamic mechanical analysis (DMA) to quantify the effects of indenter radii and mean pore sizes on their damping capacity and show the ability to place maximum damping at desired frequencies (narrowband performance). Based on the results of single-indenter-foam dampers, we design and test the optimized PVE damper in a two-indenter-foam configuration (two diffusion lengths in loading) that provides nearly rate-independent damping capacity (broadband performance). Section 3.2 summarizes our recent findings on effective cartilage PVE dissipation in a low-frequency range, conducts a scaling analysis to be used in the designs and analyses of cartilage-inspired foam-indenter dampers, and presents the experimental details on the DMA of the dampers. Section 3.3 presents the damping performance of single- and two-indenter-foam dampers. Section 3.4 discusses the assumptions used in the scaling analysis and challenges before the actual implementation of cartilage-inspired PVE dampers on real structures. Section 3.5 concludes this study with a summary of the findings.

3.2. Theory and Methods

3.2.1. PVE Damping of Cartilage

Our previous work uncoupled cartilage damping mechanisms by using the dependence of poroelastic damping on a characteristic diffusion length involved in the mechanical load on the tissue (Figure 3-1) [27]. The characteristic length was a contact radius between a rigid indenter and hydrated cartilage (Figure 3-1a). Phase lags δ between applied strains and measured stresses

were measured at different contact radii; δ is a measure of damping and can be converted into the specific damping capacity $\varphi = 2\pi \tan\delta$ [18]. The frequency f_{peak} at which the phase lag attains a maximum value due to the maximized poroelastic damping was governed by the combination of the diffusivity of a material β and contact radius a ($f_{peak} \sim \frac{\beta}{a^2}$) (Figure 3-1b) [27,32,35]; f_{peak} is referred to as a poroelastic peak damping frequency in the next subsection, and β represents the diffusion rate of a solvent in a porous media. This result indicated that damping at a targeted frequency can be maximized by placing f_{peak} at the targeted frequency via the adjustment of β and a. The previous study also showed that viscoelastic damping can provide base damping regardless of contact radii

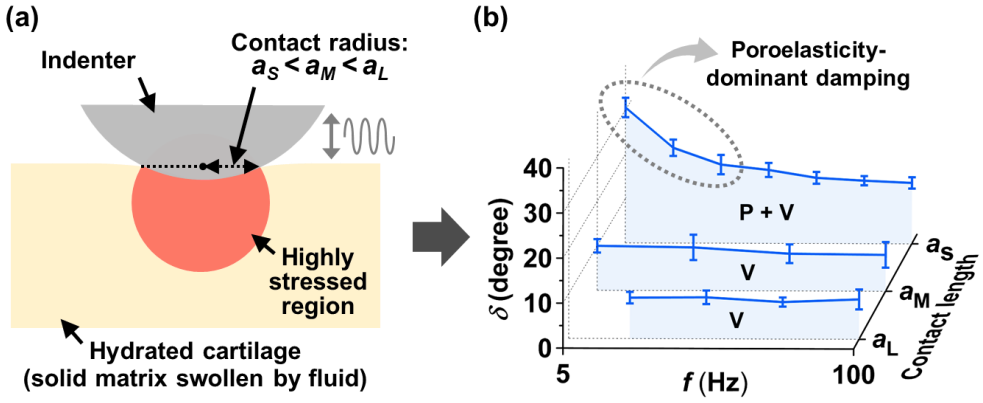

Figure 3-1: (a) Experimental setup for cartilage damping measurement and (b) results of cartilage damping (P: poroelastic damping and V: viscoelastic damping) at different characteristic lengths (a_S: ~ 13 μm, a_M: ~ 33 μm, and a_L: ~ 43 μm). Effective cartilage damping in a frequency range of 5 – 100 Hz originates from the combination of poroelastic and viscoelastic damping mechanisms. While viscoelastic damping provides sustained base damping regardless of contact radii (a_S, a_M, and a_L), poroelastic damping additionally increases damping at a relatively small contact radius (a_S). The poroelastic peak damping frequency f_{peak} is governed by the diffusivity of a material β and contact radius a ($f_{peak} \sim \frac{\beta}{a^2}$) [27,32,35]. This figure is not drawn to scale.

3.2.2. Analyses and Designs of Indenter-foam Damper

We first design an indenter-foam damper that mimics cartilage-like PVE damping mechanisms. The damper consists of a flat-ended cylindrical rigid indenter pressed on a viscoelastic foam sheet swollen with a Newtonian liquid (Figure 3-2a). A characteristic diffusion length in an indenter-foam damper is controlled by changing a contact radius *a* between an indenter and a foam sheet, similar to our previous study about cartilage dissipation mechanisms (Section 3.2.1). Contact loading creates a gradient-stress profile that leads to large volumetric strains in the vicinity of the contact region and relatively low strains far from the contact region. These volumetric strains cause liquid diffusion and hence poroelastic losses (solid-fluid frictional interaction) close to the contact region. Viscoelastic damping of the foam is responsible for energy dissipation close to and far from the contact region. However, indentation-induced shear strains are generally significantly smaller than volumetric strains, and so are viscoelastic losses [40]. A simple mechanical model of this indenter-foam system neglecting viscoelastic losses is given in Figure 3-2b. In this model, the highly stressed region close to the contact region is modeled as a linear elastic zone with Young's modulus E combined with poroelastic damping η_l; where η_l stems from the solid-liquid interaction (Kelvin-Voigt material). The region surrounding the highly stressed zone is modeled as linear elastic with the same Young's modulus of solid foam E because poroelastic interactions away from the contact are negligible due to diffused stresses. Thus, a standard linear solid element could represent the total response of the indenter-foam system. Small vibration amplitudes are assumed in the mechanical model of the indenter-foam system. Imposing harmonic loading with single frequency ω in the form of harmonic stress $\sigma = \sigma_M e^{i\omega t}$ (or strains $\varepsilon = \epsilon_M e^{i\omega t}$; $\varepsilon_0 = \epsilon_0 e^{i\omega t}$) in the following constitutive relations:

$$\sigma = E(\varepsilon - \varepsilon_0) + \eta_l(\dot{\varepsilon} - \dot{\varepsilon}_0) = E\varepsilon_0 \,. \tag{3-1}$$

This simple model yields two constitutive relations:

$$\sigma_M = (E + i\omega\eta_l)(\epsilon_M - \epsilon_0) = E\epsilon_0 \tag{3-2}$$

where σ_M and ϵ_M are the steady-state amplitudes of stress and strain at the foam-indenter contact, respectively, and ϵ_0 is the steady-state amplitude of strain at the end of the highly-stressed zone. Eliminating ϵ_0 using the equalities in Eq. 3-2 delivers

$$\sigma_M = \frac{E(E + i\omega\eta_l)}{2E + i\omega\eta_l}\epsilon_M \tag{3-3}$$

which is the relation for total stress-strain response of the foam-indenter system. Since this relation is similar to a constitutive equation at the steady-state, the terms in front of ϵ_M is referred to as dynamic modulus $G(\omega) = \frac{\sigma_M}{\epsilon_M} = \frac{E(E+i\omega\eta_l)}{2E+i\omega\eta_l}$. When normalized to the total foam modulus $E/2$, this modulus takes the following form:

$$G_N(\omega) = \frac{G(\omega)}{E/2} = \frac{1 + i\omega\tau_{PE}}{1 + i\omega\frac{\tau_{PE}}{2}} \tag{3-4}$$

where $\tau_{PE} = \frac{\eta_l}{E}$ is the poroelastic relaxation time constants. The argument of the dynamic modulus yields the phase lag δ between stress and strain as follows:

$$\delta(\omega) = \angle G_N(\omega) = \arctan \omega\tau_{PE} - \arctan \omega \frac{\tau_{PE}}{2} \qquad (3\text{-}5)$$

The phase lag is a common measure of material damping [18] and is used to measure the damping capacity of the foam-indenter system; the specific damping capacity φ can be calculated from the phase lag ($\varphi = 2\pi \tan\delta$) [18]. The phase lag given in Eq. 3-5 attains maximum at $\omega_{peak} = 2\pi f_{peak} = \sqrt{2}/\tau_{PE}$; i.e., when loading period is around the poroelastic relaxation time constant. In the remainder of this paper, we will refer to the loading frequency that yields the maximum phase lag and thus damping as a poroelastic peak damping frequency f_{peak}.

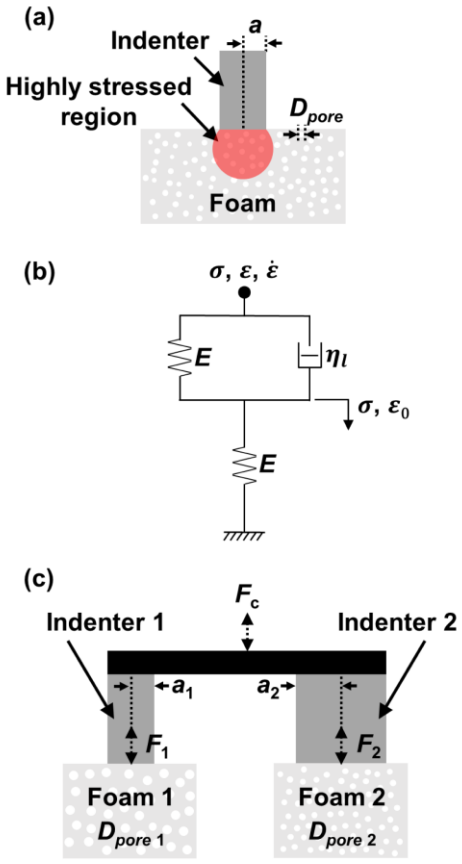

Figure 3-2: (a) Single-indenter-foam configuration, (b) its mechanical model, and (c) two-indenter-foam configuration. Foam sheets are swollen by fluid. The damping capacity of indenter-foam dampers, inspired by cartilage mechanisms, can be tuned by controlling the

contact radius *a*, pore diameter D_{pore}, and the number of indenters. *a* is a characteristic diffusion length in an indenter-foam damper. This figure is not drawn to scale.

Next, we study the kinematics and swollen foam's response to the indenter oscillations in the vicinity of the contact region (i.e., highly stressed zone); obtain an expression for liquid damping coefficient η_l and thus relate the peak damping frequency to the physical properties of the damper system (i.e., $f_{peak} \cong \frac{1}{\sqrt{2}\pi\tau_{PE}} = \frac{E}{\sqrt{2}\pi\eta_l}$). First, the highly stressed region in the vicinity of the rigid indenter is assumed to occupy a volume V that scales with the cube of indenter radius (i.e., $V \propto a^3$ as predicted by the linear elastic contact theories [36]). The rate of the volume change in that region due to the dynamic motion of the rigid indenter can be approximated as $\frac{dV}{dt} \propto -\dot{\varepsilon}_{PE}a^3$ where compressive strain rates on the poroelastic dashpot $\dot{\varepsilon}_{PE}$ are taken as positive. The average volumetric flux q and liquid velocity v_l out of that highly stressed zone scales with $q \approx v_l \propto \frac{1}{a^2}\frac{dV}{dt} \propto -\dot{\varepsilon}_{PE}a$. Note that the high porosity in the foam and the incompressibility of the swelling liquid are inherently assumed in equating the flux to the liquid velocity. Assuming the diffusion of the liquid obeys Stokes' flow, Darcy's law relates stress-gradients to liquid velocity (i.e., $v_l \propto -\frac{k}{\mu}\frac{\sigma_{PE}}{a}$). In this expression, k is the permeability of the foam (known to scale quadratically with the mean pore diameter D_{pore} in various foam sheets (i.e., $k \propto D_{pore}^2$ [37]), μ is the dynamic viscosity of the swelling liquid, and $\frac{\sigma_{PE}}{a}$ gives an estimate of gradients of stress carried by the poroelastic dashpot element. Relating the liquid velocity scaling from kinematics and the liquid diffusion yields the relation between the stress and strain rates on the poroelastic dashpot:

$$\sigma_{PE} \propto \mu \left(\frac{a}{D_{pore}}\right)^2 \dot{\varepsilon}_{PE} \tag{3-6}$$

Therefore, the liquid damping coefficient $\eta_l \propto \mu \left(\frac{a}{D_{pore}}\right)^2$, and so the peak damping frequency is found to scale as:

$$f_{peak} \cong \frac{E}{\sqrt{2}\pi\eta_l} \propto \frac{E}{\sqrt{2}\pi\mu}\left(\frac{D_{pore}}{a}\right)^2 \tag{3-7}$$

Note that this scaling law can be rewritten as $\frac{\beta}{a^2} = \frac{E}{\sqrt{2}\pi\mu}\left(\frac{D_{pore}}{a}\right)^2$ where $\beta = \frac{ED_{pore}^2}{\sqrt{2}\pi\mu}$ is a measure of diffusivity in the foam. Therefore, the peak damping frequency obtained from the indenter-foam damper model obeys the same scaling with the peak damping frequency of cartilage. Beyond this highly stressed zone dominated by poroelastic losses, viscoelastic losses stemming from solid foam deformation provide baseline dissipation also observed in cartilage. Note that those losses are not accounted for in the simple mechanical model. Since viscoelastic losses do not exhibit length dependence, their contribution to peak-damping frequencies in the foam-indenter system is negligible. In conclusion, the indenter-foam system promises damping capacity similar to articular cartilage.

The scaling law obtained in Eq. 3-7 indicates that the peak damping frequency depends on material constants (the ratio of Young's modulus of the foam to the dynamic viscosity of the liquid) and geometric properties (the ratio of mean pore diameter to indenter radius). We choose to primarily vary the latter in the indenter-foam damper designs to confirm the tunability of the peak

damping frequency in a range of 0.5 - 100 Hz, which results from the quadratic scaling with the geometric ratio $\frac{D_{pore}}{a}$.

Our recent numerical study showed that cartilage-like PVE dampers with multiple diffusion lengths in loading can offer rate-independent broadband damping [33]. Here, we experimentally validate this numerical study by designing a two-indenter-foam configuration (two diffusion lengths in loading) as shown in Figure 3-2c. Note that the panel connecting the two indenters is rigid, and the composite force F_c is treated as the vibration transmitted from a target structure to the two-indenter-foam damper. Consistent with our numerical work, we ensured that the indenters were sufficiently far from each other, the response of the foam was linear PVE so that it obeyed the same scaling law (Eq. 3-7) as in the single-indenter case. Consequently, the principle of superposition can be applied to the two-indenter-foam configuration. Therefore, the forces F_1 and F_2 carried by each indenter-foam configuration can be summed to obtain the composite force F_c. As the rigid indenters (Figure 3-2c) oscillate sinusoidally, the composite force can be represented as

$$F_c(\omega) = A_1(\omega)\sin(\omega t + \delta_1(\omega)) + A_2(\omega)\sin(\omega t + \delta_2(\omega)) \tag{3-8}$$

where $A_1$and A_2 are the amplitudes, and δ_1 and δ_2 are the phase lags for F_1 and F_2, respectively. It is possible to find the composite phase and amplitude behavior as a single sine wave by substituting Eq. 3-8 in

$$F_c(\omega) = A_c(\omega)\sin(\omega t + \delta_c(\omega)) \tag{3-9}$$

where A_c is the composite amplitude, and δ_c is the composite phase lag (frequency-dependence in amplitudes and phase lags are dropped for brevity). Then, A_c and δ_c are related to A_1, A_2, δ_1, and δ_2 as follows:

$$A_c = \sqrt{[A_1 \sin(\delta_1) + A_2 \sin(\delta_2)]^2 + [A_1 \cos(\delta_1) + A_2 \cos(\delta_2)]^2} \quad (3\text{-}10)$$

$$\delta_c = \sin^{-1}([A_1 \sin(\delta_1) + A_2 \sin(\delta_2)]/A_c) \quad (3\text{-}11)$$

Eqs. 3-10 and 3-11 yield $A_c = 2A_1$ and $\delta_c = \delta_1$ for identical indenter-foam pairs, as expected physically. Note that we used forces and stresses interchangeably in the analyses of single- and two-indenter-foam configurations. This is possible only for complete contacts where load-bearing contact areas are independent of loading. Therefore, the forces and stresses relate through a constant, and hence scaling laws are unaltered. In the following experiments, we control the deformation imposed on the indenter-foam dampers, measure forces, and calculate phase lags as a measure of damping capacity.

3.2.3. Experimental Details

We performed DMA on 12 different single-indenter-foam configurations (four types of foams × three indenter radii) and one two-indenter-foam configuration. DMA is a testing method to measure dynamic mechanical and dissipative properties of materials. Three foams (D_{pore} = 50, 90 and 200 μm) were made of polyethylene (PE) and the other (D_{pore} = 200 μm) was made of PE-based olefin (INOAC Corp., Troy, MI). The foams were cut into circular sheets (22 mm in diameter and 2 mm in thickness) and immersed in extra virgin olive oil ($\mu = 0.084\ Pa \cdot s$ [38]) for more than 24 hours before testing. A universal tester (TA ElectroForce MODEL3200; TA Instruments,

Eden Prairie, MN) was used to conduct DMA on the foams swollen in olive oil. This tester was equipped with force and displacement sensors along with data acquisition systems to monitor the dynamic normal force and displacement. Aluminum flat-ended cylindrical indenters with different radii (a = 4.75 mm, 3.15 mm, and 1.9 mm) were used to generate different contact radii. The contact radii served as characteristic diffusion lengths in loading.

Twelve single-indenter-foam configurations (Figure 3-3a and Eq. 3-7) were characterized to show the tenability of a peak damping frequency. The scaling law ($0.0001 < \left(\frac{D_{pore}}{a}\right)^2 < 0.01$ via Eq. 3-7) predicts that the combination of the three mean pore diameters and three indenter radii (12 cases) promises two orders of magnitude variation in the peak damping frequency in a single-indenter-foam configuration.

An optimal two-indenter-foam configuration (Figure 3-3b and Eqs. 3-10 and 3-11) was tested to validate whether it can provide rate-independent damping capacity. The optimal two-indenter-foam configuration was selected by applying a search criterion to the combined responses (Eqs. 3-10 and 3-11) of two single-indenter-foam configurations. In this combined configuration (Figure 3-3b), a 30 mm gap was left between the centers of the rigid flat punches to minimize interactions, which ensures the applicability of the superposition principle (Eq. 3-8). The selection of the gap complied with the literature showing minimal interaction effects in poroelastic contacts separated by five times the contact radius [39].

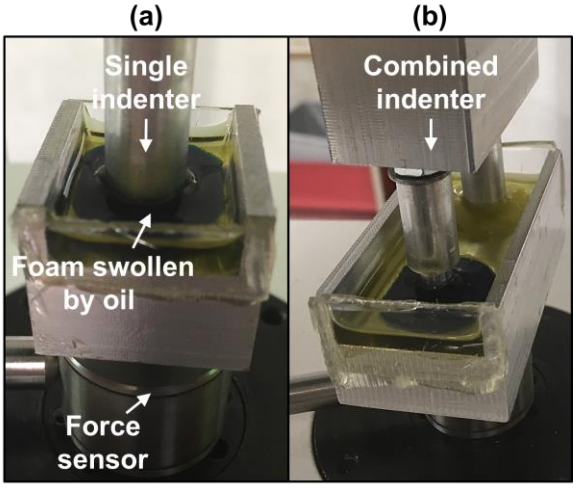

Figure 3-3: Images of cartilage-like PVE dampers: (a) single-indenter-foam configuration and (b) two-indenter-foam configuration. Foam sheets were immersed in olive oil during tests. The single-indenter-foam configuration was developed to demonstrate the tenability of the peak damping frequency via indenter radii *a* and pore diameters D_{pore}. The two-indenter-foam configuration was created to demonstrate the rate-independent damping capacity via multiple diffusion lengths in loading.

DMA was performed in a frequency range of 0.5 – 100 Hz by applying displacement-controlled oscillations to indenter-foam dampers, measuring reaction forces, and calculating phase lags between displacements and reaction forces. A static displacement of 180 μm was applied to the indenter and was held for four minutes for full relaxation. Then harmonic displacements with amplitudes of around 20 μm were applied. The static displacement was employed to ensure proper contact during tests and sufficient distance from the lower boundary of a sample. The amplitude of the harmonic indentation induced high enough excitation compared to the noise floor of the force sensor while assuring nearly linear PVE behavior (i.e., linear elastic foam response + predominantly 1D radial flow of liquid phase) for all indenter-foam configurations. We varied the excitation frequency of the harmonic indentation (f = 0.5, 1, 2, 5, 10, 20, 30, 50, 75 and 100 Hz)

to examine dissipative responses of foams. Two DMA measurements were performed at each frequency. Each measurement lasted for at least 59 cycles, and the last five cycles of displacement and corresponding force data were used to obtain the hysteresis loops (Figure 3-4c) and phase lags δ; i.e., a measure of damping capacity [18]. The number of cycles before the last five cycles was sufficient to reach equilibrium (Figure 3-4a and b). There is a minor asymmetry between the loading and unloading portions of the hysteresis loops (Figure 3-4c). It might stem from possible asymmetry in compression-tension response of the foams. The asymmetry remains minor for all the frequencies tested and thus is not expected to influence the damping capacity and tuning of the tested dampers. The average and standard deviation of 10 cycles (five cycles from each of the two tests) were reported. Figure 3-4 shows representative raw and processed DMA data. All the data was measured at the signal-to-noise ratios of more than 31 dB for the displacement data and more than 29 dB for the force data. Therefore, the level of noise is negligibly small in the recorded measurements. The raw data was processed through 4th-order lowpass Butterworth and zero-phase filters using MATLAB (The MathWorks, Inc., Natick, MA). When an excitation frequency was greater than or equal to 0.5 Hz, a filter cutoff frequency was set as 2.8 times an excitation frequency; otherwise, a cutoff frequency was set as 1 Hz. The filtfilt command of MATLAB was used to perform zero-phase filtering.

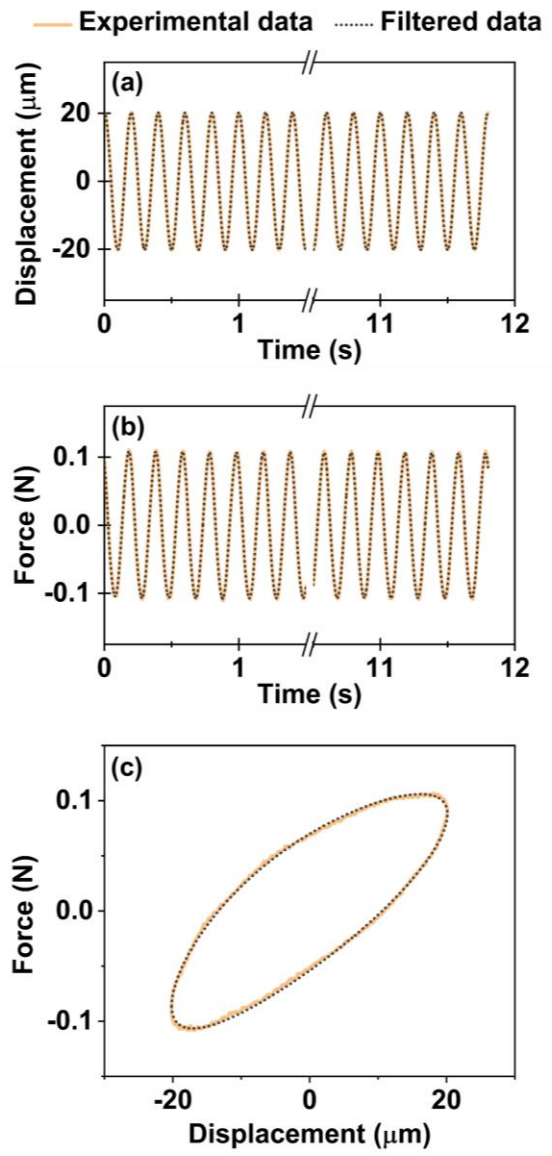

Figure 3-4: Representative DMA results: (a) applied displacement, (b) measured force, and (c) hysteresis loop (single cycle). The results were taken from a PE foam sheet with D_{pore} = 50 μm using a single indenter with a = 4.75 mm at a frequency of 5 Hz.

3.3. Results

3.3.1. Single-indenter-foam Configuration for Tunable Peak Damping Frequencies

The peak damping frequency of the single-indenter-foam damper was tunable across two decades by changing the combination of the pore diameter D_{pore} and indenter radius a (Figure 3-5). The damping capacity of all the dampers was frequency-dependent, had a peak value, and reached a base value about two decades from the peak value. The various indenter-foam combinations generated the cartilage-inspired PVE dampers with different diffusion coefficients and characteristic diffusion lengths in loading. The alterations in a diffusion length and diffusivity enabled to shift the peak damping frequency across two decades. Regardless of the pore diameter, as the contact radius decreased, the peak damping frequency moved toward relatively high frequencies. For example, in the case of the PE foam with a pore diameter of 50 μm (Figure 3-5a), the peak damping frequency shifted from 1 to 5 Hz as the contact radius decreased from 4.75 mm to 1.9 mm. For a given contact radius, as the pore diameter increased, the peak damping frequency attained a higher value. For instance, when the pore diameter increased from 50 μm to 200 μm (Figure 3-5a-c), the peak damping frequency at a 4.75 mm contact radius shifted from 1 to 30 Hz. These observations were in line with the trend of a peak damping frequency observed in cartilage. They also indicated that a peak damping frequency can be placed at a targeted frequency by controlling the diffusion and characteristic diffusion length in loading.

The tunability of the peak damping frequency in a single-indenter-foam was governed by the scaling law (Eq. 3-7). For a given form material (fixed pore diameter D_{pore}), when the frequency axis was scaled with the square of the contact radius a^2, the damping capacity curves moved closer to each other (Figure 3-6a-d). As for the PE foam with a pore diameter of 50 μm, the peak damping frequencies, spanning a decade from a = 4.75 mm to a = 1.9 mm (Figure 3-5a), virtually collapsed

into a point after scaling (Figure 3-6a). Furthermore, scaling the frequency axis with the square of the ratio of a contact radius to a pore diameter $\left(\frac{a}{D_{pore}}\right)^2$ nearly collapsed all the phase lag versus frequency curves. While the ratio of the highest to the lowest peak damping frequencies was around 100 before the scaling (Figure 3-5a and d), the ratio reduced to 4 after the scaling as illustrated by the two vertical red lines in Figure 3-6e-h. Consequently, all the curves were centered in the vicinity of $f\left(\frac{a}{D_{pore}}\right)^2 \cong 2\times10^4$ Hz and formed a master damping capacity curve. The consistency with the scaling law demonstrated that the dominant damping mechanism around the peak damping frequencies stemmed from poroelastic damping (solid-fluid interactions). Similar to cartilage damping mechanisms [27], viscoelastic damping was likely to provide damping in the tails of the damping capacity curves. Furthermore, according to the scaling law, the peak damping frequency after the scaling should be on the same order as the ratio of Young's modulus of the foams to the dynamic viscosity of the olive oil (i.e., $f_{peak}\left(\frac{a}{D_{pore}}\right)^2 \propto \frac{E}{\sqrt{2}\pi\mu}$). When taking the dynamic viscosity of the extra virgin olive oil as $\mu = 0.084\ Pa\cdot s$ [38], the scaling law leads to $E \propto \sqrt{2}\pi\mu f_{peak}\left(\frac{a}{D_{pore}}\right)^2 \cong 10$ kPa. The storage moduli, estimated from the raw stress-strain data at 0.5 Hz, range from around 111 kPa to around 2303 kPa for all the indenter-foam configurations. Therefore, the proportionality constant to turn the scaling argument for the peak damping frequencies to an approximation for the measured values ranges from 11.1 to 230.3. Given the omission of several proportionality constants and assumptions made throughout the scaling argument, this range of proportionality constants is acceptable (see the Discussion section for details of those assumptions). A poroelastic peak damping frequency governed by the scaling law

showed that a single-foam-indenter PVE damper has damping mechanisms mimicking cartilage and thus can be called a cartilage-like damper.

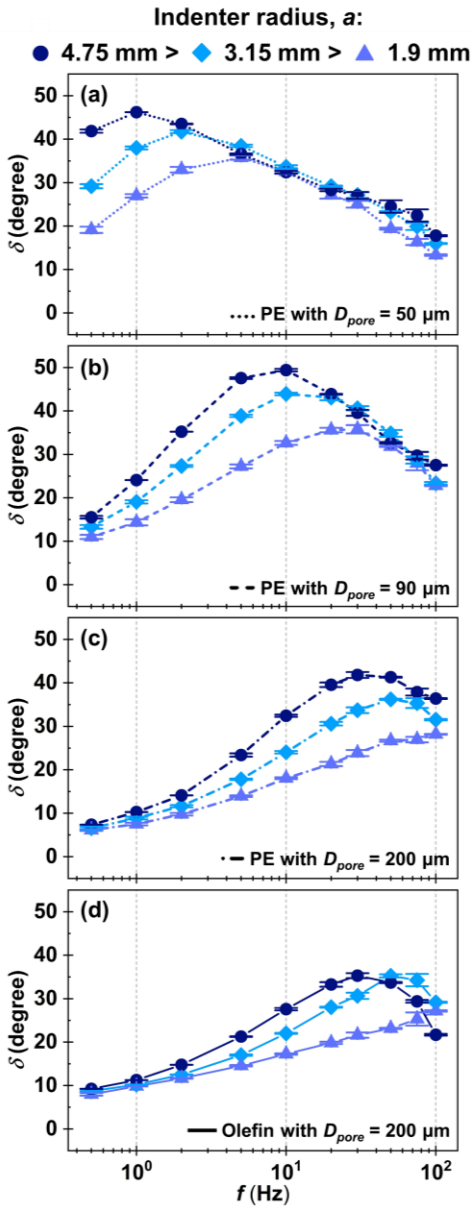

Figure 3-5: Phase lag δ versus frequency f curves measured with different combinations of contact radii a, pore sizes D_{pore}, and materials. The damping capacity curves were obtained with single-indenter-foam configurations. Each subfigure shows the effect of a on δ. The comparison of (a), (b), and (c) shows the effect of D_{pore} on δ. The comparison between (c) and (d) presents the effect of a material on δ.

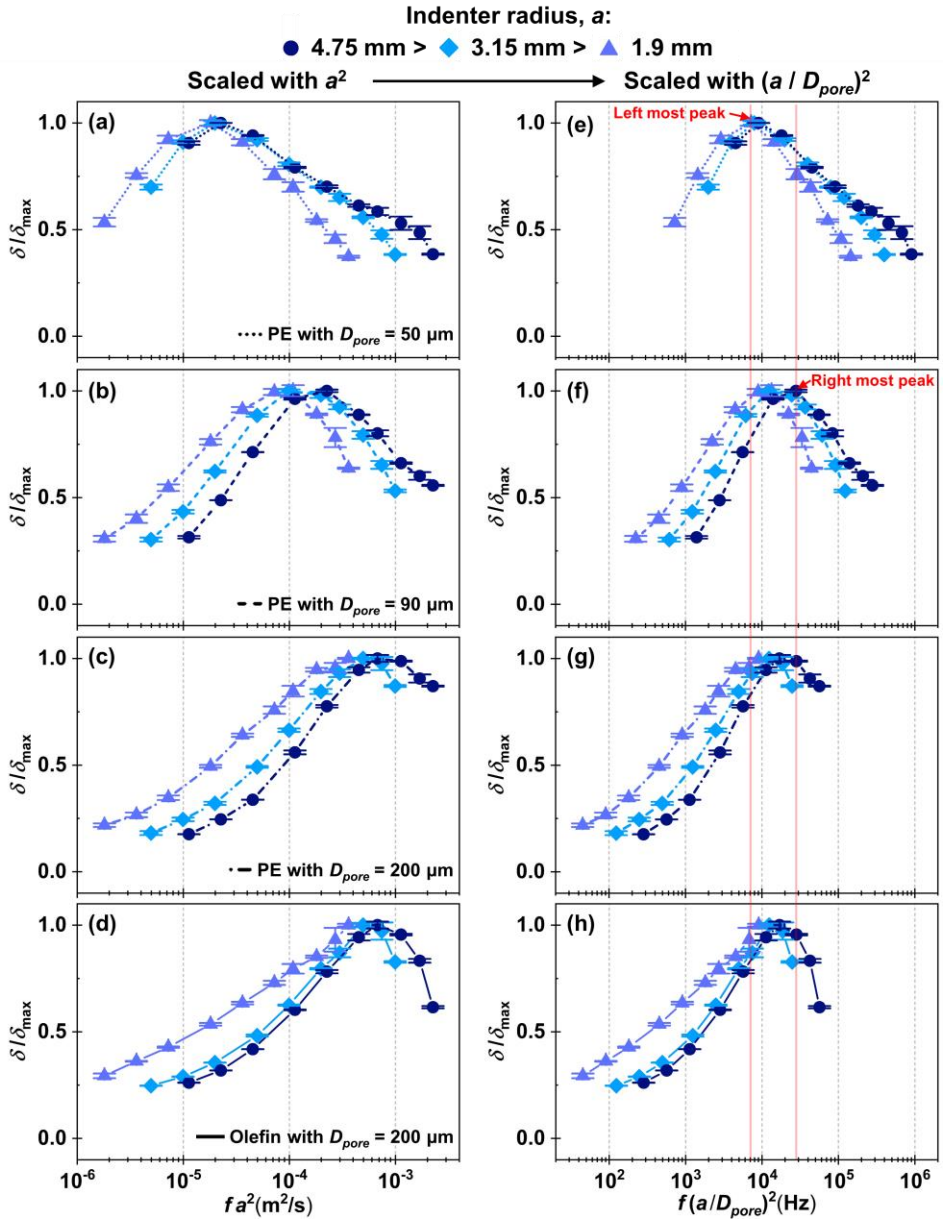

Figure 3-6: Effects of contact radius a and pore diameter D_{pore} on phase lag δ versus frequency f curves. In (a-d), scaling f with a^2 shifts the f_{peak} of three curves for each material (Figure 3-5) into a nearly single value. In (e-d), scaling fa^2 with $1/D_{pore}^2$ further aligned the f_{peak} of all the curves with each other centering around $f\,(a/D_{pore})^2 \cong 2\times10^4$ Hz. The red lines

indicate the left and right most f_{peak} among all of the curves, and therefore stacking the curves generates a nearly single master damping curve.

3.3.2. Two-indenter-foam Configuration for Rate-independent Damping Capacity

An optimal two-indenter-foam configuration for rate-independent damping capacity was obtained based on the experimental results of the single-indenter-foam configurations. After confirming that peak damping frequencies of 12 single-indenter-foam dampers were consistent with the scaling law (Eq. 3-7), an optimal two-indenter-foam configuration was determined by finding a combined response (Eqs. 3-10 and 3-11) among 66 combinations of two-indenter-foam configurations (two out of 12 single-indenter-foam configurations), which satisfied the search criterion. The search criterion was implemented via discrete optimization and was as follows:

$$\text{maximize } \|\delta_c\|_\infty$$

$$\text{subject to}$$

$$\max \delta_c - \min \delta_c < 5^\circ$$

$$\text{where}$$

$$5\text{Hz} < f < 100\text{Hz}$$

The phase lag of an optimal two-indenter-foam configuration attains values between the phase lags of each participant indenter-foam pair because total force cannot lag more or less than force carried by either indenter. Consequently, the search criterion confirmed that the combination of $\frac{\boldsymbol{D_{pore}}}{\boldsymbol{a}} = \frac{\mathbf{50\mu m}}{\mathbf{4.75mm}}$ and $\frac{\boldsymbol{D_{pore}}}{\boldsymbol{a}} = \frac{\mathbf{200\mu m}}{\mathbf{3.15mm}}$ could achieve nearly rate-independent damping capacity in a frequency range of 0.5 - 100 Hz.

An optimal two-indenter-form damper provided nearly rate-independent damping capacity and was consistent with the predicted trend (Figure 3-7). While the damping capacity of the single-

indenter-foam configurations, used for the optimal combined configuration, varied by around 26 degrees for D_{pore} = 50 μm with a = 4.75 mm and around 25 degrees for D_{pore} = 200 μm with a = 3.15 mm in a frequency range of 2 – 100 Hz, the damping capacity of the two-indenter-foam configuration only varied by around 7 degrees between 2 - 100 Hz (Figure 3-7b); although there was a sudden drop in the damping capacity of the two-indenter-foam configuration in a frequency range of 0.5 - 2 Hz, it was still minor compared to the fluctuations in the damping capacity of the single-indenter-foam configurations. Consequently, these results showed that an optimal two-indenter-foam configuration can generate relatively rate-independent damping capacity. In addition, the trend of the rate-independent damping capacity was aligned with the predicted trend (Eqs. 3-10 and 3-11 and Figure 3-7b). Also, the experimental and predicted results were consistent with our previous simulation work in the context that selecting and combining peak damping frequencies at the bounds of the bandwidth of interest provided desired rate-independent damping capacity [33]. Hence, PVE damping in 50 **μm** PE foam dominated the rate-independent damping capacity in the low-frequency range, whereas PVE damping in 200 **μm** PE foam took over in the high-frequency range.

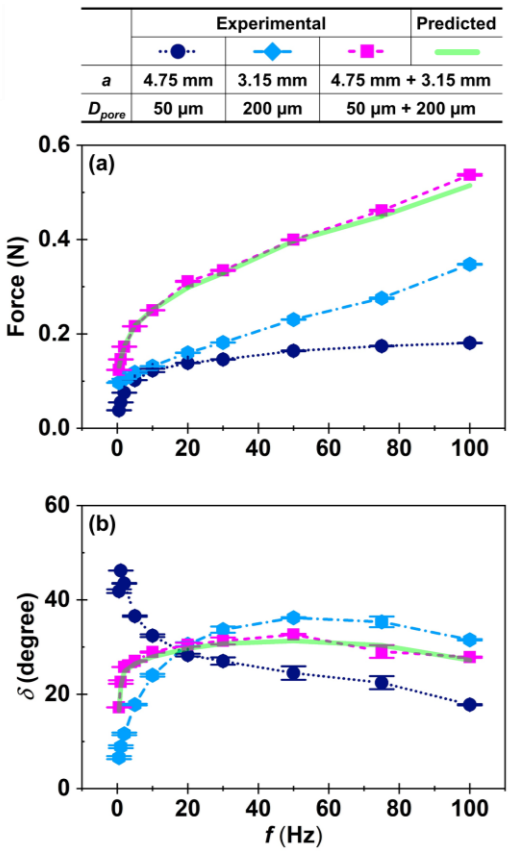

Figure 3-7: Force and phase lag δ as a function of frequency f measured with single- and two-indenter-foam configurations and predicted with Eqs. 3-10 and 3-11: (a) force versus frequency curves and (b) phase lag versus frequency curves. The optimal two-indenter-foam configuration offered relatively rate-independent damping capacity compared to the singe-indenter-foam configuration and was consistent with the predicted curves.

3.4. Discussions

This paper developed and tested passive PVE dampers inspired by cartilage damping mechanisms, allowing for the maximization of damping capacity at the desired frequency (single-indenter-foam damper) and rate-independent damping capacity (two-indenter-foam damper). Furthermore, the scaling analysis was used to examine the peak damping capacity of the single-indenter-foam system modeled by simple constitutive relations, and it was found that the peak damping capacity

was governed by the scaling law. Nevertheless, assumptions made in this scaling analysis and several practical challenges in the design of those dampers are worth revisiting.

In the scaling analysis, the foam was divided into two distinct regions. The region around the contact area was assumed to exhibit PE damping whereas the remainder was assumed to be linear elastic. This breakdown was employed to obtain a simple constitutive model for the indenter-foam damper. In reality, poroelastic diffusion gradually decreases as the stress gradient vanishes far from the contact region. Nevertheless, for cylindrical flat punches, the gradients are confined within spherical segments with radii twice as large as the contact radii [40], and therefore poroelastic effects can be safely assumed to occur in the vicinity of the contact region, within a volume that scales with the cube of contact radii. In addition, the average volumetric flux was assumed approximately equal to the liquid velocity diffusing out of that region (i.e., $q \approx v_l$). This approximation is acceptable for high porosity foams used in our experiments; the porosity of the samples ranged from 80 % to 85 %. Then, Darcy's law was used to relate flux to pressure gradient. In other words, viscous Darcian flow was assumed to dominate the liquid diffusion with negligible inertial effects (i.e., low Reynolds number $Re = \frac{\rho_l u D_{pore}}{\mu} \ll 1$). In the dynamic testing presented here, the linear velocity in the vicinity of the contact region attains a maximum value of $u = 2\ mm/s$ for 100 Hz cases. When the density and viscosity of olive oil and the maximum pore size are used in the experiments, the maximum Reynolds number is estimated to be around 0.002. Therefore, the Darcian flow assumption was reasonable. Lastly, the permeability and Young's modulus of the foams were assumed to be independent of applied strains. Strain-induced changes in these properties are prominent for large strains ($\varepsilon > 0.05$ [37]). In the dynamic testing, the deformation induced by the indenters reached 200 μm, and this corresponded compressive strain $\varepsilon \approx 0.07$ given the thicknesses of the foams in swollen condition. In fact, one of the factors leading

to slight shifts of the damping capacity curves with respect to the scaled frequency axis (Figure 3-6e-h) could be the strain-induced changes in the different types of foam.

Our past numerical simulation on the multi-indenter damper configurations [33] combined with the current experimental study on the two-indenter-foam configuration showed a great degree of flexibility in tuning the broadband performance of the dampers. Notwithstanding, several design requirements have to be met before the implementation of multi-indenter-foam dampers in practice. In particular, space limitations would necessitate analyses of interacting indenters as the principle of superposition would break down for closely placed indenters. For instance, in the asymptote where most of the indenters are placed closely in clusters, poroelastic dissipation would lose efficacy, and only viscoelastic dissipation would prevail. Such configurations would lack the maximum damping performance around a peak damping frequency as viscoelastic losses are length independent, and thus should be avoided. Lastly, practical utilization of liquid-imbibed PVE materials brings inherent challenges such as leakage, contamination, temperature-pressure-shear dependent viscosity, and phase changes. Therefore, the reliable encasement of the indenter-foam dampers is essential for maintaining the desired damping capacity.

3.5. Conclusions

A practical realization of cartilage-like damping capacity was demonstrated via the development of indenter-foam PVE dampers to extend damping methods in a low-frequency range (< 100 Hz). Our previous study on the numerical simulation of cartilage-like dampers [33] suggested that they have great potential to deliver effective damping capacity tailored to desired narrow and broadband dynamic responses. This current study designed, tested, and analyzed cartilage-inspired PVE dampers in a frequency range of 0.5 – 100 Hz, employing a hybrid of interfacial and material damping. The simple mechanical model and scaling analysis provided physical parameters that

govern a poroelastic peak damping frequency of a single-indenter-foam damper. The measured damping capacity of 12 single-indenter-foam dampers were consistent with the scaling analysis and demonstrated an ability to maximize poroelastic damping at the desired frequency across two decades by changing the pore diameter (diffusion) and contract radius (characteristic diffusion length). The poroelastic peak damping frequency can be tuned to specific modal frequencies of a structure so that damping is maximized only around them (narrowband performance). Viscoelastic damping was likely to provide baseline damping in a frequency range far from the poroelastic peak damping frequency. In addition, the optimized two-indenter-foam damper demonstrated that nearly rate-independent damping capacity can be achieved by combining single-indenter-foam dampers with poroelastic peak damping frequencies at the bounds of the bandwidth of interest (broadband performance). These findings on cartilage-inspired PVE dampers can appease the needs of both narrowband and broadband applications in a passive way.

3.6. Acknowledgment

This work is partially supported by the National Science Foundation Grant CMMI-1662456.

3.7. References

[1] U. Boz, I. Basdogan, IIR filtering based adaptive active vibration control methodology with online secondary path modeling using PZT actuators, Smart Mater. Struct. 24 (2015) 125001.

[2] F. Fenton, M.J. Sullivan, Cavity back iron with vibration dampening material in rear cavity, US5290036A, 1994.

[3] A.J. Keane, Passive vibration control via unusual geometries: the application of genetic algorithm optimization to structural design, J. Sound Vib. 185 (1995) 441–453.

[4] S. Behrens, A.J. Fleming, S.O.R. Moheimani, Passive vibration control via electromagnetic shunt damping, IEEEASME Trans. Mechatron. 10 (2005) 118–122.

[5] J.P. Carneal, M. Giovanardi, C.R. Fuller, D. Palumbo, Re-Active Passive devices for control of noise transmission through a panel, J. Sound Vib. 309 (2008) 495–506.

[6] C. Fuller, Passive distributed vibration absorbers for low frequency noise control, Noise Control Eng. J. 58 (2010).

[7] Y. Xue, J.S. Bolton, T. Herdtle, S. Lee, R.W. Gerdes, Structural damping by lightweight poro-elastic media, J. Sound Vib. 459 (2019) 114866.

[8] M.R.F. Kidner, C.R. Fuller, B. Gardner, Increase in transmission loss of single panels by addition of mass inclusions to a poro-elastic layer: Experimental investigation, J. Sound Vib. 294 (2006) 466–472.

[9] L. Zuo, S.A. Nayfeh, Optimization of the Individual Stiffness and Damping Parameters in Multiple-Tuned-Mass-Damper Systems, J. Vib. Acoust. 127 (2005) 77–83.

[10] L. Zuo, S.A. Nayfeh, The Two-Degree-of-Freedom Tuned-Mass Damper for Suppression of Single-Mode Vibration Under Random and Harmonic Excitation, J. Vib. Acoust. 128 (2006) 56–65.

[11] I.M. Koç, A. Carcaterra, Z. Xu, A. Akay, Energy sinks: Vibration absorption by an optimal set of undamped oscillators, J. Acoust. Soc. Am. 118 (2005) 3031–3042.

[12] A. Carcaterra, A. Akay, Theoretical foundations of apparent-damping phenomena and nearly irreversible energy exchange in linear conservative systems, J. Acoust. Soc. Am. 121 (2007) 1971–1982.

[13] A. Carcaterra, A. Akay, C. Bernardini, Trapping of vibration energy into a set of resonators: Theory and application to aerospace structures, Mech. Syst. Signal Process. 26 (2012) 1–14.

[14] R.L. Weaver, The effect of an undamped finite degree of freedom “fuzzy” substructure: Numerical solutions and theoretical discussion, J. Acoust. Soc. Am. 100 (1996) 3159–3164.

[15] E.E. Ungar, The status of engineering knowledge concerning the damping of built-up structures, J. Sound Vib. 26 (1973) 141–154.

[16] B.J. Lazan, Damping of Materials and Members in Structural Mechanics, Pergamon Press, 1966.

[17] K.Y. Sanliturk, D.J. Ewins, A.B. Stanbridge, Underplatform Dampers for Turbine Blades: Theoretical Modeling, Analysis, and Comparison With Experimental Data, J. Eng. Gas Turbines Power. 123 (2001) 919–929.

[18] P.R. Lakes, Viscoelastic Materials, 1 edition, Cambridge University Press, Cambridge ; New York, 2009.

[19] Z. Li, M.J. Crocker, A Review on Vibration Damping in Sandwich Composite Structures, Int. J. Acoust. Vib. 10 (2005).

[20] X.Q. Zhou, D.Y. Yu, X.Y. Shao, S.Q. Zhang, S. Wang, Research and applications of viscoelastic vibration damping materials: A review, Compos. Struct. 136 (2016) 460–480.

[21] M. Kumar, R.A. Shenoi, S.J. Cox, Experimental validation of modal strain energies based damage identification method for a composite sandwich beam, Compos. Sci. Technol. 69 (2009) 1635–1643.

[22] A.P. Mouritz, E. Gellert, P. Burchill, K. Challis, Review of advanced composite structures for naval ships and submarines, Compos. Struct. 53 (2001) 21–42.

[23] J. Park, D.L. Palumbo, Damping of Structural Vibration Using Lightweight Granular Materials, Exp. Mech. 49 (2009) 697–705.

[24] T. Pritz, Five-parameter fractional derivative model for polymeric damping materials, J. Sound Vib. 265 (2003) 935–952.

[25] R.L. Harne, On the linear elastic, isotropic modeling of poroelastic distributed vibration absorbers at low frequencies, J. Sound Vib. 332 (2013) 3646–3654.

[26] S.S. Deshmukh, G.H. McKinley, Adaptive energy-absorbing materials using field-responsive fluid-impregnated cellular solids, Smart Mater. Struct. 16 (2007) 106–113.

[27] G. Han, C. Hess, M. Eriten, C.R. Henak, Uncoupled poroelastic and intrinsic viscoelastic dissipation in cartilage, J. Mech. Behav. Biomed. Mater. 84 (2018) 28–34.

[28] P. Kannus, Structure of the tendon connective tissue, Scand. J. Med. Sci. Sports. 10 (2000) 312–320.

[29] V.C. Mow, A. Ratcliffe, A. Robin Poole, Cartilage and diarthrodial joints as paradigms for hierarchical materials and structures, Biomaterials. 13 (1992) 67–97.

[30] G. Han, M. Eriten, C.R. Henak, Rate-dependent crack nucleation in cartilage under microindentation, J. Mech. Behav. Biomed. Mater. 96 (2019) 186–192.

[31] B.K. Connizzo, A.J. Grodzinsky, Tendon exhibits complex poroelastic behavior at the nanoscale as revealed by high-frequency AFM-based rheology, J. Biomech. 54 (2017) 11–18.

[32] H.T. Nia, L. Han, Y. Li, C. Ortiz, A. Grodzinsky, Poroelasticity of Cartilage at the Nanoscale, Biophys. J. 101 (2011) 2304–2313.

[33] L. Liu, A.D. Usta, M. Eriten, A broadband damper design inspired by cartilage-like relaxation mechanisms, J. Sound Vib. 406 (2017) 1–14.

[34] U. Boz, M. Eriten, A numerical investigation of damping in fuzzy oscillators with poroelastic coating attached to a host structure, J. Sound Vib. 417 (2018) 277–293.

[35] H.T. Nia, I.S. Bozchalooi, Y. Li, L. Han, H.-H. Hung, E. Frank, K. Youcef-Toumi, C. Ortiz, A. Grodzinsky, High-Bandwidth AFM-Based Rheology Reveals that Cartilage is Most Sensitive to High Loading Rates at Early Stages of Impairment, Biophys. J. 104 (2013) 1529–1537.

[36] K.L. Johnson, Contact Mechanics, Cambridge University Press, 1987.

[37] L.J. Gibson, M.F. Ashby, Cellular Solids: Structure and Properties, Cambridge University Press, 1999.

[38] C. Peri, The extra-virgin olive oil chain, in: Extra-Virgin Olive Oil Handb., John Wiley & Sons, Ltd, 2014: pp. 3–10.

[39] Q. Lan, A.P.S. Selvadurai, Interacting indentors on a poroelastic half-space, Z. Für Angew. Math. Phys. ZAMP. 47 (1996) 695–716.

[40] A.C. Fischer-Cripps, Introduction to contact mechanics, 2nd ed, Springer, New York, 2007.

Chapter 4 Dynamic Mechanical Analyses Characterization of Indenter-foam Passive Dampers Under Harmonic Excitations*

Lejie Liu, Haocheng Yang, Corinne R. Henak, and Melih Eriten

*(*Prepared for submission to a journal)*

4.1. Introduction

Absorbing and trapping energy as often achieved by dampers in a prescribed frequency range is essential for vibration suppression in engineered systems. Dampers can be categorized as active, semi-active or passive depending on the existence of a feedback control in the system [1]. Active damping is used when high performance is critical and/or the host system operates under highly transient conditions. Active dampers are comprised of sensors, actuators and controllers and so increase complexity, weight, power consumption and cost to a particular system design than the one of passive dampers [2]. Passive dampers, in contrast, offer vibration suppression with simple utilization of a single or multiple damping mechanisms without a feedback control. Therefore, most passive dampers lack broadband effectiveness and adaptation to changing operation conditions. Examples of recent passive damper studies and corresponding damping mechanisms include: Yuan et al. used a novel mathematical method to study viscoelastically damped structures by generating a virtual fractional oscillator [3]; McNamara et al. introduced annular tuned liquid dampers that can be mounted in slender structures [4]; Wong W. and Wong C. simulated an air damper using Maxwell transformed element and Coulomb element [5]; Lv and Leamy introduced anechoic stubs as the damping element to remove vibration modes from planar frame structures [6]; Love et al. proposed a pendulum-type tuned mass damper to reduce wind-induced structural motion [7]; Javidialesaadi and Wierschem introduced a three-element inerter to suppress the

vibration of a single-degree-of-freedom system [8]; Tai et al. investigated an energy harvester using a monostable Duffing oscillator connected to an electromagnetic generator [9]. Current passive dampers focused on either narrow-band or broad-band loading frequencies and still lack of efficiency.

The authors tried to fill in the gaps and introduced a novel poro-viscoelastic (PVE) passive damper design: Liu et al. simulated a PVE indenter-foam damper using fractional Zener model and validated with experimental results [10]; Boz and Eriten introduced fuzzy oscillators with PVE coatings to reduce low frequency vibrations [11]; Han et al. designed and fabricated the PVE damper with two indenters and validated its damping capacity within 0-100 Hz frequency range [12]. The indenter-foam dampers developed by the authors were shown to be tunable for broadband [10] or narrowband [11] damping needs. Experimental validations reported by the same authors demonstrated that simple and cost-effective design of indenter-foam dampers delivers damping capacities comparable to other material dampers [12]. In those experiments, however, the authors utilized small excitations and thus investigated primarily linearized response of highly nonlinear PVE relaxation mechanisms and indenter-foam contact mechanics. Therefore, the performance of indenter-foam dampers under large vibrations and possible contact nonlinearities remains unexplored. This study aims at filling this gap.

4.2. Indenter-foam Dampers

Indenter-foam dampers consist of indenters transmitting vibration to PVE media and thus attenuate vibrations via viscoelasticity, diffusion and lossy fluid-solid interactions. In broader sense, PVE passive dampers employ various forms of contact and material damping mechanisms simultaneously and thus resemble articular cartilage at the tips of our long bones. In 2016, the

current authors optimized a set of indenter-foam dampers to achieve broadband damping [10]. In particular, we designed a damper where a PVE foam was sandwiched between two hard materials and vibrations were transmitted to that layer via multiple indenters of varying contact lengths. Near those indenter-foam contacts, length-dependent diffusion and PVE relaxations were triggered delivering maximum damping at frequencies coinciding to Peclet number of 1. Optimizing those contact lengths then enabled a rather constant loss factor for a broad frequency range (3-3000 Hz); i.e., an effective broadband damper. The authors then utilized the same dampers in fuzzy-oscillators and demonstrated tunable vibration absorption around modes of a host structure [11]. Finally, in a more recent article, the authors developed foam-indenter dampers and reported their damping capacity in single and double indenter configurations [12]. Tested dampers included rigid cylindrical indenters pressed on open-cell polyethylene foams swollen fully with Newtonian liquid. Dynamic mechanical analysis (DMA) with linear harmonic vibrations of the indenters over a frequency range of 0.5-100 Hz delivered damping capacity. The experimental observations validated both the narrow and broadband performance of those dampers under small vibrations.

In those earlier works, small vibration assumptions allowed us to model the indenter-foam system with linearized PVE models that neglect complications such as material and contact nonlinearities. The latter of those complications will be the focus of the current study as in practical indenter-foam damper assembly, contact interfaces are maintained by pre-compression and adhesion. Pre-compression levels can be adjusted to achieve a desired strain in the PVE foam. After a sufficiently long time, PVE relaxations lead to reduction in residual compressive stresses and thus subsequent vibrations can apply tension in parts of loading cycles with moderate to large amplitudes. If adhesion between PVE foam and indenters counters the tension, then contact areas remain constant and changes in stiffness and damping capacity are expected to be minimal.

However, adhesion of PVE materials to rigid surfaces is known to increase with the unloading rates [13–17]. This then proposes a scenario where certain combination of strains and strain rates could develop tensile stresses in PVE materials that would overcome adhesive strength and cause peeling at the indenter-foam interface. Peeling at the interface in turn would be reflected in stiffness and damping capacity estimations. Moreover, the asymmetric nature of contact response in compressive and tensile parts of a vibration cycle produces higher harmonics (starting with the second harmonic) in the transmitted contact force. Therefore, contact nonlinearities would influence dampers' performance directly. Those nonlinearities are experimentally studied in the current work. Amount of contact peeling, corresponding loss of contact stiffness and degree of nonlinearities are reported as maps of strains and strain rates. Those maps provide guidelines for linear and nonlinear designs of indenter-foam dampers.

4.3. Experiments and Methods

4.3.1. Indenter-foam Damper Preparation

Open cell polyurethane foams (New England Foam Co.) swollen with castor oil (NAISSANCE) were used as the PVE material of the dampers [12]. The average pore size of the foams was 0.25 mm in diameter (100 PPI) reported by the manufacturer. The foams were cut in cylindrical shapes with radius, a_s, of 27 mm and thickness, H, of 7.6 mm, and then placed in a sample holder filled with castor oil. The foam density was measured as 0.03 $\mathrm{g/cm^3}$ (consistent with manufacturer specifications). The dynamic viscosity of castor oil is reported as 0.6 $Pa \cdot s$ [18]. Swelling of the dry foam samples included several steps as reported elsewhere [19,20]. Prior to swelling, the bottom of the cylindrical foam was fixed to the sample holder; sample was then loaded to 70% average normal strain in nearly unconfined compression setting. Castor oil was added to the sample

holder and the sample stayed in the castor oil bath in pre-compressed and fully submerged condition for 10 minutes. Finally, the sample was unloaded slowly and left to recover for 10 minutes. The sample remained fully submerged during the last recovery phase. To achieve homogenous and near full-saturation, load-submerge-unload-recovery process was repeated 6 times. Repetitions assisted removal of air bubbles trapped in the sample and ensured homogeneity of the foams in the swollen states.

As for indenters, two cylindrical punches were made from aluminum, with radii, a, of 4.25 mm and 8.5 mm to re-confirm the earlier observations on length-dependent PVE relaxations and their influence on contact nonlinearities and damping capacity of the dampers [12,17].

4.3.2. Dynamic Mechanical Analysis Setup

In our previous work, we investigated the damping capacity of various indenter-foam dampers via DMA [12]. We used a similar methodology in this study, with broader ranges of strains and strain rates. Previous studies had utilized strains of 0.01 and average strain rates of 0.04/s to 4/s. Here, we extended that range 3-fold larger to gauge nonlinear dynamic response of the dampers. In our dynamic tests (Figure 4-1a), an indenter probe driven by a universal tester (TA ElectroForce MODEL3230; TA Instruments, Eden Prairie, MN) was used to apply first a quasistatic pre-compression and then harmonic vibrations with prescribed amplitudes and frequencies on the top surface of the swollen foams. A load cell attached to the bottom of the sample holder monitored the forces throughout the experiments. The expected form of mathematical functions of input displacements and measured forces were shown on a sketch of the setup in Figure 4-1b. A quasistatic displacement of $d_0 = 1$ mm was applied on the swollen foams and was held for 10 minutes for full relaxation to ensure full contact at the beginning of each test. Harmonic vibration amplitude, Δd was set to 20, 50, 100, and 200 μm. Therefore, the strain level remained small to

avoid any material and geometric nonlinearities. The frequency of the harmonic vibrations f was set to 1, 3, 10, 20, 50, 70 and 100 Hz. This frequency range is considered as broadband for civil and engineering structures. Thus, we extend the strain and strain rate level of the harmonic excitation to 0.025 and 10/s, respectively. Besides, the peak relaxation frequencies of the 8.5 mm and 4.25 mm indenters were found at around 7.5 Hz and 30 Hz, thus 1-100 Hz range is sufficient for our study. Each measurement reached steady-state after 60 cycles, and the last five cycles of displacement and corresponding force data were reported in the results. The sampling rate was chosen at 5000 Hz to give enough data points for the 100 Hz harmonic case. The displacement controller of the TA instrument tended to oscillate under smaller amplitudes than the one given as the input when loading frequencies were larger than 20 Hz. A larger modified displacement amplitude had to be provided to obtain the desired input displacement. The phase lag between applied displacements and measured forces, δ, is used to quantify the damping capacity of the indenter-foam dampers whereas deviations from the expected monofrequency (linear) response in force were reported as a measure of nonlinearity.

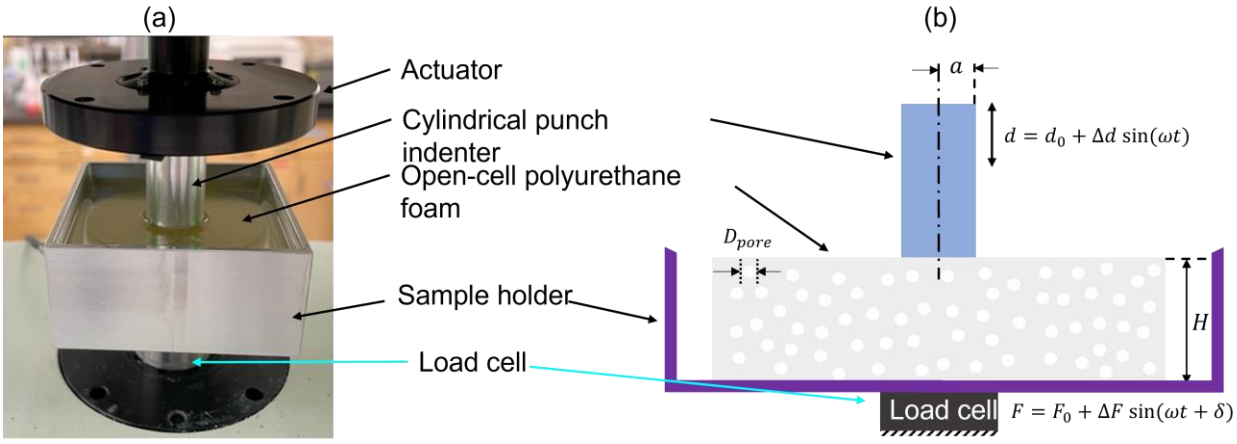

Figure 4-1: Experimental setup for dynamic testing of the indenter-foam dampers, (a) photo and (b) sketch.

4.4. Results and Discussion

4.4.1. Dynamic Test Results

Figure 4-2a shows typical steady-state forces measured from 8.5 mm radius indenter-foam damper under harmonic excitations at two extreme cases; almost linear case at $f = 1$ Hz and $\Delta d = 20$ μm, and the most nonlinear case observed at $f = 100$ Hz and $\Delta d = 200$ μm. Excitations in the form of indenter displacements were nearly harmonic for both cases; i.e., negligibly small higher harmonics existed in the signals (blue curves in Figure 4-2a). Forces recorded for the former case also resembled pure harmonic signals with amplitudes in the compressive regime (+ magnitudes) throughout a loading cycle, suggesting linear compressive response of the foams. The linearity was also evident from the symmetric force-displacement curve (hysteresis loop) in Figure 4-2b and fundamental harmonic-dominated Fourier transform (normalized with respect to the fundamental harmonic peak value) in Figure 4-2c. For the latter case, forces exhibited partially tensile and partially compressive regime within a loading cycle and clear asymmetries in the form of softening in the tension direction (Figure 4-2a). The corresponding hysteresis loop (Figure 4-2b) showed the asymmetry clearly and Fourier transform of the force (Figure 4-2d) contained higher harmonics at $f_{2,3} = 200, 300$ Hz. Note that the amplitude of 2nd harmonic was an order of magnitude larger than the 3rd harmonic. 2nd harmonics were previously shown to dominate the nonlinearities in various other systems with contacts. For instance, partial peeling across rough crack surfaces was the source of contact acoustic nonlinearities in surface wave propagation and corresponding acoustic nonlinearity parameter (defined as the ratio of 2nd to fundamental harmonic amplitudes) yielded a measure of nonlinearity [21]. Besides, contact stiffness in shear direction decreases linearly with increasing frictional slip [22–24], and thus delivers quadratic nonlinearity in restoring forces. Borrowing from this literature, we studied next the ratio of amplitudes of 2nd

and fundamental harmonics (referred to as harmonic ratio in the remainder of the paper) as a function of applied displacement amplitudes and rates.

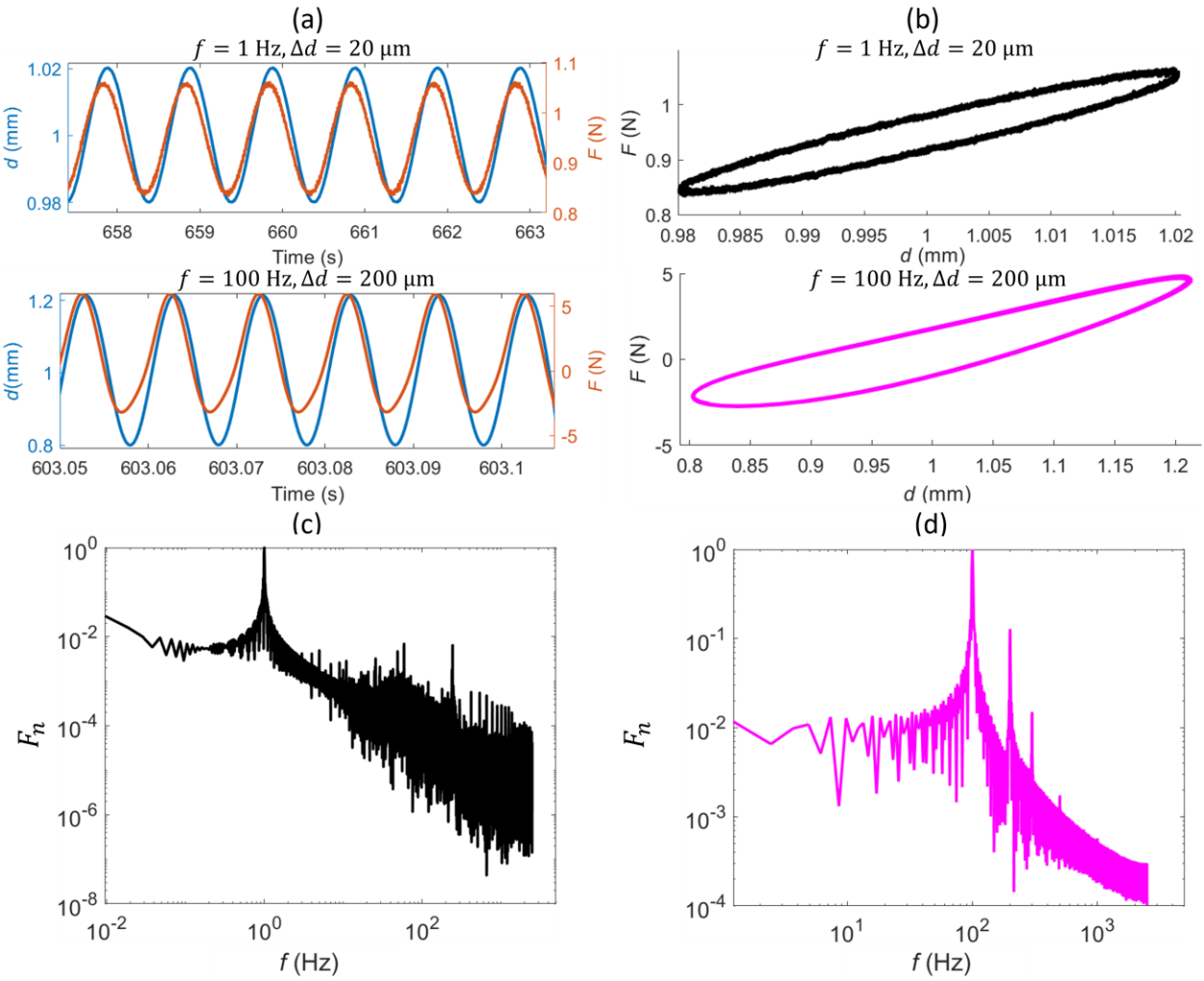

Figure 4-2: (a) Displacements and forces recorded for 8.5 mm radius indenter-foam damper at: f=1 Hz, Δd=20 µm (upper subfigure) and f=100 Hz, Δd=200 µm (lower subfigure); (b) corresponding hysteresis loops, and (c) normalized FFT of the force at f=1 Hz, Δd=20 µm (d) normalized FFT of the force at f=100 Hz, Δd=200 µm.

4.4.2. Harmonic Ratio

To show how nonlinearity in measured forces depended on applied displacement amplitudes and rates, we plotted in Figure 4-3 the harmonic ratio as a function of applied average strains and strain rates for 8.5 mm (a) and 4.25 mm (b) radius indenter-foam dampers. There were 28 data points in total, with 4 different oscillation amplitudes by 7 different loading rates. Linear interpolation was applied to obtain the smooth contour plots. The average applied strain was defined as the indenter displacement divided by the undeformed thickness of the swollen foam, $\Delta d/H$, whereas average strain rate was defined as the displacement loading rate divided by the thickness of the foam, $\dot{d}/H$.

Contour plots for both indenters show a similar trend of harmonic ratio along with the average strain and strain rate. At low strain rates, ($\frac{\dot{d}}{H} \ll 1$), the harmonic ratio increased with strains and was independent of strain rate. The latter trend is expected since damping forces at low strain rates would have negligible contribution compared to elastic forces in the foams and thus would not cause any substantial nonlinearity. The former trend is more difficult to explain. Since strains used in this study were limited to 2.5%, within typical proportional limit of various open cell foams [25], neither geometric (higher order strains) nor material nonlinearities could explain the increase in harmonic ratio with strains. An alternative explanation is peeling induced by increasing strains. In this small strain and strain rate regime, the elastic forces grow as strains increase. Increasing elastic forces could overcome adhesive forces holding the indenter and foam samples together and compromise full contact condition by partial peeling. Given the stress concentrations, such a peeling should commence at the edge of the flat indenter punches. At higher strain rates ($\frac{\dot{d}}{H} \gg 1$), the harmonic ratio increased with both increased of average strain and strain rate. If peeling was responsible after the nonlinearity, this trend is also expected since both damping and elastic forces

contribute to the total forces built up in the foams, which then could overcome adhesive interactions between indenter and foams.

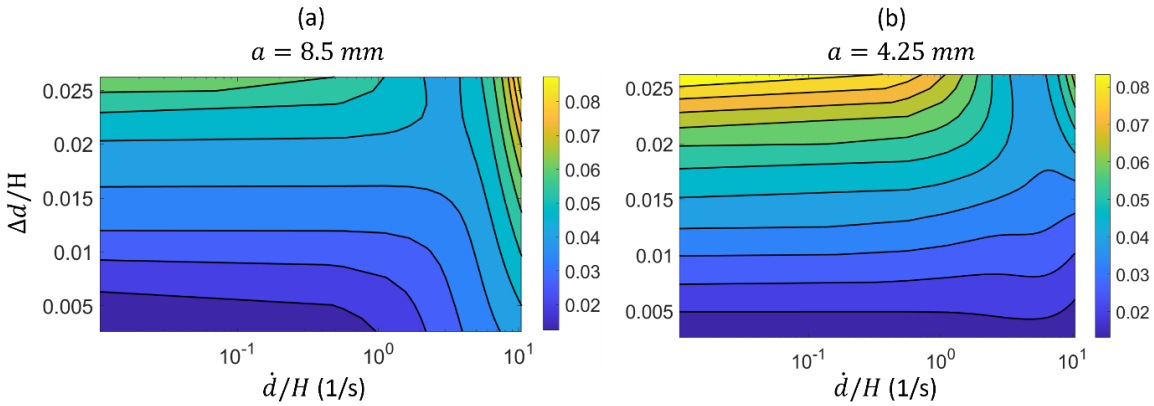

Figure 4-3: Contour plots of harmonic ratio as a function of both average strain and average strain rate for (a) the 8.5mm radius indenter-foam damper, and (b) the 4.25mm radius indenter-foam damper.

At high strains $\left(\frac{\Delta d}{H} \sim 0.025\right)$ and intermediate strain rates $\left(1 < \frac{\dot{d}}{H} < 3\right)$, harmonic ratio attained smaller values compared to smaller and higher strain rates. This trend could not be explained only by elastic and damping forces built up in the foams because at a given strain level increasing strain rates should increase the force built up and thus peeling and corresponding nonlinearity in the damper response. We will resort to rate-dependent adhesion commonly observed for multiphasic soft materials such as the foams used in this study to further analyze that trend.

4.4.3. Rate-dependent Adhesion and Peeling Index

In previous [12] and current indenter-foam dampers, adhesion was the only force that kept the interface between the indenter and foams in contact during possible tension in a vibration cycle. As we discussed in an earlier work [17], adhesion of PVE materials depends on the degree of

relaxation, and hence it is rate-dependent. This is practically because of how applied mechanical work is distributed within PVE medium to strain, dissipation, bond breakage and surface creation energies during the peeling process [26–28]. In that respect, experimentally recorded adhesion can only be treated as apparent property that is coupled to mechanical response of the material rather than an intrinsic adhesive energy of surfaces newly created after peeling. This coupled response can be simply modeled by a slider element attached to a lossy material (standard linear solid) model as shown in Figure 4-4. In this model, two springs and a dashpot represent the foam with one dominant relaxation time constant and the slider represent the interface between the indenter and the foam. Note that similar models were used to explain nonlinearities in modal damping [29] and in wave transmission [30] due to interfacial slip. When a harmonic input displacement d is applied to the foam a resultant periodic force F is transmitted to the slider element; i.e., contact interface. The rate-dependent adhesion force, quantified herein with pull-off forces measured in tack experiments, is denoted as F_p. Accordingly, full separation will occur when the total force in the material exceeds adhesive forces; i.e., $F > F_p$. When $F < F_p$, the interface behavior will range from full to partial contact depending on the magnitude of F relative to F_p. Adopting an ad-hoc approach, we define a peeling index: $PI = F/F_p$. In this definition, $PI = 1$ means the interface is fully separated and $PI = 0$ means the interface is under complete contact condition. Note that we already measured the forces built up in the foams, F during the dynamic tests discussed above. To quantify the peeling index, we need pull-off forces under different unloading rates.

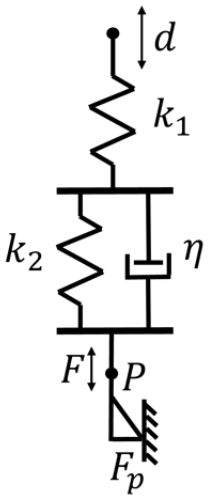

Figure 4-4: Simple model of indenter-foam damper with an adhesive interface (modeled as the slider element).

We conducted adhesion experiments were on the same machine and setup shown in Figure 4-1. In those experiments, a static 1 mm displacement with 0.1/s average strain rate was applied on the foams and was held for 10 minutes for full relaxation. Then, the indenter was pulled off at different average unloading strain rates ranging from 0.01 s^{-1} to 10 s^{-1}; i.e., the same range used in the dynamic testing. Forces were recorded at same sampling rates as in dynamic tests. Each test was repeated twice and the maximum error within 4%, which showed a good repeatability. Figure 4-5 shows typical force-displacement responses obtained from those experiments (positive forces are compressive and negative are tensile per the convention used in the dynamic tests). The pull-off force was defined as the maximum negative force measured.

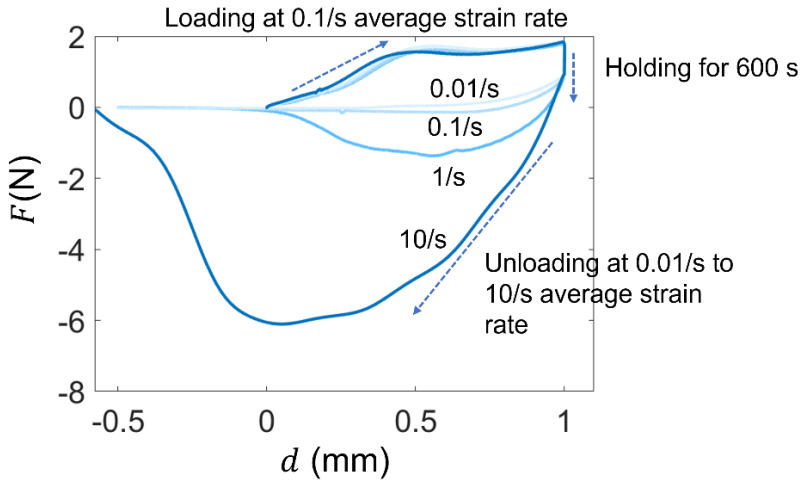

Figure 4-5: Raw data of pull-off test for 8.5 mm radius indenter-foam damper under pull-off average strain rates at 0.01/s, 0.1/s, 1/s, and 10/s.

Measured pull-off forces normalized to contact areas of indenters (average pull-off stresses) are shown in Figure 4-6. Average pull-off stresses increased with unloading rates for both indenters. Similar increases in adhesion with unloading rates were reported for viscoelastic (elastomers in [31]) and PVE materials (cartilage in [16]).

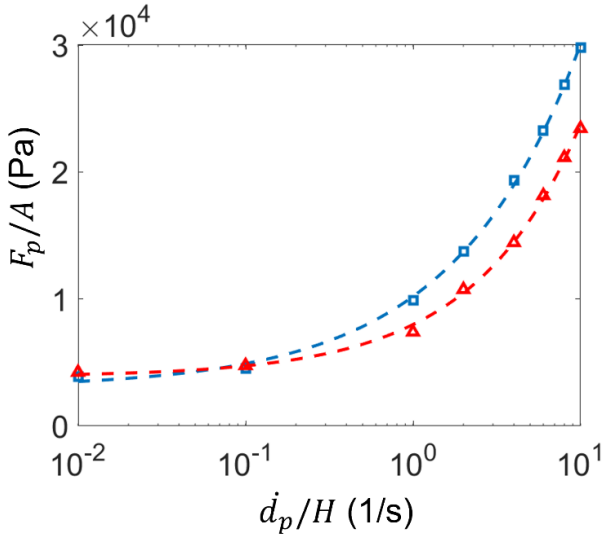

Figure 4-6: The average pull-off stress as a function of the average pull-off strain rate for 8.5 mm radius (blue) and 4.25 mm radius (red) indenter-foam dampers.

After the adhesion tests, the peeling index was estimated as the ratio of dynamic and pull-off forces measured at corresponding strain rates. The contours of *PI* values are shown as a function of strain and strain rates in Figure 4-7. One should notice clearly the similarities between the *PI* and the harmonic ratio contours in Figure 4-7 and Figure 4-3, respectively. Therefore, we conclude that the degree of nonlinearity observed in forces measured was directly linked to the value of *PI*; i.e., the degree of peeling in indenter-foam interface.

The trends in *PI* can be qualitatively explained by the simple model in Figure 4-4 and rate-dependent adhesion shown in Figure 4-6. At low strain rates, adhesion force F_p remains nearly constant (changes only 2-fold for 0.01-1 s^{-1} strain rates) while only springs in Figure 4-4 contribute to the forces built up in the foam. Hence, the degree of peeling is only a function of strains. This is reflected as horizontal contours of *PI* in strain rate-strain mapping in Figure 4-7. At intermediate to high strain rates, both springs and damper contribute to the forces in the foam but adhesion force increases steeply to suppress peeling partially. That is why the horizontal contours are interrupted and *PI* attains a local minimum at a given strain. As strain rates further increase, increase in adhesion forces cannot compensate for the increase in forces in the foam, and so diagonal contours of *PI* are observed in strain rate-strain mapping. At extremely high loading rates, one would expect damper forces not to contribute to the forces in the foam. In other words, the loading would be too quick for the foam to relax significantly within a loading cycle. In that asymptotic case, we expect the *PI* contours to exhibit horizontal patterns as in low frequency (nearly quasistatic) asymptote shown in Figure 4-7. One key difference in those asymptotes would be that unrelaxed foam is stiffer and thus higher *PI* values would be achieved at higher strain rates. Note that extremely high

loading rates can be achieved at loading frequencies that are much larger than peak relaxation frequencies of the foam. Our experiments do not cover that asymptote because of the limited bandwidth of the employed universal testing machine.

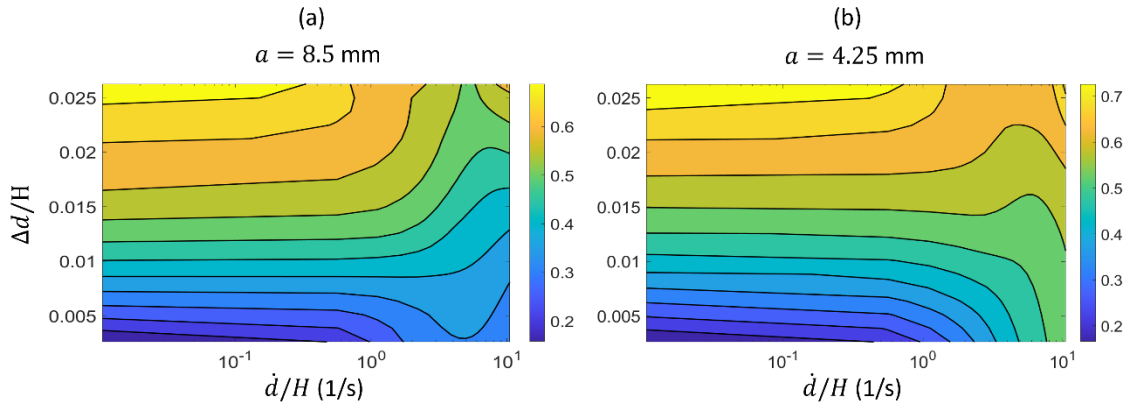

Figure 4-7: Contour plots of peeling index as a function of average strain and average strain rate normalized with peak damping frequencies for (a) 8.5 mm radius indenter-foam damper and (b) 4.25 mm radius indenter-foam damper.

4.4.4. Nonlinearity, Peeling and Reduction in Contact Stiffness

Above discussion relates nonlinear dynamic response of indenter-foam dampers to the partial peeling at the interface. A similar connection is expected with reduction in contact stiffness, which scales with the product of Young's modulus and contact length (radius) [32]. Contact stiffness, K_{con} can be estimated from the force-displacement curves (Figure 4-5). To account for the rate-dependent modulus of the foam and its effect on stiffness, we normalized K_{con} by its initial value at the start of tension K_{con}^0 so that $K_n = K_{con}/K_{con}^0$ ranges from 0 to 1 and quantifies the change in contact lengths throughout adhesion tests. Note that similar normalized stiffness measures were used to identify onset of sliding and plastic shearing in the literature [33–35]. Figure 4-8 shows the normalized stiffness for both large and small indenters. As pull-off strain increased, normalized

stiffness decreased because of partial peeling and reduction in contact lengths. For all strain rates except for the highest and both indenters, normalized stiffness collapsed nearly on to a single curve that smoothly reduces from 1 to ~0.2 as a function of strain. That reduction is less for the highest loading rate. This deviation can be attributed to the complicated peeling dynamics at high adhesion levels measured for 10 s^{-1} cases. As shown in Figure 4-5, even after pull-off forces were reached, the peeling process continued all the way to negative (tensile) displacements. So, more straining was needed to fully separate indenters from the foams at the highest strain rate thanks to increased adhesion.

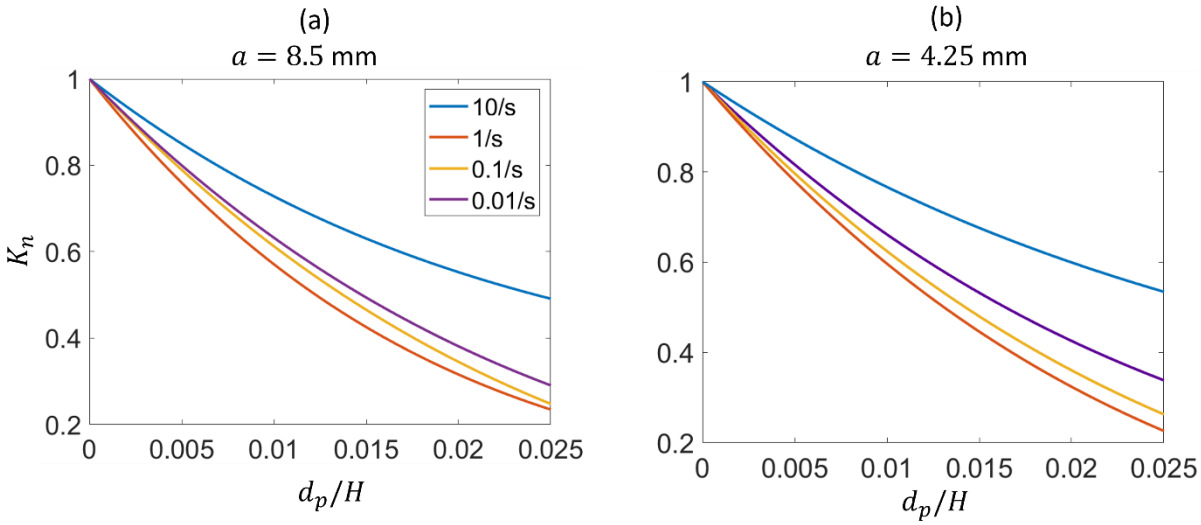

Figure 4-8: The normalized stiffness as a function of average strain of (a) 8.5mm radius indenter-foam damper and (b) 4.25 radius indenter-foam damper.

Finally, reduction in normalized stiffness can be linked to the peeling index since both are defined as proportional to contact length. Experimentally evaluated *PI* and reduction in normalized stiffness $(1 - K_n)$ are plotted in Figure 4-9 at coinciding strains for both indenters. As expected, *PI* and $(1 - K_n)$ are linearly related for all but highest strain rate cases. Complicated transients in

the peeling process, as discussed above, potentially lead to breakdown of that linearity at the highest strain rate. Nevertheless, the reduction in contact stiffness, $(1 - K_n)$, the decrease in contact lengths and degree of peeling can be alternatively used to predict the degree of nonlinearity in dynamic response of the indenter-foam dampers. To do that, one needs rate-dependent adhesion response of the indenter-foam interface.

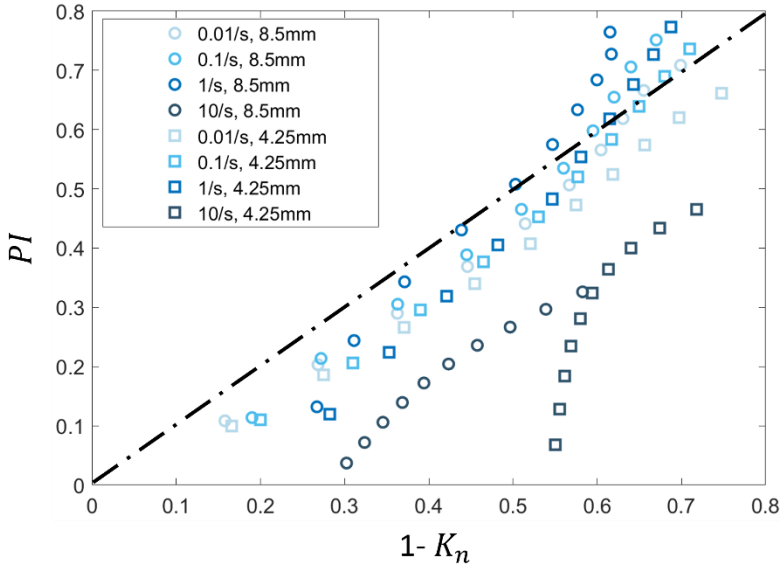

Figure 4-9: Scatter plot of PI versus $(1 - K_n)$ for both 8.5 mm and 4.25 mm radius indenter-foam damper under average strain rate at 0.01/s, 0.1/s, 1/s, and 10/s.

4.5. Conclusions

In this study, we measured the nonlinear dynamic response of indenter-foam dampers and explained the source of nonlinearity. First, we noticed higher harmonics in force measurements on an indenter-foam damper that was harmonically excited under small strains, which was the signature of a nonlinear response. Then, we analyzed relative magnitudes of second harmonics at various strains and strain rates to obtain nonlinearity maps. Since geometric and constitutive nonlinearities were unlikely due to small strains used in the experiments, we focused on interfacial

nonlinearities, specifically adhesion and peeling dynamics, to explain the source of nonlinearities. We used a simple viscoelastic material model attached to a slider element to model adhesive interactions, and defined peeling index and reduction in contact stiffness that directly correlated with the degree of nonlinear dynamic response. In summary, any of the reduction in contact stiffness, the decrease in contact lengths and degree of peeling could predict the degree of nonlinearity in dynamic response of the indenter-foam dampers. Nonlinear dynamic response could complicate the design and limit usability of indenter-foam dampers. Our findings suggest increasing adhesion at the indenter-foam interface would suppress those nonlinearities trivially (e.g., via chemical and physic reinforcement of interfaces).

Interfacial nonlinearities studied here induced second harmonics due to asymmetric nature of peeling dynamics. Nearly perfect correlation of relative second harmonic amplitudes and peeling index paves the way to wave or vibration-based diagnostic of the adhesive integrity of multi-phasic interfaces. Since those interfaces are ubiquitous in nature and engineering systems with soft materials, such a diagnosis method could prove utility in various applications.

4.6. Acknowledgment

This work is partially supported by the National Science Foundation (Grant No. CMMI-1662456 and 1826214) and by the University of Wisconsin-Madison, Office of the Vice Chancellor for Research and Graduate Education with funding from the Wisconsin Alumni Research Foundation.

4.7. References

[1] T.T. Soong, B.F. Spencer Jr, Supplemental energy dissipation: state-of-the-art and state-of-the-practice, Eng. Struct. 24 (2002) 243–259.

[2] A. Preumont, Vibration control of active structures: an introduction, Springer, 2018.

[3] J. Yuan, S. Gao, G. Xiu, L. Wang, Mechanical Energy and Equivalent Viscous Damping for Fractional Zener Oscillator, J. Vib. Acoust. 142 (2020).

[4] K.P. McNamara, J.S. Love, M.J. Tait, T.C. Haskett, Response of an Annular Tuned Liquid Damper Equipped With Damping Screens, J. Vib. Acoust. 143 (2020).

[5] W.O. Wong, C.N. Wong, Optimal Design of Maxwell-Viscous Coulomb Air Damper With a Modified Fixed Point Theory, J. Vib. Acoust. 143 (2020).

[6] H. Lv, M.J. Leamy, Damping Frame Vibrations Using Anechoic Stubs: Analysis Using an Exact Wave-Based Approach, J. Vib. Acoust. 143 (2021).

[7] J.S. Love, K.P. McNamara, M.J. Tait, T.C. Haskett, Series-Type Pendulum Tuned Mass Damper-Tuned Sloshing Damper, J. Vib. Acoust. 142 (2019).

[8] A. Javidialesaadi, N.E. Wierschem, Three-Element Vibration Absorber–Inerter for Passive Control of Single-Degree-of-Freedom Structures, J. Vib. Acoust. 140 (2018).

[9] W.-C. Tai, M. Liu, Y. Yuan, L. Zuo, On Improvement of the Frequency Bandwidth of Nonlinear Vibration Energy Harvesters Using a Mechanical Motion Rectifier, J. Vib. Acoust. 140 (2018).

[10] L. Liu, A.D. Usta, M. Eriten, A broadband damper design inspired by cartilage-like relaxation mechanisms, J. Sound Vib. 406 (2017) 1–14.

[11] U. Boz, M. Eriten, A numerical investigation of damping in fuzzy oscillators with poroelastic coating attached to a host structure, J. Sound Vib. 417 (2018) 277–293.

[12] G. Han, U. Boz, L. Liu, C.R. Henak, M. Eriten, Indenter–Foam Dampers Inspired by Cartilage: Dynamic Mechanical Analyses and Design, J. Vib. Acoust. 142 (2020) 051113.

[13] A.N. Gent, J. Schultz, Effect of Wetting Liquids on the Strength of Adhesion of Viscoelastic Material, J. Adhes. 3 (1972) 281–294.

[14] D. Maugis, M. Barquins, Fracture Mechanics and Adherence of Viscoelastic Solids, in: L.-H. Lee (Ed.), Adhes. Adsorpt. Polym., Springer US, Boston, MA, 1980: pp. 203–277.

[15] B. Lorenz, B.A. Krick, N. Mulakaluri, M. Smolyakova, S. Dieluweit, W.G. Sawyer, B.N.J. Persson, Adhesion: role of bulk viscoelasticity and surface roughness, J. Phys. Condens. Matter. 25 (2013) 225004.

[16] G. Han, M. Eriten, Effect of relaxation-dependent adhesion on pre-sliding response of cartilage, R. Soc. Open Sci. no. 5 (2018): 172051.

[17] G. Han, M. Eriten, and C. R. Henak, Rate-dependent adhesion of cartilage and its relation to relaxation mechanisms, J. Mec. Behav. bio. mater. 102 (2020): 103493

[18] L. A. Quinchia, M. A. Delgado, C. Valencia, J. M. Franco, and C. Gallegos, Viscosity modification of different vegetable oils with EVA copolymer for lubricant applications, Indu.Crops and Pro. 32, no. 3 (2010): 607-612.

[19] H.T. Nia, I.S. Bozchalooi, Y. Li, L. Han, H.-H. Hung, E. Frank, K. Youcef-Toumi, C. Ortiz, A. Grodzinsky, High-Bandwidth AFM-Based Rheology Reveals that Cartilage is Most Sensitive to High Loading Rates at Early Stages of Impairment, Biophys. J. 104 (2013) 1529–1537.

[20] H.T. Nia, L. Han, Y. Li, C. Ortiz, A. Grodzinsky, Poroelasticity of cartilage at the nanoscale, Biophys. J. 101 (2011) 2304–2313.

[21] T. Oberhardt, J.-Y. Kim, J. Qu, L.J. Jacobs, A contact mechanics based model for partially-closed randomly distributed surface microcracks and their effect on acoustic nonlinearity in Rayleigh surface waves, AIP Conf. Proc. 1706 (2016) 020024.

[22] M. Eriten, A.A. Polycarpou, L.A. Bergman, Physics-based modeling for fretting behavior of nominally flat rough surfaces, Int. J. Solids Struct. 48 (2011) 1436–1450.

[23] M. Eriten, S. Chen, A.D. Usta, K. Yerrapragada, In Situ Investigation of Load-Dependent Nonlinearities in Tangential Stiffness and Damping of Spherical Contacts, J. Tribol. 143 (2020).

[24] K.S. Parel, R.J. Paynter, D. Nowell, Linear relationship of normal and tangential contact stiffness with load, Proc. R. Soc. Math. Phys. Eng. Sci. 476 (2020) 20200329.

[25] L.J. Gibson, M.F. Ashby, B.A. Harley, Cellular Materials in Nature and Medicine, Cambridge University Press, 2010.

[26] T. Yang, X. Yang, R. Huang, K.M. Liechti, Rate-dependent traction-separation relations for a silicon/epoxy interface informed by experiments and bond rupture kinetics, J. Mech. Phys. Solids. 131 (2019) 1–19.

[27] L. Léger, C. Creton, Adhesion mechanisms at soft polymer interfaces, Philos. Trans. R. Soc. Math. Phys. Eng. Sci. 366 (2008) 1425–1442.

[28] E. Barthel, C. Frétigny, Adhesive contact of elastomers: effective adhesion energy and creep function, J. Phys. Appl. Phys. 42 (2009) 195302.

[29] D.J. Segalman, M.S. Allen, M. Eriten, K. Hoppman, Experimental Assessment of Joint-Like Modal Models for Structures, in: American Society of Mechanical Engineers Digital Collection, 2016.

[30] K.J. Moore, M. Kurt, M. Eriten, J.C. Dodson, J.R. Foley, J.C. Wolfson, D.M. McFarland, L.A. Bergman, A.F. Vakakis, Nonlinear Parameter Identification of a Mechanical Interface Based on Primary Wave Scattering, Exp. Mech. 57 (2017) 1495–1508.

[31] G. Violano, L. Afferrante, Adhesion of compliant spheres: an experimental investigation, Procedia Struct. Integr. 24 (2019) 251–258.

[32] K.L. Johnson, Contact mechanics, 1985, Cambridge University Press, Cambridge, 1974.

[33] V. Brizmer, Y. Kligerman, I. Etsion, A Model for Junction Growth of a Spherical Contact Under Full Stick Condition, J. Tribol. 129 (2007) 783–790.

[34] D.B. Patil, M. Eriten, Frictional Energy Dissipation in Spherical Contacts Under Presliding: Effect of Elastic Mismatch, Plasticity and Phase Difference in Loading, J. Appl. Mech. 82 (2015).

[35] D.B. Patil, M. Eriten, Effects of Interfacial Strength and Roughness on the Static Friction Coefficient, Tribol. Lett. 56 (2014) 355–374.

Chapter 5 Conclusions

5.1. Conclusions and future work

The main goal of this dissertation was to examine the influence of interface topography on PVE material damping, and to design and fabricate a prototype of PVE passive damper. It was divided into three objectives.

The first objective was to introduce a passive damper design inspired by the cartilage-like PVE mechanisms (*Chapter 2*). The dissipative properties of PVE materials sandwiched by hard materials were studied and the PVE interfaces were modeled using fractional Zener elements. As a conclusion, optimal damping (either narrowband or broadband) can be harvested from those dampers by simply changing the contact parameters.

The second objective was to validate and realize the passive PVE damper idea (*Chapter 3*). Both single and multiple indenter-dampers were designed, tested, and analyzed in a frequency range of 0.5 – 100 Hz. The measured damping capacity of 12 single-indenter-foam dampers were consistent with the scaling analysis and demonstrated an ability to maximize PVE damping at the desired frequency ranges by changing the pore diameter (diffusivity) and contract radius (characteristic diffusion length). The poroelastic peak damping frequency can be tuned to specific modal frequencies of a structure so that damping is maximized only around those modes (narrowband performance). In addition, the optimized two-indenter-foam damper demonstrated that nearly rate-independent damping capacity can be achieved (broadband performance). These findings on PVE dampers can appease the needs of both narrowband and broadband applications in a passive way.

The third objective was to extend the behavior of the PVE indenter-foam dampers to higher excitation levels and analyze their nonlinear responses. The nonlinear dynamic responses were measured and explained in detail (*Chapter 4*). First, we noticed higher harmonics in force measurements on an indenter-foam damper that was harmonically excited under small strains, which was the signature of a nonlinear response. Then, we analyzed relative magnitudes of second harmonics at various strains and strain rates to obtain nonlinearity maps. Since geometric and constitutive nonlinearities were unlikely thanks to small strains used in the experiments, we focused on interfacial nonlinearities, specifically adhesion and peeling dynamics, to explain the source of those nonlinearities. In summary, any of the reduction in contact stiffness, the decrease in contact lengths and degree of peeling could predict the degree of nonlinearity in dynamic response of the indenter-foam dampers. Our findings suggest increasing adhesion at the indenter-foam interface would suppress those nonlinearities trivially (e.g., via chemical and physical reinforcement of interfaces).

This dissertation not only makes several contributions to knowledge about the PVE interfacial damping mechanisms, but also provides an effective passive damper design. The performance and limitations of those dampers have been discussed thoroughly. The next step would be to integrate those dampers into semi-active and active damper designs to guarantee and adaptive damping performance. MR fluids, for instance, can be a good choice for semi-active damper design when used as a swelling agent in the indenter-foam dampers. Similarly, MR elastomers can provide active alternative to the foams. MR fluids and elastomers have attracted a significant amount of attention for their potential in engineering applications during the last few decades; as evident from numerous applications as vibration absorbers, base isolators and sensing devices [1–4]. A natural extension of my doctoral studies can take advantage of those materials'

ability to absorb energy and its controllability with external magnetic fields. For example, Maranville and Ginder tested the dynamic mechanical properties of MR fluids entrained in open-cell polyurethane foams [5]; Hirunyapruk et al. presented a MR fluid-filled structure device as a tunable vibration absorber [6]; Dohmen et al. introduced a polyurethane-based MR fluid composite, and reported its behavior under external magnetic fields [7]. All the studies indicated that increasing the applied magnetic field increases both the complex shear modulus and energy dissipation of the devices. Therefore, we might adjust the magnitude of the energy dissipated by the MR fluid foams via applied magnetic field strength and thus achieve real-time control on indenter-foam dampers.

5.2. References

[1] Y. Li, J. Li, W. Li, H. Du, A state-of-the-art review on magnetorheological elastomer devices, Smart Mater. Struct. 23 (2014) 123001.

[2] Zielinski, Tomasz G., and Michal Rak. Acoustic absorption of foams coated with MR fluid under the influence of magnetic field, J. Inte. Mater. Sys. Struct. 21, no. 2 (2010): 125-131.

[3] M. Behrooz, X. Wang, F. Gordaninejad, Modeling of a new semi-active/passive magnetorheological elastomer isolator, Smart Mater. Struct. 23 (2014) 045013.

[4] M.J. Chrzan, J.D. Carlson, MR fluid sponge devices and their use in vibration control of washing machines, in: Smart Struct. Mater. 2001 Damping Isol., SPIE, 2001: pp. 370–378.

[5] C.W. Maranville, J.M. Ginder, Small-strain dynamic mechanical behavior of magnetorheological fluids entrained in foams, Int. J. Appl. Electromagn. Mech. 22 (2005) 25–38.

[6] C. Hirunyapruk, M.J. Brennan, B.R. Mace, W.H. Li, A tunable magneto-rheological fluid-filled beam-like vibration absorber, Smart Mater. Struct. 19 (2010) 055020.

[7] Dohmen, Eike, Martin Boisly, Dmitry Borin, Markus Kästner, Volker Ulbricht, Maik Gude, Werner Hufenbach, Gert Heinrich, and Stefan Odenbach, Advancing Towards Polyurethane-Based Magnetorheological Composites, Adv. Engin. Mater. 16, no. 10 (2014): 1270-1275